

An Investigation on Small Scale Precipitation Structures

Von der Fakultät für Mathematik und Physik
der Gottfried Wilhelm Leibniz Universität Hannover
zur Erlangung des Grades
Doktor der Naturwissenschaften
Dr. rer. nat.
genehmigte Dissertation
von
Dipl.-Met. Michael Theusner
geboren am 08.12.1974 in Hannover

2007

Referent: Prof. Dr. T. Hauf
Korreferent: Prof. Dr. D. Etling
Tag der Promotion: 02.02.2007

Abstract

The subject of this study is to better understand the geometrical structure of fields of post-frontal deep convective cells. Rain fields from 39 summer days are investigated using the national radar composite of the DWD. Using the data of a radar network allows to analyse 2-D structures about one order of magnitude larger than done in previous studies.

It is shown here, for the first time, that the peak number distribution (PND; the peak number represents the number of convection cells within a cluster of cells) is not only self similar (it is a power law) over the average of several days, but also down to temporal scales of one hour. Furthermore, it is found that the PND does not vary over a large area despite large differences in orography and surface inhomogeneities. Additionally, evidence is presented that the German North Sea coast markedly enhances convective activity, very likely due to roughness length changes and sea breeze effects. The total number of rain areas and their total size follow typical diurnal cycles mainly influenced by surface heating, but likely also other effects. The maximum of convective activity is reached in the early afternoon. In contrast to the well defined diurnal cycles of the aforementioned parameters, the average number of deep convection cells per cluster does not change much during the day. This new finding is shown to be a consequence of the self similar frequency distribution which does not change over a certain day either.

The rain area size distribution is log-normal for each peak number, confirming results of earlier studies. The parameters that govern the log-normal distributions depend on the peak number and can be represented by power laws. It is found that μ_p is a combination of two power laws in contrast to previous research. This new finding is a consequence of the larger spatial scales investigated here.

For the first time, the distances between the centers of deep convection cells using radar are investigated. It is found that their frequency distribution is log-normal and almost identical for each peak number. The frequency distribution independent of the peak number is also log-normal as was found for cloud fields observed by satellites.

The fractal dimension of the rain areas is low for small rain areas ($d = 1.19$) and increases to $d = 1.67$ for large rain areas. This change can be traced back to unicellular and multicellular rain areas. The break diameter D_b is about 20 km.

The methods developed during this work and the results presented here supported the initiation and extension of a project within the framework of the DFG's priority program Quantitative Precipitation Forecast (SPP 1167 PQP). They were also successfully used to validate the small scale precipitation structures of the regional climate model BALTIMOS. Additionally, the obtained statistics lay the basis for the development of a rain cell generator.

Keywords: radar, precipitation structures, convection
Schlagworte: Radar, Niederschlagsstrukturen, Konvektion

Zusammenfassung

Ziel dieser Arbeit ist ein besseres Verständnis der geometrischen Struktur von Feldern postfrontaler, hochreichender Konvektionszellen. Dazu wurden unter Benutzung von Radarkompositbildern des DWD Niederschlagsfelder von 39 Sommertagen untersucht. Die Verwendung von Radarbildern eines Radarnetzwerks erlaubt die Analyse zweidimensionaler Strukturen, die etwa eine Größenordnung größer sind als die, die in bisherigen Studien untersucht wurden.

Es wird hier zum ersten Mal gezeigt, dass die Peak-Zahl-Verteilung (PND; die *Peak-Zahl* ist die Anzahl von Konvektionszellen innerhalb eines Clusters von Zellen) nicht nur im Mittel über mehrere Tage selbstähnlich ist, sondern sogar auf Zeitskalen bis hinunter zu einer Stunde. Weiterhin wurde entdeckt, dass die PND trotz großer Unterschiede in der Orographie und großer Oberflächeninhomogenität über große räumliche Skalen konstant ist. Zudem wird gezeigt, dass die konvektive Aktivität entlang der Deutschen Nordseeküste deutlich erhöht ist, was möglicherweise auf Rauigkeitslängenunterschiede und Land-Seewind-Effekte zurückzuführen ist. Die Gesamtzahl der Regengebiete und ihre Gesamtfläche folgen einem typischen Tagesgang der hauptsächlich durch die Oberflächenerwärmung aber auch durch andere Prozesse bestimmt wird. Das Maximum der konvektiven Aktivität wird dabei am frühen Nachmittag erreicht. Im Gegensatz zu den Tagesgängen der zuvor genannten Parameter ist die mittlere Zahl von hochreichenden Konvektionszellen innerhalb eines Clusters über den Tag fast konstant. Es wird gezeigt, dass diese neue Erkenntnis die Folge einer sich über den Tag ebenfalls nicht ändernden, selbstähnlichen Häufigkeitsverteilung ist.

Die Regengebietsgrößen-Verteilung ist für jede Peak-Zahl lognormal und bestätigt damit die Ergebnisse früherer Studien. Die Parameter, die die Lognormalverteilung bestimmen, hängen von der Peak-Zahl ab und können durch Potenzgesetze beschrieben werden. Der Mittelwert μ_p der Lognormalverteilung ist dabei eine Kombination von zwei Potenzgesetzen. Diese neue Erkenntnis wurde durch die Untersuchung größerer räumlicher Skalen möglich.

Zum ersten Mal werden hier die Abstände zwischen den Zentren der Konvektionszellen mit Hilfe von Radardaten untersucht. Es ergibt sich, dass ihre Häufigkeitsverteilung lognormal und für jede Peak-Zahl fast identisch ist. Die Häufigkeitsverteilung unabhängig von der Peak-Zahl ist ebenfalls lognormal was auch durch Studien von mit Satelliten beobachteten Wolkenfeldern berichtet wird.

Die fraktale Dimension der Regengebiete ist klein für kleine Regengebiete ($d = 1.19$) und steigt auf $d = 1.67$ für große Regengebiete. Dieser Unterschied kann auf einzellige und mehrzellige Regengebiete zurückgeführt werden. Der Skalenbruch liegt dabei bei einem Equivalentdurchmesser D_b von etwa 20 km.

Die Methoden, die für diese Untersuchung entwickelt wurden und die erzielten Ergebnisse, unterstützten die Initiierung und die Verlängerung eines DFG-Projektes im Rahmen des Schwerpunktprogramms *Quantitative Niederschlagsvorhersage* (SPP 1167). Sie wurden ebenfalls erfolgreich für die Validierung von kleinskaligen Niederschlagsstrukturen des regionalen Klimamodells BALTIMOS eingesetzt. Außerdem bereiten die beobachteten Statistiken die Basis für die Entwicklung eines Regenzellengenerators.

Contents

List of Figures	viii
List of Tables	x
1 Introduction	1
1.1 Precipitating Convection	1
1.2 Structure of Atmospheric Convection	6
1.3 A Typical Example	7
1.4 Review of Previous Studies	12
1.5 Motivation and Current Demand for Research	15
1.6 Aims and Objectives	16
2 Methodology	19
2.1 Data	19
2.1.1 Radar Data	19
2.1.2 Synoptic Data, Satellite Data and Data Selection	19
2.2 Basic Data Processing	21
2.2.1 Removal of Overlaid Map	21
2.2.2 Decoding Reflectivity Values	21
2.2.3 Segmentation	23
2.3 Data Analysis - Basic Parameters	23
2.3.1 Definitions	27

3	Results	33
3.1	Rain Area Number and Peak Number	34
3.1.1	Diurnal Variation of the Numbers of Rain Areas and Reflectivity Peaks	34
3.1.2	Peak Number Distribution	37
3.1.3	Diurnal Variation of the PND	40
3.1.4	Spatial Variation of the PND	43
3.2	Size of the Rain Areas	48
3.2.1	Diurnal Variations of the Total Rain Area and Related Entities	48
3.2.2	Diurnal Variation of the Average Rain Area Size	49
3.2.3	Diurnal Variation of the Average Area Per Peak	50
3.2.4	Rain Area Size Distribution	51
3.2.5	Rain Area Size Distribution Without Peak Number Distinction	57
3.3	Distances Between Peaks	60
3.3.1	Nearest Neighbor Distribution - Peak Number Depen- dence	60
3.3.2	Nearest Neighbor Distribution - Diurnal Variation . . .	64
3.4	Fractal Dimension	66
4	Conclusions, Limitations and Outlook	68
4.1	Conclusions	68
4.2	Limitations	72
4.3	Summary and Outlook	73
A	Used radar images	74
B	Fast Fourier Transform Parameters	76
C	PND Parameters	78
D	Rain Area Distribution	80

Bibliography	84
Acronyms and Symbols	91
Acknowledgements	94
Curriculum Vitae	95

List of Figures

1.1	Stages of a developing Cb.	2
1.2	Reflectivities in a mature Cb.	4
1.3	Open and closed cell convection, and roll convection	7
1.4	Typical synoptic situation.	9
1.5	Typical post-frontal situation.	10
1.6	Typical temp.	11
2.1	Radar image from 29 August 1998, 10 UTC.	22
2.2	Template containing the river, border, coastline, radar location and text data.	22
2.3	Corrected radar image from 29 August 1998, 10 UTC.	23
2.4	Segmentation process.	24
2.5	Threshold application.	26
2.6	Labeling process.	27
2.7	Determining the perimeter.	28
2.8	Continuous and discrete reflectivity values.	29
2.9	Delaunay triangulation.	31
3.1	Average diurnal variation of the number of rain areas.	34
3.2	Average diurnal variation of the number of peaks.	35
3.3	Average diurnal variation of the number of peaks per rain area.	36
3.4	Peak number distribution.	39
3.5	PND for single days and hourly periods.	41

3.6	Frequency distribution of exponents.	42
3.7	Diurnal variation of the PND.	43
3.8	Diurnal variation of the PND on 21 May 1997.	44
3.9	Spatial distribution of rain areas with $p = 1$ ($\tau = 19$ dBZ). . .	45
3.10	Spatial distribution of rain areas with $32 \leq p < 64$ ($\tau = 19$ dBZ). 46	
3.11	Domains used for the calculation of regional PNDs.	47
3.12	PNDs calculated for four regional domains.	47
3.13	Diurnal variation of the total rain area A_{total}	48
3.14	Diurnal variation of the average area of a rain area A_r	50
3.15	Diurnal variation of the area per peak A_{max}	51
3.16	Size distribution of equicircle diameters for various values of p . 52	
3.17	Parameter μ_p as a function of p	54
3.18	Parameter σ_p as a function of p	55
3.19	Mean diameter \bar{D}_p of the rain areas as a function of p	56
3.20	Mean area associated with each peak as a function of p	57
3.21	Rain area size distribution for $\tau = 19$ dBZ.	59
3.22	Distribution of the frequency of RA populations for $\tau = 19$ dBZ. 59	
3.23	Rain are with $p = 30$ subdivided into smaller subsystems of peaks.	61
3.24	NND for four different peak numbers ($\tau = 19$ dBZ).	62
3.25	Parameter μ_p for the NND as a function of p ($\tau = 19$ dBZ). . .	63
3.26	Parameter σ_p for the NND as a function of p ($\tau = 19$ dBZ). . .	63
3.27	Diurnal variation of the NND independent of p ($\tau = 19$ dBZ)..	64
3.28	Parameter μ_p for the NND as a function of time ($\tau = 19$ dBZ). 65	
3.29	Parameter μ_p for the NND as a function of time ($\tau = 19$ dBZ). 65	
3.30	Fractal dimension of the rain areas.	66
D.1	Parameter σ_p as a function of p (diameter distribution).	81
D.2	Parameter μ_p as a function of p (diameter distribution).	81
D.3	Parameter σ_p as a function of p for the area distribution.	82
D.4	Parameter μ_p as a function of p for the area distribution.	82
D.5	Rain area size distribution for $\tau = 7$ dBZ and $\tau = 28$ dBZ.	83
D.6	Rain area diameter distribution for $\tau = 7$ dBZ, $\tau = 19$ dBZ and $\tau = 28$ dBZ.	83

List of Tables

2.1	Days selected for the analyses.	20
2.2	Relative number of reflectivity values	25
3.1	Coefficients of Equation 3.1.	38
3.2	Coefficients of Equation 3.1 for the PNDs.	46
3.3	Coefficients of Equation 3.4.	55
3.4	Coefficients of Equation 3.5.	55
3.5	Coefficients of Equation 3.12 and 3.13.	62
A.1	List of the used radar images.	74
A.2	List of the used radar images, 1998.	75
B.1	Coefficients for the diurnal cycle of the number of rain areas. . .	76
B.2	Coefficients for the diurnal cycle of the number of peaks. . . .	76
B.3	Coefficients for the diurnal cycle of the number of peaks per rain area.	77
B.4	Coefficients for the diurnal cycle of the total area of rain areas.	77
B.5	Coefficients for the diurnal cycle of the average area of a rain area.	77
B.6	Coefficients for the diurnal cycle of the average area per peak.	77
C.1	PND parameters for single days (1997).	78
C.2	PND parameters for single days (1998).	79
D.1	Coefficients of Equation 3.4 (σ_p) for the area distributions. . .	80
D.2	Coefficients of Equation 3.5 (μ_p) for the area distributions. . .	80

Chapter 1

Introduction

The subject of this thesis is the investigation of post-frontal precipitation pattern also known as post-frontal showers. These showers belong to the phenomenon of deep moist convection and are, hence, precipitating convection. To illustrate the basic principles of such processes a brief overview on the initiation, evolution and characteristics of convective clouds and precipitating convection is given in this first part of the introduction. In the second and third part, the structure of convection and a typical weather situation with post-frontal showers is presented, followed by a review of the literature relevant to this work. Based on that, demand for research is identified in the fourth part. The introduction is closed by outlining the objectives of this thesis.

1.1 Precipitating Convection

Precipitating/deep moist convection is a type of atmospheric convection. Its main difference from dry convection is that the temperature of rising air parcels are cooled below the parcels' dew point temperature. Thus, excess moisture condenses and forms little water droplets or ice crystals. The total vertical heat flux by convection is comprised of the sensible heat flux by dry convection and the latent heat flux by moist convection. On a global scale, the latter is five times larger than the former.

Generally, three main conditions have to be fulfilled for the development of deep moist convection (BARTHLOTT *et al.* 2006):

- a sufficient amount of humidity in the lower troposphere, so that the convective condensation level can be reached and clouds can develop,
- an appropriate vertical density stratification of the troposphere and

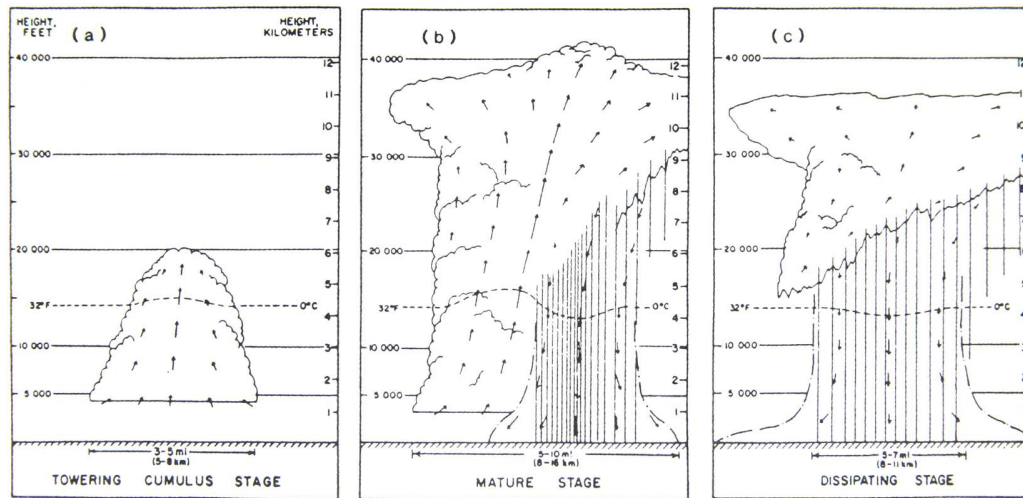


Figure 1.1: Three stages of development of a Cb (from EMANUEL 1994).

- a small-scale triggering process at the ground (described further below).

If these conditions are met, air can rise until its temperature reaches equilibrium with the surrounding air or reaches a capping inversion that is strong enough to prevent further upward motion (either within the Troposphere or at the Tropopause, with the exception of the overshooting tops of cumulonimbus clouds). The vertical motion that develops becomes visible through the formation of little water droplets and ice crystals. Clouds generated by such condensation belong to the cloud family of "clouds with a large vertical extent" (cumulonimbus calvus - Cb cal; cumulonimbus capillatus - Cb cap) and low level clouds (cumulus congestus, Cu con). All these clouds have in common that they are able to form precipitation which can be detected by means of radar. According to EMANUEL (1994), three development stages can be distinguished (Figure 1.1):

- The cumulus stage (Figure 1.1 a),
- the mature stage and (Figure 1.1 b)
- the dissipating stage (Figure 1.1 c).

During the first stage, the cloud behaves very much like a non-precipitating cloud, though, the central updraft is already much stronger compared to a non-precipitating cloud. First radar echoes can be detected that signal the presence of precipitation particles. In course of the further development the number of precipitation particles increases throughout the cumulus stage. The clouds in the first stage typically extend to 1 to 6 km above the freezing

level (AGEE 1982). The stage ends when first rain drops reach the surface, usually about 10 to 15 minutes after the convection cell was triggered.

The mature stage is marked by the presence of a strong updraft. The number of precipitation particles (solid and liquid) still increases as well as their size. Due to their weight, precipitation particles fall and lead to the development of a downdraft within the cloud. The cloud is now in its most active phase which lasts approximately 15 to 30 minutes. Due to the large number and large size of the precipitation particles, the cloud is very prominent in radar images during this stage. A typical example of reflectivities within such a mature cumulonimbus capillatus is given in Figure 1.2. At the end of the mature stage, the updraft that developed at the beginning and sustained the cloud ceases to exist. This is caused by intensified downdrafts which finally cover the whole lower region of the cloud and prevent further influx of warm, moist air.

This trend continues during the dissipation stage until the last water droplets have reached the ground and all downward vertical motion has stopped (AGEE 1982). The duration of the dissipation stage is of the order of 30 minutes. Radar echoes become progressively weaker in the process.

For a detailed, in-depth description of atmospheric convection and the development of deep moist convection refer to e.g. AGEE (1982) and EMANUEL (1994).

Triggering Processes

In the Earth's atmosphere many different processes can lead to the triggering of deep moist convection. In the case of post-frontal convection over Western and Central Europe these processes can be grouped into three major categories. These are (1) local perturbations in the boundary layer, (2) local modification of the atmosphere by previous convection cells and (3) large scale lifting (BENNETT *et al.* 2006). While (1) and (3) include processes that are also important for the onset of precipitating convection, (2) is only relevant when deep convection is already present.

Among the processes found in category (1) are spontaneous generation of mesoscale variability due to upward transport in the boundary layer and horizontal convergence and locally enhanced uplift. They are directly related to

- orography,
- land/sea contrast,
- land-use heterogeneity
- variability in temperature/moisture due to variation in surface characteristics and soil moisture.

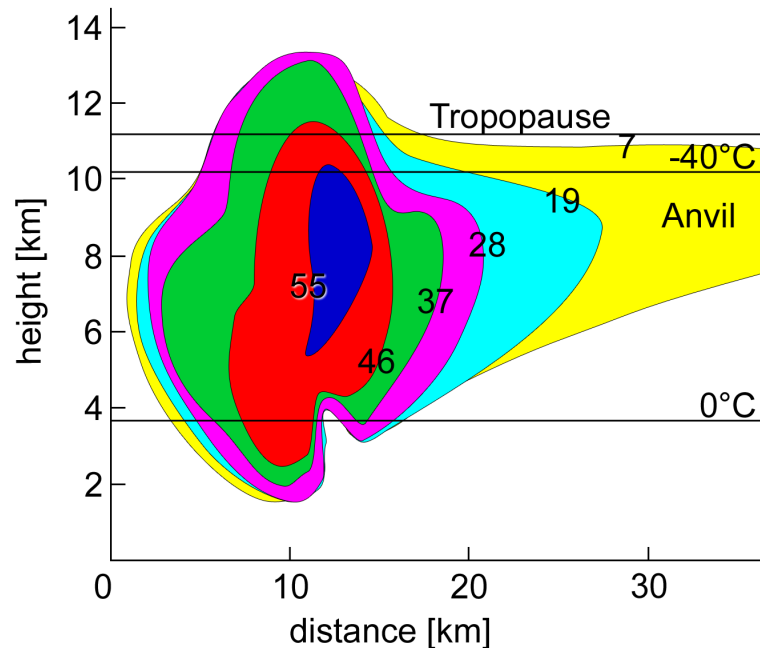


Figure 1.2: Vertical cross section of radar reflectivities detected in a typical mature cumulonimbus capillatus (after AGEЕ 1982, modified).

In the case of well developed deep convection (2) gust fronts formed by the outflow of cold air from the convection cells can initiate further convection cells in their vicinity if their effect dominates over the perturbations caused by the processes listed in category (1) (BENNETT *et al.* 2006).

Coastal and Orographic Effects

The difference between land and sea has two important effects on atmospheric flow. The first is thermal and the second mechanical. The thermal effect results from the different heat capacities of the land surface and the water of the sea. The land heats up more quickly during the day and under suitable conditions enables the development of the well known sea-breeze circulation. The stronger heating of the land surface leads to increased column thickness and the formation of a local low pressure area over land. In absence of strong synoptic scale motions, the resulting onshore flow of moist cold air from the sea leads to the formation of a distinct convergence zone. This convergence causes upward motion and can, hence, trigger the development of (deep) convection. It was also shown by FOVELL and DAILEY (2001) that the interaction between the sea-breeze front and other boundary layer features like horizontal convection rolls are of great importance for the enhancement of convection. That also applies to the collision of different sea-breeze fronts originating from differently aligned parts of a coast (VAN DE BERG and OERLEMANS 1985; WAKIMOTO and ATKINS 1994; ATKINS *et al.* 1995; KINGSMILL 1995; WILSON and MEGENHARDT 1997; BENNETT *et al.* 2006).

The mechanical effect on the atmospheric flow of the coast stems from the change in roughness length between sea and land. This roughness length change induces vertical velocities in the absence of thermal forcing and, thus, enhanced convection (ALESTALO and SAVIJÄRVI 1985; ROELOFFZEN *et al.* 1986; ANDERSSON and GUSTAFFSON 1994). The effect is the greatest when the onshore flow forms an angle with the coastline of about 20° (ROELOFFZEN *et al.* 1986). This is often the case at the German North Sea coast under a westerly to northwesterly flow. It was also observed that precipitation is increased by up to 40% compared to locations further inland (ALESTALO and SAVIJÄRVI 1985).

Orography can also lead to the occurrence of upstream or downstream convergence lines through roughness length differences and forced lifting with the subsequent development of deep precipitating convection (SMOLARKIEWICZ *et al.* 1988; CROOK *et al.* 1990; CROOK *et al.* 1991; WILSON *et al.* 1992; GRAY and SEED 2000; HSU and LEE 2005; DAVOLIO *et al.* 2006).

Another mechanism that involves orography is the latter's influence on convective rolls in the boundary layer. These convective rolls can also get strengthened downwind of hills so that deep moist convection is triggered (TIAN and PARKER 2002; TIAN *et al.* 2003; PIKE 2003)

Temperature and Moisture Variation

The development of moist convection also depends on the stratification of the air mass and its moisture content. Therefore, the temperature of the underlying surface and the moisture content of the soil are of great importance, too. This was shown e.g. by WECKWERTH (2000) who found that small-scale variations in moisture were responsible that deep convection developed on some days but not on others. The variations can be as small as 1 K in temperature and 1 g kg^{-1} in moisture (CROOK 1996) and are typical in a convective boundary layer (WECKWERTH *et al.* 1996). They are closely linked to the type of the underlying surface. Different soil types have different maximum soil moisture contents and differing thermal properties. These structures are superimposed by the spatial distribution of previous rain events and vegetation. Land-use heterogeneity is another important factor that has a strong impact on soil moisture and also temperature (BENNETT *et al.* 2006). The importance of these moisture and temperature variations for the initiation of deep convection was also shown by STIRLING and PETCH (2004). They also report that onset of deep convection can change by several hours and total rainfall amounts by up to 70%.

Previous Convection Cells

When a cumulonimbus cloud has developed to its mature stage, it can spawn the occurrence of second-generation convection. The outflow of cold air from the Cb forms a density current on the ground (a so-called cold pool) that spreads outward from the Cb. It has a distinct gust front that acts as a convergence line and leads to forced lifting of warm air at its leading edge (BENNETT *et al.* 2006). This process can trigger the rapid development of

convection which can also develop into a Cb leading to the generation of a multi-cell storm. Such multi-cell storms have a much longer life-time than a single Cb and often last for hours, while the life-time of each convection cell of such a storm remains unchanged (SMITH 1990; EMANUEL 1994).

All the processes described above and their complex interaction determine where deep precipitating convection cells emerge. They are, hence, of great importance for the spatial distribution of convection cells and for the overall precipitation pattern that forms.

1.2 Structure of Atmospheric Convection

One of the central features of nature and the atmosphere is the development of ordered structures. In the atmosphere, these structures are usually closely linked to convection. The question of the structure of post-frontal showers is subject of this thesis. In this section a brief overview is given on the typical (regular) structures of other types of atmospheric convection which are also in the focus of current research. These are open and closed cell convection (see Figure 1.3a) on the one hand and roll-convection (see Figure 1.3b) on the other. These systems develop within the convective boundary layer (ATKINSON and ZHANG 1996).

Open and closed cells are usually found over the oceans (EMANUEL 1994) where a suitable density stratification exists in the boundary layer due to differences in air-sea temperature (ATKINSON and ZHANG 1996). The vertical extent of these convective elements is typically about 1-3 km vertically and 10-40 km horizontally, which can also clearly be seen in Figure 1.3a. These structures are very similar to Rayleigh-Bénard convection observed in laboratory experiments. The major difference between both of them is their very different aspect ratio. It is 5-50 in the atmospheric case and close to unity for Rayleigh-Bénard convection. To explain these differences and even the occurrence of convection of this type is subject of ongoing research.

Roll convection often occurs in polar cold air outbreaks. The large difference in temperature between air and sea leads to the development of a convective boundary layer. If the horizontal wind velocity is high enough, two-dimensional convection aligned with the shear vector can develop and forms so called cloud streets (EMANUEL 1994; see Figure 1.3b). The separation of these rolls is usually around 2-20 km and they have a vertical thickness of 2-3 km. Their aspect ratio therefore varies between unity and about eight (SCHRÖTER 2003). Development and occurrence of these rolls also is a matter of current research activities as these systems are still not well understood.

When the organized convective systems described above are advected onto land, their structure usually changes drastically. Due to the phenomena

described in Section 1.1, convection is often enhanced and shallow convection develops into deep convective systems. The structure that occurs in that process is described in the following section.

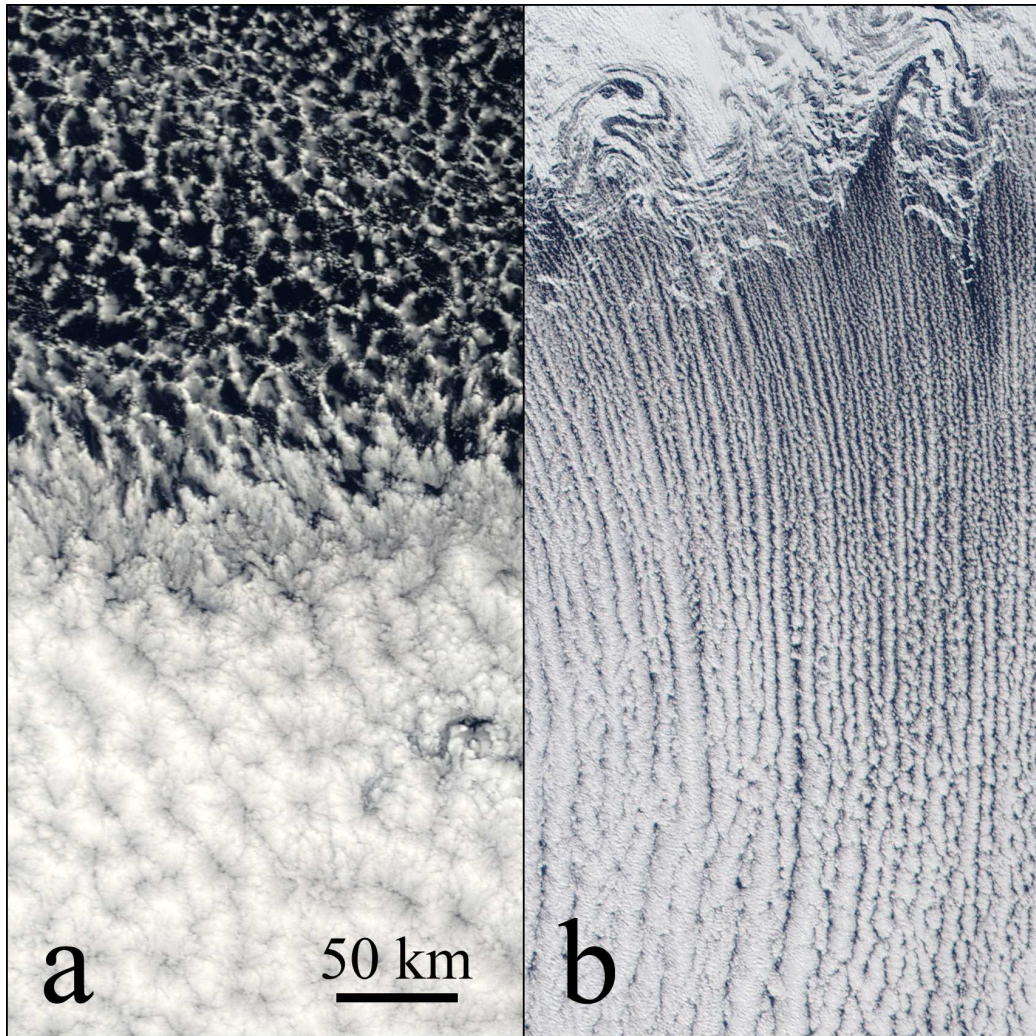


Figure 1.3: (a) Open (upper half) and closed cell convection (lower half) over the Pacific Ocean. (b) Roll convection over the Davis Strait (MODIS images). A gradual transition of the rolls to closed cells is observed with increasing distance from the ice edge (white swirls at the top of the image).

1.3 A Typical Example

The convective structures that are subject of this investigation develop in cold air masses of polar origin. Situations suitable for the analysis can therefore be

described as follows: A cold front passes over Germany/Western Europe and post frontal convective structures appear in the rear of the front (cf. Figure 1.5), especially, when a trough is located over the North Sea or the Atlantic Ocean or the British Isles. Such a trough leads to enhanced lift upstream of its location through positive vorticity advection. The fronts in these cases approach Germany from northwesterly to southwesterly directions.

A typical example of such a post-frontal convective situation over Western Europe on 28 May 2006 at 11-12 UTC is given in Figures 1.4 and 1.5. On the back side of a frontal system connected to a low over the central Baltic Sea, cold air of polar origin moves onto the continent with a northwesterly flow. A large area of lifting is associated with the low and the low's trough. The radiosonde sounding at WMO station 10393 Lindenberg of 12 UTC shows that the airmass within the lifting area is characterized by an unstable stratification (Figure 1.6). Air parcels released at the ground can reach an altitude of approximately 6.5 km. Large convective clouds of that height are indeed present in this area and can be seen in a satellite image (Figure 1.5). The Cbs are visible as large bright white spots. Some of the Cbs have already developed an anvil (upper right area of the satellite image). Strong precipitation is connected to the Cbs, visible in the radar reflectivity map (Figure 1.5).

The influence of the coast on convective activity (as described in the previous section) is clearly evident in the satellite images. Upstream, over the ocean, no convective clouds are found. This changes abruptly as soon as the air mass flows onto the continent, because convection is triggered by the effects described in section 1.1 and convective clouds evolve. Some of them are aligned in cloud streets, a structure that can still be identified far inland, especially over the Northern German low lands. In other parts, especially further south, the linear structures of the cloud streets change into a more irregular and random spatial distribution, possibly caused by orography and other effects as explained above. The basic structures of convective precipitation which are investigated in this thesis are evident in Figure 1.5. While some of the convection cells remain as single cells, others are members of large clusters of cells (the alignment of these structures will not be investigated). To gain a deeper understanding of these structures and to find suitable parameters to describe mathematically the spatial distribution of the convection cells is purpose of this thesis.

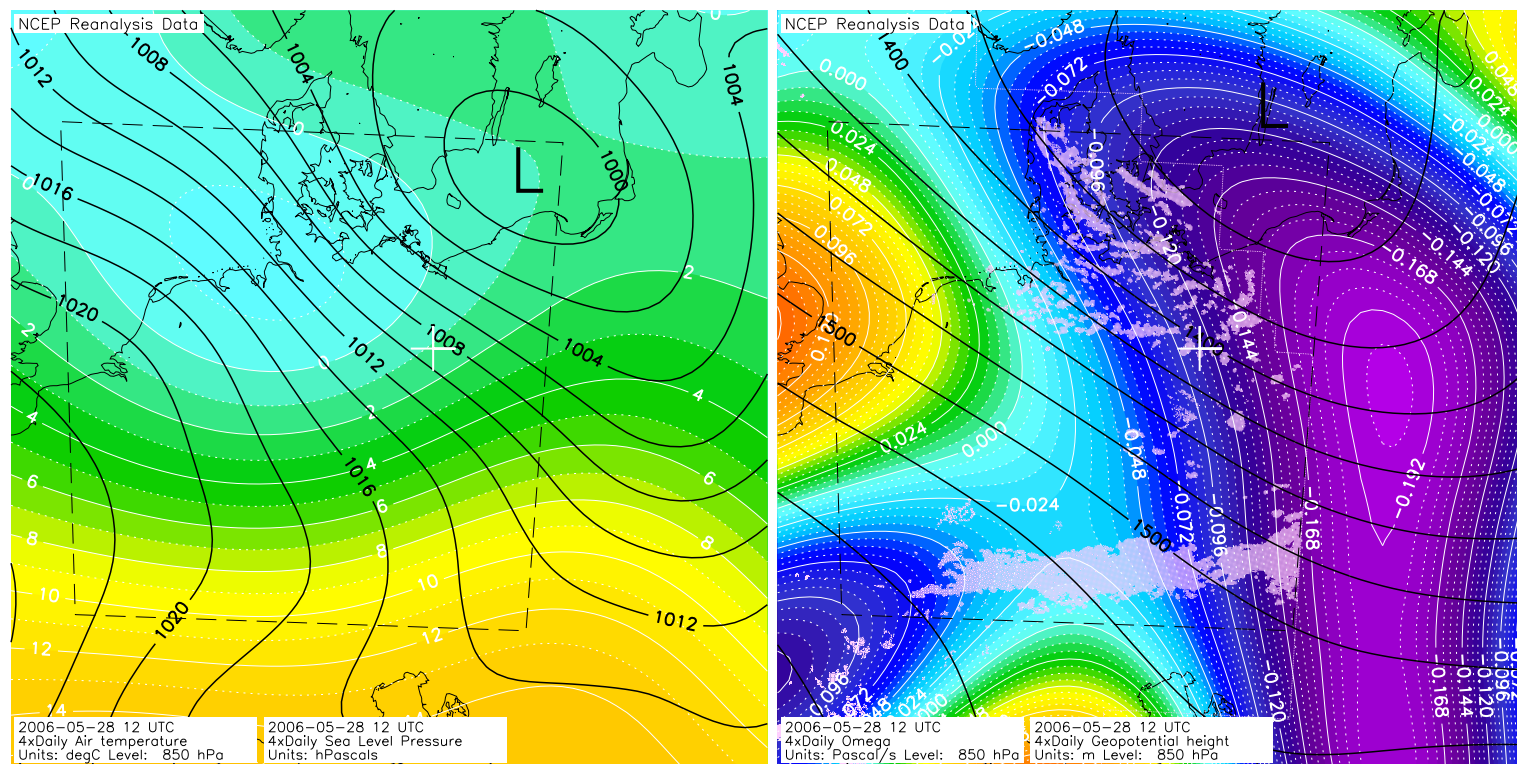


Figure 1.4: Synoptic situation over Western Europe on 28 May 2006 at 12 UTC (NCEP reanalysis data). The reanalysis data show the situation one hour after the high resolution satellite images were taken (see Figure 1.5). The long dashed lines represent the area covered by these satellite images. The temp displayed in Figure 1.6 was recorded at the location of the white cross. In the left image the 850 hPa temperature and the sea level pressure are shown. Omega and geopotential height (both at 850 hPa) are displayed in the right image. Additionally, the location of precipitation evident from the radar reflectivity values is indicated by the light pink area (pink line: border of the radar composite image), it is clearly associated with the large scale lifting (negative omega) within the low pressure system and its trough (right edge of the image).

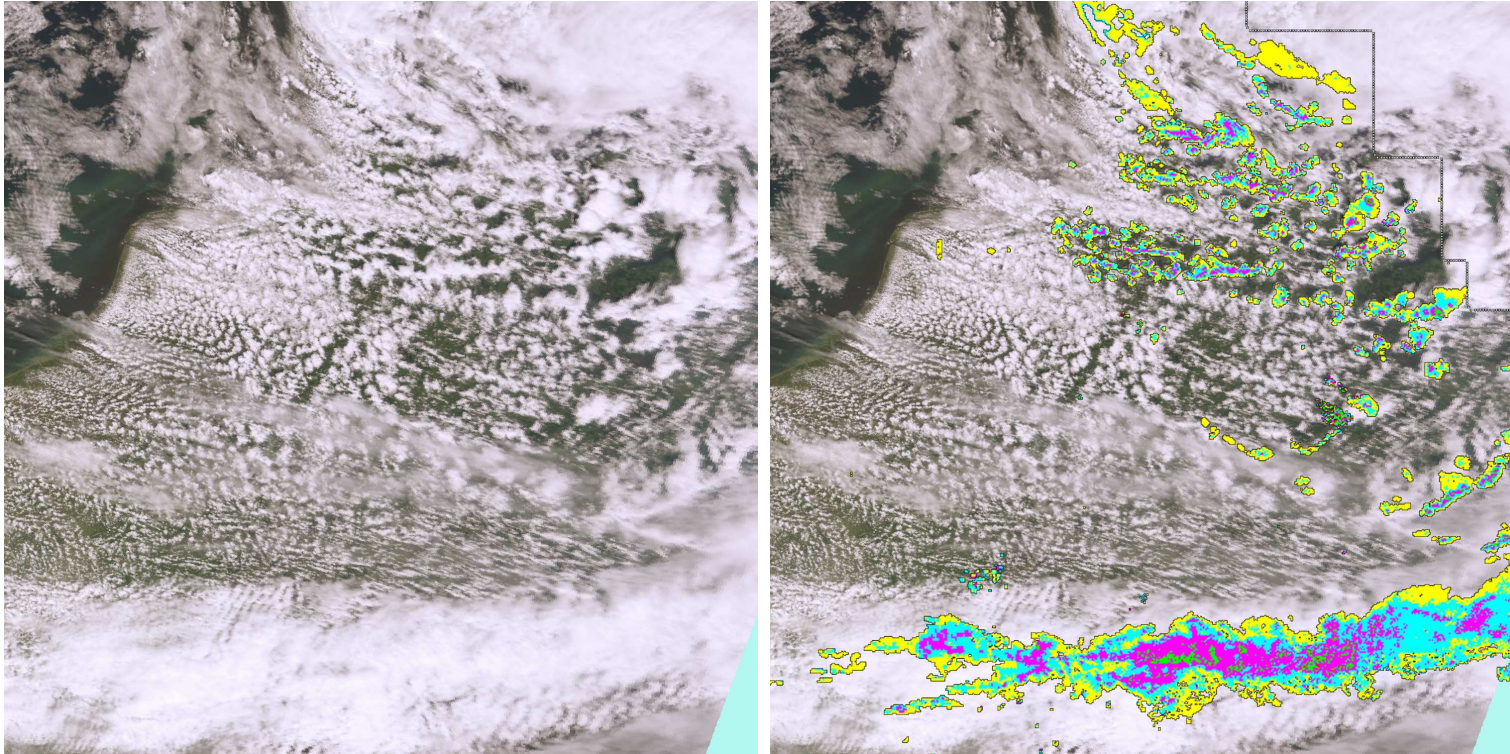


Figure 1.5: Left: MODIS image recorded over Western Europe on 28 May 2006 at 11 UTC (one hour before the synoptical situation displayed in Figure 1.4). Many typical convective structures can be identified like cloud streets (left half of the image) and deep moist convection (Cbs, upper right quarter). The cloud band of the cold front is located at the bottom of the image, over the Alps. Right: the same image with an overlay of the radar reflectivity values recorded at that time. Precipitating convection, evident by the cluster-shaped structures, is mainly found in the upper right quarter where the Cbs are observed.

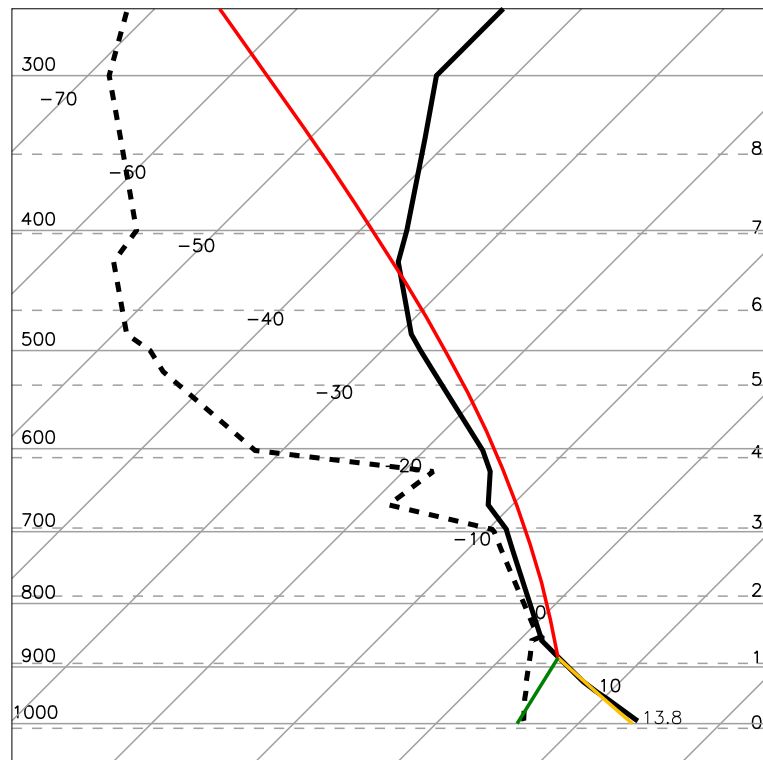


Figure 1.6: Sounding of synoptic station 10393 Lindenberg on 28 May 2006 at 12 UTC (1 hour after the satellite images of Figure 1.5) plotted as a Skew-T diagram showing temperature (solid black line) and dew point (dashed line, both given in degrees Celsius). The atmosphere is characterized by a typical unstable stratification which allows free convection to reach an altitude of approximately 6.5 km (intersection between moist adiabat, red line and temperature). The yellow line represents the dry adiabat and the green one a constant saturation mixing ratio.

1.4 Review of Previous Studies

Convection is one of the dominating processes of the lower atmosphere. It is, therefore, not surprising that a large number of investigations of the structure of convection (see Section 1.2) have been undertaken during the last few decades. These are usually carried out using satellite images (photographic and radiometric data) which use visual and near infrared channels and are able to record the whole spectrum of droplet/ice particle sizes. They allow the analysis of convective structures over large areas and scales, i.e. to determine their characteristic size distributions and fractal dimensions. That also applies to radar images, though, these cover areas more limited compared to satellite images and reflect precipitating clouds, only, as they are usually limited to droplets/ice particles larger than $100 \mu\text{m}$. In the following, first, an overview is given on the results from structure analyses of clouds before results from radar image analyses are presented.

Satellite based studies

Cumulus cloud size distributions, in the range of approximately 100 m to 15 km, were investigated by, eg., WIELICKI and WELCH (1986), WELCH and WIELICKI (1986), WELCH *et al.* (1988), CAHALAN and JOSEPH (1989), JOSEPH and CAHALAN (1990), SENGUPTA *et al.* (1990), WEGER *et al.* (1992), ZHU *et al.* (1992), KUO *et al.* (1993), BENNER and CURRY (1998) and GOTOH and FUJII (1998). Usually, the size parameter considered for the analysis is the equivalent circular diameter D of the cloud area. Most authors report that the size distribution of the clouds can very well be reproduced by two simple power laws ($N(D) = N_0 D^{-\alpha}$). A value of α around -1.7 has been found for clouds with a diameter smaller than a certain break diameter D_b . For larger clouds ($D > D_b$) α is typically close to -3.4 . Mostly, the slope changes drastically for $D_b \approx 1 \text{ km}$.

Evidence has been found that the marked slope difference is associated with a change from a unicellular population to a multicellular population of clouds. Whether a cloud is unicellular or multicellular depends on the number of convection cells found in each cloud (THEUSNER and HAUF 2004). The counting of the number of cells is performed by considering the bumps on the cloud tops in satellite images. The break diameter D_b is found to distinguish between the two different populations, as the corresponding diameter of the clouds grows when the multicellular character of the clouds evolves (the area of a multicellular cluster is usually much larger than a unicellular cloud). The type of frequency distribution and dependencies influence of unicellular and multicellular populations is dealt with in this investigation as well.

Size distributions for large deep convective cloud clusters (size range between 20 km and 500 km equivalent circular diameter) have also been investigated by a number of scientists (MACHADO *et al.* 1992; MACHADO and ROSSOW 1993; MAPES and HOUZE 1993; CARVALHO and SILVA DIAS 1998). Again, power laws were found to very well represent the size distributions.

Though, in one case, a log-normal distribution of the cloud sizes is reported (MAPES and HOUZE 1993).

Besides size distributions, nearest neighbor spacings between the clouds were analyzed as well. All authors report that a log-normal function describes the spacings between the clouds best (e.g. ALI 1998; SENGUPTA *et al.* 1990; JOSEPH and CAHALAN 1990) and that it is superior to Weibull distributions.

Another aspect relevant for the analysis of the structure of objects is the so-called fractal dimension. It provides information on the wigglyness of the perimeter U of an object compared to its area A (MANDELBRODT 1982). The perimeter to area relationship $U = cA^{d/2}$ shows the connection between the two parameters, where d is the aforementioned fractal dimension. For simple structures as circles or squares, the fractal dimension $d = 1$. For structures with $A \rightarrow 0$ and $U \rightarrow \infty$, the fractal dimension $d \rightarrow 2$. Many authors (eg. LOVEJOY 1982; RYS and WALDVOGEL 1986; LAWFORD 1996; FERAL and SAUVAGEOT 2002), relying on satellite and radar imagery, found that the fractal dimension of clouds and rain areas is $d = 1.35$. That there is a single value for the fractal dimension for the whole population implies that these objects are *self similar* throughout the whole size range.

Other researchers detected that for small clouds ($D < 1$ km), the fractal dimension of the clouds is significantly smaller than for larger clouds (D of up to 20 km). In the first case, fractal dimensions of $1.08 < d < 1.29$ were found, indicating that small clouds have a rounder perimeter than their larger counterparts which exhibit fractal dimensions of $1.27 < d < 1.73$ (BENNER and CURRY 1998). These differences are attributed to the influence of the unicellular and multicellular structures of the clouds (CAHALAN and JOSEPH 1989; SENGUPTA *et al.* 1990; KUO *et al.* 1993; BENNER and CURRY 1998). This is reinforced by the value of the break diameter observed for the cloud size distributions, which is the same for the fractal dimension. Low fractal dimensions have also been analyzed for supercell storms, likely because they are unicellular (FERAL and SAUVAGEOT 2002). The fractal dimension and a possible break diameter are also subject of the work presented in this thesis.

Radar based studies

Rain fields cannot be observed with satellite imagery, as they are contained within the cloud continuum. In contrast, the convective structures of homogeneous or continuous cloud fields can be observed by radar only. Despite this and although radar is widely used in atmospheric research, the investigation of the structure of convective clouds by means of radar has not received close attention in the past (reviews by CRANE 1996; SAUVAGEOT *et al.* 1999; MESNARD and SAUVAGEOT 2003).

First radar based investigations of convection already took place in the late 1940s, shortly after the invention of radar systems. MATHER (1949) obtained information on the size of precipitation echoes and found a roughly linear relationship between cell diameter and height. DENNIS and FERNALD

(1963) noted an exponential decrease with size of the number of showers in a certain area. Their area of investigation covered a radius of 75 nautical miles (approximately 140 km) at several locations in the USA, England and over the Pacific Ocean. Similar results were found by MILLER *et al.* (1975), who also noted that no seasonal variation of the statistics was evident.

An exponential representation of the rain area size distribution was also reported by DRUFUCA (1977) and KONRAD (1978). GOLDBIRSH and MUSIANI (1986) also acquired that the size distribution of rain cells with an equivalent diameter between 1 km and 5 km can very well be fitted by an exponential function. The value of the slope and other parameters was found to be invariant with respect to the rain rate threshold τ for a large range of rain rates (3 mm/hr to 88 mm/hr). Another set of studies prefers to use a log-normal distribution to describe the height of rain areas and precipitation duration (LOPEZ 1977; HOUZE and CHENG 1977; LOPEZ *et al.* 1984), as well as the rain rate (KEDEM *et al.* 1990; SAUVAGEOT 1994). It is hypothesized that the law of proportional effects (LOPEZ 1977) could explain the frequent observation of log-normal frequency distributions in Earth systems. The types of distributions suitable to describe the rain areas will be discussed below.

In a recent study by MESNARD and SAUVAGEOT (2003) rain area size distributions were investigated with respect to the number of convection cells the rain areas consist of. The number of convection cells was deduced by counting the maxima of radar reflectivity (the so-called peak number) within a contiguous area of reflectivity, respectively rain rate. A procedure which is used in this thesis as well. The study was performed using radar data from four single radars. It was found that the rain area size distribution for each peak number is log-normal, as was found by other studies for other properties of the rain areas (see above). Consequently, the rain area size distribution is the integral of all the log-normal distributions. Furthermore, the authors report, that the frequency distribution of the peak numbers is a power law. The slope of which depends on the cut-off. All these results are followed up here as well and extended to larger scales than those covered by single radars through the use of radar composite images.

Self organizing criticality

Recently, the theory on self-organizing criticality (SOC) systems has successfully been used to explain the evolution of ordered structures in chaotic systems. This theory was published in 1987 in two ground breaking papers by BAK *et al.* (1987) and BAK *et al.* (1988) and has successfully been applied to numerous natural systems. The authors report that certain extended dissipative dynamical systems naturally develop into a critical state, with no characteristic time or length scales. The temporal finger print of these systems is the presence of so-called $1/f$ noise, while the spatial signature is the evolution of scale-invariant, self-similar (fractal) properties (evident as a power law shaped frequency distribution). The presence of such frequency distributions is investigated in this work, too.

1.5 Motivation and Current Demand for Research

During the last ten years, a range of precipitation events, the severity of which surprised authorities as well as scientists, proved that the understanding of processes leading to such events and the ability to forecast them is still limited. Among these events are the flood at the Oder/Odra river in 1997, the Elbe/Labe and Rhone valley in 2002 (KUNDZEWICZ *et al.* 2005), floods in Wales in 2001 (BENNETT *et al.* 2006) and in Boscastle (UK) in 2004 (BURT 2005). In many of these cases convective precipitation was involved and the spatial structure of the precipitation fields played an important role. In the aftermath of the Elbe flood, the Deutsche Forschungsgemeinschaft (German Research Foundation, DFG) recognized the deficits in the understanding of precipitation processes and initiated a large scale research program named Quantitative Precipitation Forecast (SPP 1167 PQP). It is stated by the DFG that "the correct and timely forecast of precipitation is of great public interest and, because of the damaging potential of heavy rain, flooding, hail and gales, has significant societal importance. During recent years considerable progress has been made in the general field of numerical weather forecast, whereas in the sub-area of quantitative precipitation forecast this was not the case to the same extent".

Quantitative analyses of precipitation have shown (e.g. HAUF *et al.* 2001) that the amount of rainfall generally, among other factors, depends on the spatial structure of the precipitation fields. Based on these findings and the statements of the DFG, this thesis aims to analyze the spatial and temporal structure of post frontal convective precipitation (by means of radar images) to provide a basis for further investigations on how the observed structures influence the amount of observed precipitation. It extends work carried out by MESNARD and SAUVAGEOT (2003) and THEUSNER and HAUF (2004). The results presented in this thesis led to the funding and extension of a research project in the framework of the SPP 1167 QPF. That project aims at the development of a hybrid probabilistic forecast model for post-frontal convective precipitation and is currently conducted at the Institute of Meteorology and Climatology of the Leibniz University of Hannover.

Another area where the investigation of precipitation structures proved to be very useful is the validation of atmospheric models. Techniques developed during the work for this thesis were used to compare statistics of observed and modeled precipitation structures (THEUSNER and HAUF 2006), namely those of the BALTRAD radar network (KOISTINEN and MICHELSON 2002) and the regional climate model BALTIMOS (JAKOB and ET. AL. 2006).

According to HOUZE (1993), GEORGAKAKOS and KRAJEWSKI (1996) and CHENG and ARAKAWA (1997) knowledge on the spatial structures of precipitation, in the form of the rain area size distribution, is also relevant

to circulation models used for the parametrization of the water and energy cycle. Support could also be provided for hydrology and rain-runoff models as well as weather models as stated by SAUVAGEOT (1994) and MESNARD and SAUVAGEOT (2003).

The literature review regarding investigations on precipitation structures using radar showed that research in this area is still very limited, despite the wide spread use of radar systems today (MESNARD and SAUVAGEOT 2003). The parameters that are analyzed usually include the rain area size distribution. It was also found that various approaches have been used in the investigation of cloud and rain area size distributions (see section 1.4), with the result that a number of different size distributions are reported to represent the observed data. Also, it is suspected that there are changes of the parameters of the population during the transition of unicellular to multicellular structures, without the ability to conclusively prove that assumption (cf. section 1.4). Furthermore, investigations that consider the number of convection cells within a convective structure are absent, to the authors knowledge, with only one exception (MESNARD and SAUVAGEOT 2003). In the latter case, no distinction between convective and stratiform rain is made, even though these two types of rain originate from markedly different processes.

Furthermore, the temporal variation of the statistics is merely analyzed on seasonal scales (see section 1.4), while a possible diurnal variation of the size distributions is not discussed. Investigations of spatial variability are usually limited to comparisons of land/ocean differences, relying on a single or a set of single radar stations. They do not consider possible spatial variations e.g. over land itself due to orographic forcing. This is very likely resulting from the lack in the past of appropriate radar composite images which combine data from a number of radar stations to cover much larger areas than a single radar station can.

The recent developments in the area of SOC systems explained why certain types of frequency distributions are frequently found in Earth systems. One of the most prominent examples of a SOC system is Rayleigh-Bénard convection (GETLING 1998). Even though, typical Rayleigh-Bénard convection is not found in the Earth's atmosphere, certain convective systems on Earth show very similar structures (see Section 1.2). Thus, the question arises whether or not evidence for a SOC system is found for post-frontal convection, too.

1.6 Aims and Objectives

The previous section shows that the demand for research in the area of radar based analysis of (convective) precipitation structures is high and that only

limited work has been performed so far. Results from studies on precipitation structures could, furthermore, provide input for a number of applications.

The main aims and objectives of this thesis are, therefore:

- To provide a contribution for a better understanding of spatial pattern of post-frontal convective rain fields.
- An application of the same analysis strategies presented in section 1.4 to the composite images of a radar network. This enables to check the validity of previous results for radar observed structures which are almost two orders of magnitude larger than the ones investigated so far. The radar network of the German Weather Service (DWD) provides a sound basis for this undertaking.
- To limit the investigation to one type of precipitation (convective).
- To distinguish the convective precipitation structures in dependence of the number of convection cells contained within them.
- To test which frequency distributions describe the analyzed convective rain areas. Especially, to check whether or not the equations forecasted by the theories of the law of proportional effects and self-organizing criticality can be used to represent well the size distributions (and other analyzed parameters).
- An analysis of spatial and temporal dependencies of the frequency distributions.
- To investigate the fractal dimension of the precipitation structures and find a possible break diameter.
- To analyze the diurnal cycle of the convective structures (number and size).

To serve the demands and to achieve the aims presented above, one main data set will be used. It is an extensive set of radar composite images provided by the German Weather Service, covering the months May to August 1997 and June to August 1998. The period of investigation is therefore limited to the summer months, respectively, to ensure comparable atmospheric conditions. Additionally to the radar data, many other data sets were used including photometric and radiometric satellite images, synoptic observations and analyses. While radar images provide the basic data for the temporal and spatial structure analyses, satellite and synoptic data enable to recognize regions over Germany with the required post-frontal conditions.

The following basic hypotheses and expectations resulting from the literature review suit as guidelines that lead through the investigation of the data set:

- The rain area size distribution (RASD) and its parameters are a function of the peak number p and can be fitted by simple functions.
 - The RASD is log-normal for rain areas containing the same number of peaks p .
 - The frequency distribution of the distances of convection cell centers to their nearest neighbor are also log-normal.
 - The area size distribution can be described by the combination of the RASD for rain areas containing the same number of peaks p .
- The peak number distribution (PND) is expected to be a power law.
 - Power laws are found for all investigated temporal and spatial scales.
 - The PND varies markedly from day to day, but is nearly constant on a certain day.
 - The PND is the same for the whole investigated domain.
- The numbers of rain areas and deep convection cells as well as their total size show a marked diurnal cycle
 - Enhanced surface heating and other factors lead to a diurnal cycle of the numbers of rain areas and deep convection cells with a maximum in the early afternoon.
 - Orography also enhances convective activity.
- The fractal dimension of the rain areas is expected to range from 1.2 to 1.8.
 - A break diameter D_b separates unicellular and multicellular populations, the latter exhibiting a markedly larger fractal dimension than the unicellular rain areas.

The thesis is structured as follows: First, the data set used and the methodology will be described, also detailing the basic parameters that were used in this work. After that, the results are presented and discussed followed by the conclusions. At the end a brief the limitations of this studies are outlined and a summary and outlook are given.

Chapter 2

Methodology

2.1 Data

2.1.1 Radar Data

The German Weather Service's (Deutscher Wetterdienst, DWD) national radar composite product (the so-called PC-product) contains the spatial distribution of the near-surface radar reflectivity as a logarithmic, six-step color scale (dBZ values) with a lower cut-off of 7 dBZ during the summer months (DWD 1998). From 15 local radars, the lowest elevation PPI (plane position indicator) which is not obscured by the surrounding terrain is contributed in this product. Hence, the lowest elevation angles vary between 0.5° and 1.8° . The radar composite covers most of Germany and also parts of neighboring countries. It extends over an area of approximately 920 km x 920 km. The spatial resolution of the product is 2 km x 2 km (in this case a pixel is a square picture element). The radar composites are available every 15 minutes. Data in this study were clutter filtered by the routinely applied filters of the DWD. For a complete description of the data set one may refer to DWD (1998). Radar data used for this investigation were provided by the DWD for the periods from 1 May 1997 to 6 September 1997 and 1 June 1998 to 31 August 1998. This period includes the meteorological summer months of both years.

Problems result from local radar images missing for certain time steps. They interrupt the time series of the spatial radar reflectivity distribution. For some times the whole radar composite image was unavailable.

2.1.2 Synoptic Data, Satellite Data and Data Selection

Several datasets were used to obtain an overview of the synoptic situation over Central Europe and to find suitable convective situations. The typical

cloud patterns can easily be identified in satellite images as visible in Figure 1.5. These cloud patterns are usually visible as cellular and cluster-shaped structures (as described in Section 1). Images of polar orbiting NOAA-satellites obtained from the Dundee Satellite Receiving Station were analyzed to find such patterns (NOAA AVHRR channel 2; near infra-red, 0.725-1.10 μm) by eye. The radar images were then used to detect precipitation inside the convective structures. Additionally, charts of the 500 hPa geopotential height (Berliner Wetterkarte, Europäischer Wetterbericht) were checked to find out whether the area with the convective structures was located on the upstream side of a trough or not. Also, advection of deep, cold air masses at upper levels from Polar Regions can be recognized from these maps. The significant weather observed at the meteorological stations provided additional knowledge on the distribution of convective showers.

A detailed description of the climatic conditions in the months of the investigated period can be found in THEUSNER and HAUF (2004). In summary, it can be said that most of these months represent typical German summer months with average conditions deviating only slightly from the long term mean. Only July 1997 (precipitation of up to 300% of the 1961-1990 average) and August 1997 (temperature +3 to +5 K above 1961-1990 average) are an exception due to some unusual circulation patterns. The situation in August 1997 with high pressure over central Europe led to the absence of post-frontal convective situations between 2 and 28 August 1997.

These criteria led to the choice of 39 days all together, twenty of them are from 1997 and nineteen from 1998. The chosen dates are listed in Table 2.1. For these 39 days a total number of 3717 radar images were available. This corresponds to an overall completeness of 99.3%. Finally, of these 3717 radar images 3258 were used for the investigation as only those contained convective precipitation pattern. A list of the utilised radar images is given in Appendix A.

Table 2.1: Days selected for the analyses.

month	days
May 1997	7, 9, 10, 21, 28, 30, 31
June 1997	9, 14, 22, 23, 24
July 1997	1, 4, 5, 19, 27, 29
August 1997	1, 29
June 1998	10, 11, 15, 16, 17, 18, 28
July 1998	1, 5, 6, 7, 14, 15, 31
August 1998	5, 22, 23, 27, 29

2.2 Basic Data Processing

2.2.1 Removal of Overlaid Map

The radar data described in Chapter 2.1.1 were provided as images in Graphics-Interchange-Format (GIF). Besides the actual radar data other data sets had been overlaid on the images for orientation and information purposes (Figure 2.1):

- Rivers,
- borders,
- coastlines,
- locations of radars and
- text.

These additional data sets partly obscured in the images the original radar data. Therefore, it was necessary to remove these unwanted data sets from the images before a quantitative analysis based on the images could be performed. This was done in three steps.

First, radar images which showed no reflectivity data were selected. These were then used to assemble a template (Figure 2.2) that contained only those pixels which belonged to the additional data listed above. In a second step, all pixels marked in the template were removed from all radar images. Step three was to restore the radar data formerly obscured by the unwanted data. The missing pixels were generated from the maximum reflectivity of the surrounding pixels using an eight-neighbor-search algorithm.

2.2.2 Decoding Reflectivity Values

Another factor which needed attention resulted from the nature of GIF-images. The Graphics-Interchange-Format uses indexed color tables to display the colors of an image. That means that each color (which is assembled from three channels - red, green and blue) is given a unique color index (0-255). Unfortunately, the index for a certain color varied between the radar images. This complicated the identification of the different reflectivity values in the images as each color corresponds to a reflectivity value. This problem could be resolved by using the color bar in the lower left corner of the radar images (Figure 2.1) to synchronize the color indices and the reflectivity values.

Finally, the corrected radar images (Figure 2.3) were stored for further analyses.

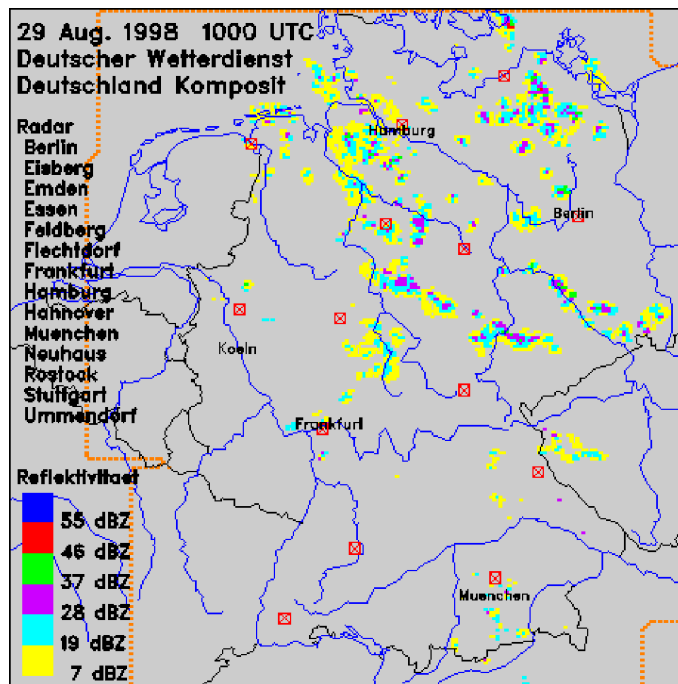


Figure 2.1: Radar image from 29 August 1998, 10 UTC.

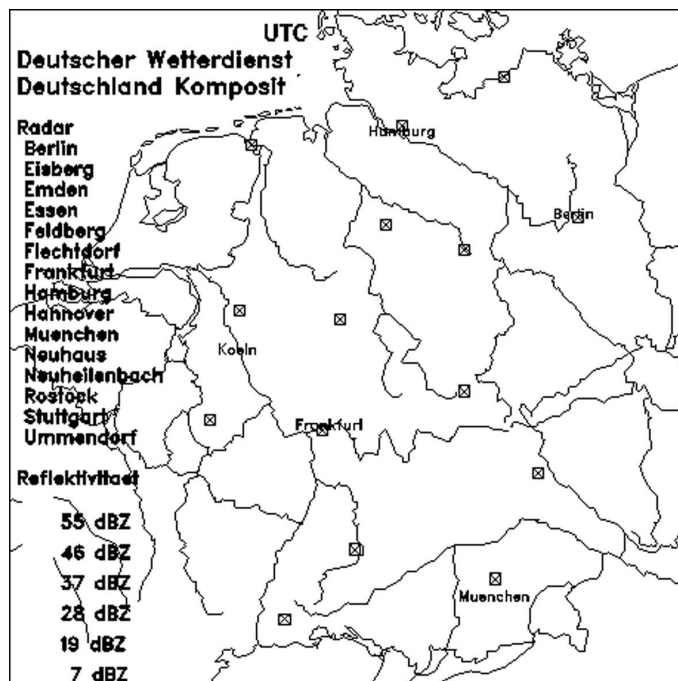


Figure 2.2: Template containing the river, border, coastline, radar location and text data.

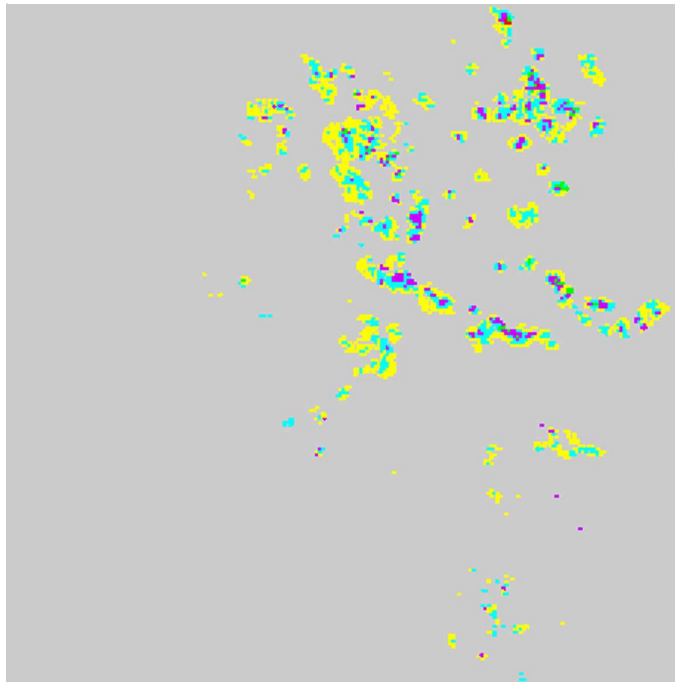


Figure 2.3: Corrected radar image from 29 August 1998, 10 UTC.

2.2.3 Segmentation

The segmentation of the precipitation field into convective and stratiform precipitation was performed using a subjective approach. A specially designed graphical user interface (GUI) enabled to review consecutive radar images as a film and to draw manually a boundary around the area with convective precipitation. Despite the routinely applied clutter filters (cf. Section 2.1.1; DWD (1998)), spurious echoes were still present in the analyzed data sets. Whenever possible, these were eliminated during the segmentation process to prevent biasing of the data set. Though, it is likely that clutter could not be entirely removed. All pixels inside the boundary line were kept for analyses while all others were deleted from the data set. The remaining data were then stored in a final, corrected and segmented, radar image. The whole process is depicted in Figure 2.4.

2.3 Data Analysis - Basic Parameters

One of the main objectives pursued in this thesis is the mathematical description of a rain field. MESNARD and SAUVAGEOT (2003) describe in detail the related problems. Many different approaches have been proposed in the past

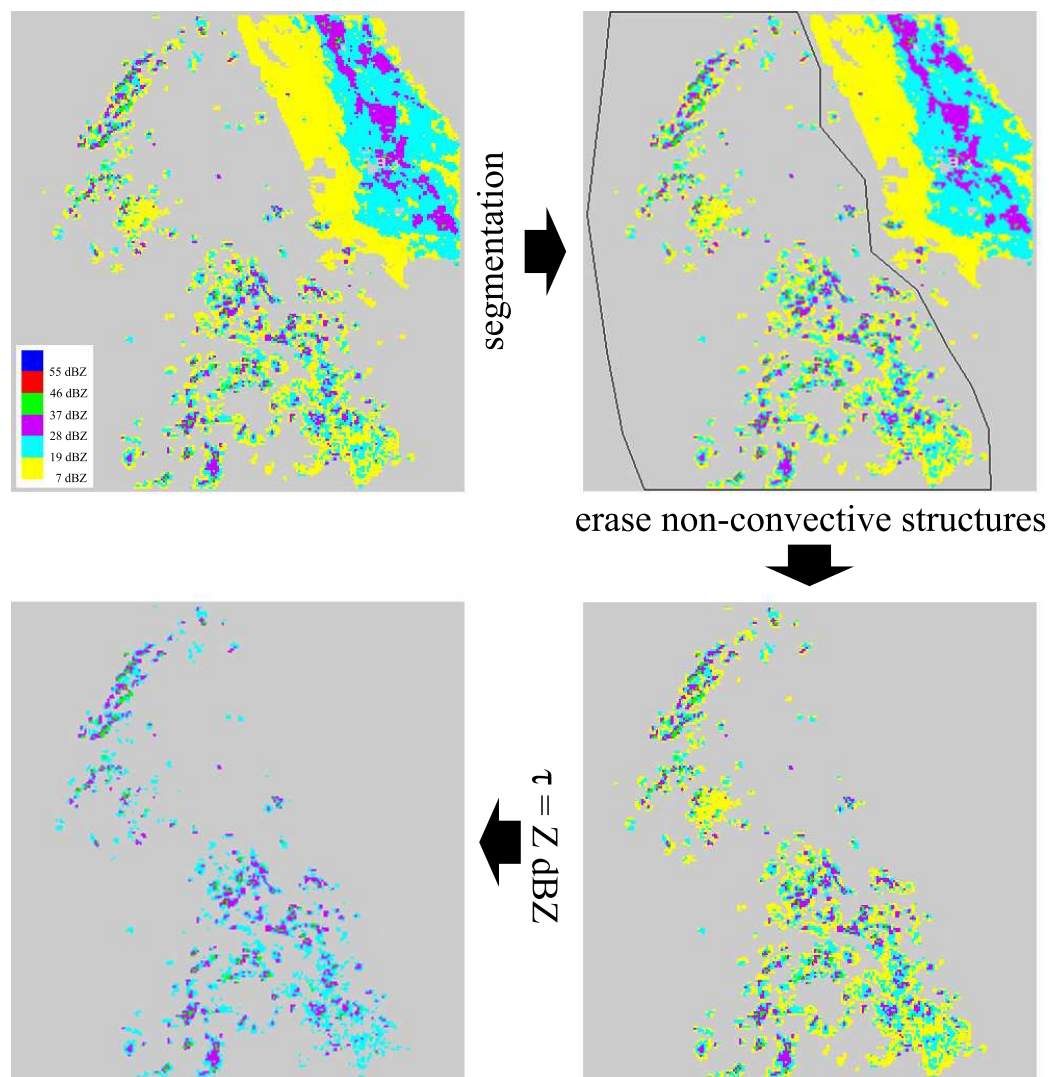


Figure 2.4: Schematic representation of the segmentation process. The process begins (upper left) with a corrected radar image (see section 2.2). The corrected radar image is then segmented using all the supplementary data described in section 2.1.2 (upper right). All unwanted data are deleted afterwards (lower right) and, if desired, a threshold value τ ($Z = 19$ dBZ) applied to the remaining data (lower left).

resulting in large differences in terminology. The terminology followed here is the one proposed by MESNARD and SAUVAGEOT (2003), GOLDHIRSH and MUSIANI (1986) and DRUFUCA (1977). They define a contiguous rain area as the area inside which the reflectivity Z (or rain rate R) $\geq \tau$, where τ is an arbitrary threshold value.

Due to the six-step reflectivity nature of the radar images, the choice for the threshold values is limited to the thresholds used by the DWD. These are

7, 19, 28, 37, 46 and 55 dBZ and were used as cut-offs for the radar images, ie. to determine the statistics of the rain field for different values of τ (it is reported by MESNARD and SAUVAGEOT (2003) and other authors that the statistics of the rain fields depends on the threshold value). To find out which of the thresholds could be used, it was investigated how many pixels existed in the segmented radar images with a reflectivity value Z higher than a given threshold τ . If one considers the number of pixels with $Z \geq 7$ dBZ as a reference, 50.5% of these pixels have a reflectivity higher than $Z = 19$ dBZ. The numbers for the other values of τ are given in Table 2.2. It can be seen that the number of pixels with $Z \geq \tau$ quickly decreases with increasing τ . For $\tau \geq 46$ dBZ so few pixels are found that an analysis is no longer statistically sensible.

Table 2.2: Relative number of pixels with a reflectivity value higher than τ . The number of pixels with a reflectivity higher than 7 dBZ is used as a reference.

τ	fraction (%)
7	100.00
19	50.48
28	19.53
37	4.80
46	0.74
55	0.04

Before choosing certain thresholds for the analyses, it is also important to know which threshold corresponds to which feature of a deep convective cloud. Using the DWD's standard Z - R relation

$$Z = 256R^{1.42} \quad (2.1)$$

yields rain rates of approximately 0.06, 0.4, 1.9, 8.1, 34.9 and 150.4 mm h⁻¹, respectively. According to MESNARD and SAUVAGEOT (2003) these rain rates correspond to the following features of the convective cells: The lowest rain rate ($R = 0.06$ mm h⁻¹) represents the outermost regions of the precipitation field which envelopes the cores of convective precipitation (e.g. like the anvil of a Cb, see Figure 1.2). It also corresponds to a deep convective cloud at the beginning of its life cycle or in the decaying phase. The 2nd and the 3rd rain rate are the transition between the aforementioned features and the areas of heavy precipitation in the centers of the deep convective cells. The latter can be resolved using rain rates higher than 5 mm h⁻¹ as a threshold and is suitable to separate the dynamical part of the cloud from the advective part (e.g. anvil). The effect that the use of these different thresholds has is schematically shown in Figure 2.5. A threshold of $\tau = 7$ dBZ results in many large rain areas consisting of the convection cells enveloped by the peripheral regions of low rain rates. Using $\tau = 19$ dBZ already removes

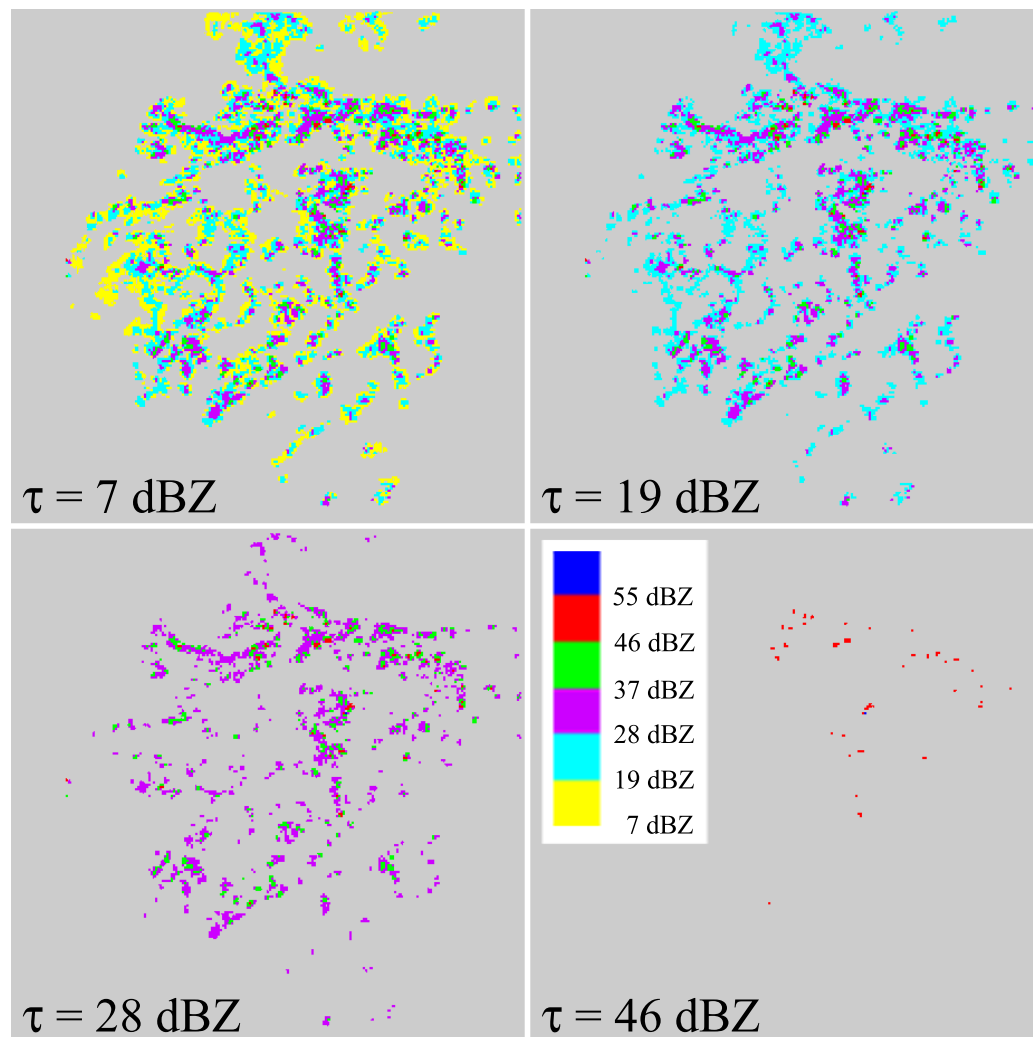


Figure 2.5: Application of different thresholds to the radar images. When a threshold of $\tau = 19$ dBZ is applied to the original radar image (upper left), the envelope of low reflectivity values is removed and the rain areas are broken up into smaller units. Using thresholds $\tau > 19$ dBZ further breaks up the rain areas until only the centers of the strongest convection cells remain. The number of rain areas is greatly reduced in this process.

much of the low rain rate envelope and breaks up the large rain areas in many small ones. For even higher threshold values, the remaining rain areas are further broken up into smaller units until only the centers of the strongest convection cells remain. In this process, the number of rain areas is greatly reduced for $\tau > 19$ dBZ (analogous to the small number of pixels with high reflectivity values reported above).

For the reason given above, only 7, 19, 28 and 37 dBZ were finally used

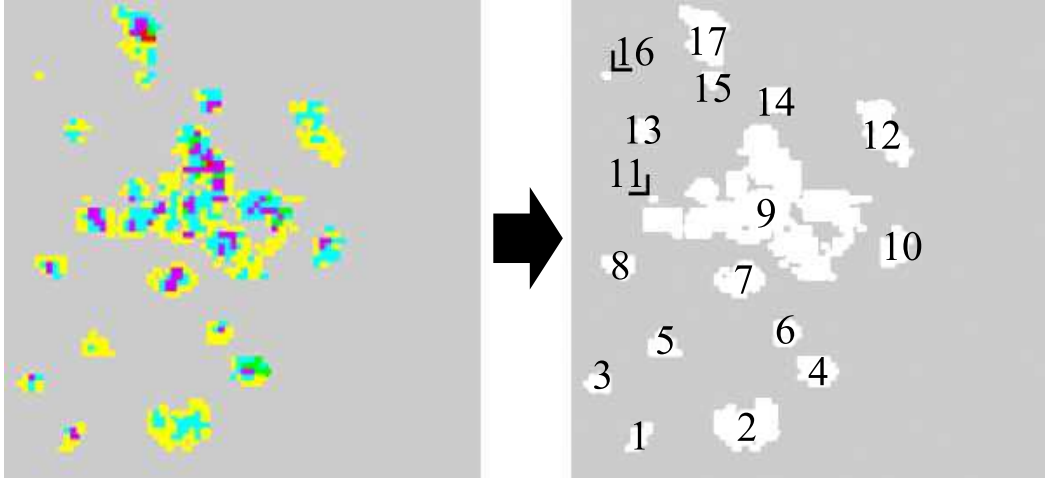


Figure 2.6: Illustration of the labeling process. The left image shows an unlabeled radar image. To the right the contiguous rain areas (white) are shown. The pixels of each rain area are labeled with the unique region index next to or above the rain area.

to calculate the basic parameters described below as they provide information on different aspects of the convective rain fields combined with a solid statistical basis.

To identify the contiguous rain areas in the radar images all pixels with reflectivity (rain rate) lower than a given threshold τ were deleted. Then, a four-neighbor-search algorithm was used which labels each rain area with a unique region index. This means that each pixel belonging to a certain rain area is labeled with the same index i . This enables to distinguish separate rain areas and to calculate parameters for a each rain area. The labeling process is illustrated in Figure 2.6. The region index i is of type unsigned integer with $0 < i \leq N_A$, where N_A is the number of rain areas present at a certain given time (in one radar image) or at a certain given time of day (in all the radar images recorded at the same time of day).

2.3.1 Definitions

Rain Area Specific Parameters

The area A_i of a rain area with region index i can be obtained by simply counting the number of pixels n_i with the same region index and multiplying the result with the pixel size $A_{px} = 4 \text{ km}^2$:

$$A_i = n_i \cdot A_{px}. \quad (2.2)$$

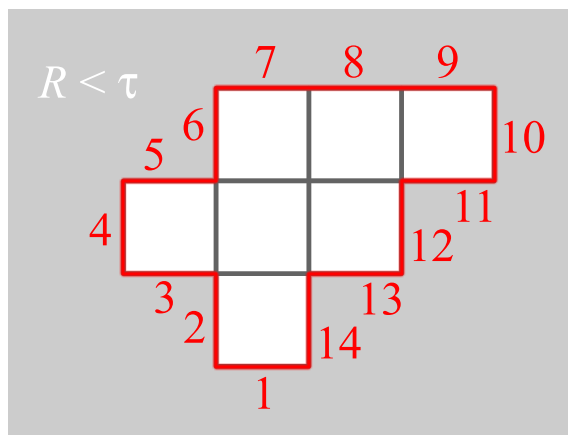


Figure 2.7: Illustration of the process to determine the perimeter of a rain area. Each pixel of a radar image has four sides. Only those sides (red) of the pixels of a rain area (white area) are counted that border pixels with $R < \tau$ (gray area). In this case the rain area has a perimeter of 14.

As only pixels with non-zero reflectivity values are labeled with a region index, pixels with $R < \tau$ enclosed by pixels with $R \geq \tau$ do not contribute to the area A_i of a rain area.

The equivalent circular diameter (equicircle diameter) D_i of a rain area i follows from a simple transformation of A_i :

$$D_i = \sqrt{\frac{A_i}{\pi}}. \quad (2.3)$$

It is the diameter of a circular rain area with an area of A_i . The parameter D_i is frequently used in the literature instead of A_i (see section 1.4). To allow for comparability it is used in this thesis as well.

The perimeter U_i of each rain area i was calculated by counting all those sides s_i of the pixels of a rain area which bordered pixels with $R < \tau$ (cf. Figure 2.7). This also applies to areas with $R < \tau$ inside the rain area. Therefore:

$$U_i = s_i \cdot \sqrt{A_{px}}. \quad (2.4)$$

The determination of the number p_i of reflectivity peaks of a rain area i was not as straight forward as described by (MESNARD and SAUVAGEOT 2003). This is caused by the six-step nature of the radar images. It leads to a permanent underestimation of p_i . In contrast to a rain area that exhibits several peaks in the case of a continuous distribution of reflectivity, the same rain area could only show one peak when the six-step scale is used (this is schematically shown in Figure 2.8). However, a close inspection of the radar images revealed that most of the peaks could still be identified with

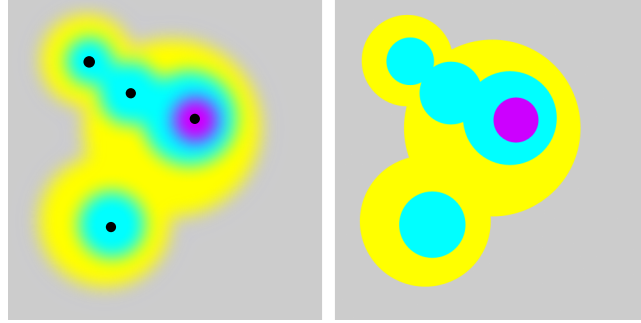


Figure 2.8: Schematic representation of a radar image with continuous reflectivity scale (left) and the same image using discrete reflectivity values (right). The black dots mark the locations of relative maxima of reflectivity (peaks) which cannot be found in the case of discrete reflectivity values.

an algorithm that uses a two-dimensional Gauss-filter that smoothens the radar images (equivalent to proceeding from right to left in Figure 2.8). All pixels are considered to be peaks which have a greater reflectivity value than their 8 neighbors. How many peaks are found then depends on the standard deviations σ_x and σ_y used for the filter (the larger σ_x or σ_y , the stronger the smoothing). If the standard deviations are too large, the smoothing is too strong and less peaks are found. The same is the case when the smoothing is too soft.

To find the optimum choice for $\sigma_x = \sigma_y$ a test data set of radar images with a spatial resolution of 1 km and 0.5 dB steps was retrieved from the DWD. From these high resolution images, two different sets of images were computed. The first set (S1) consisted of images that were simply scaled down to a resolution of 2 km. For the second set (S2), the images were also scaled down to a resolution of 2 km, but, additionally, the reflectivity values were adjusted to the six discrete values of the DWD's PC product (see Section 2.1.1). These two sets were then used to compare the number of reflectivity peaks found in images with 0.5 dB reflectivity steps (S1) and the six-step dBZ images (S2). A filter with $\sigma_x = \sigma_y = 1$ Pixel proved to be the optimum choice to recover the reflectivity peaks in S2. The number p of reflectivity peaks found in S2 by the algorithm deviated by a maximum of 10% from the ones present in the high resolution images S1.

The distance e_{ij} between a peak and its nearest neighbor (undefined for $p_i = 1$) within the same rain area also was of interest. The distances were computed using Delaunay triangulation (BURT and SCHACHTER 1980). A Delaunay triangulation decomposes a planar set of points into triangles (Figure 2.9). Each triangle has the property that its circumcircle does not contain any points within. This makes it the ideal tool to determine the distances between the nearest points only. As there are p_i peaks in the rain area, a set \mathbb{E}_i of p_i distances can be composed for each of the rain areas:

$$\mathbb{E}_i = [e_{i1}, \dots, e_{ip_i}] \quad (2.5)$$

with

$$e_{ij} = \min \left(\sqrt{(\mathbb{X}_{ij} - x_{ij})^2 + (\mathbb{Y}_{ij} - y_{ij})^2} \right), \quad (2.6)$$

where x_{ij} and y_{ij} ($j = 1, \dots, p_i$) are the x- and y-coordinates of the j^{th} peak of the i^{th} rain area. \mathbb{X}_{ij} and \mathbb{Y}_{ij} are sets of x- and y-coordinates of the peaks connected through the Delaunay triangulation to the j^{th} peak of rain area i (see Figure 2.9).

A set of distances \mathbb{E} can then be used to calculate the nearest neighbor distribution (NND) for each peak number separately. \mathbb{E} includes all nearest neighbor distances of rain areas with a given peak number p_0 (at a certain time or period of time):

$$\mathbb{E} = [\mathbb{E}_1, \dots, \mathbb{E}_{N_{A,p}}], \quad (2.7)$$

where $N_{A,p}$ is the number of rain areas with $p = p_0$. A NND independent of p can also be derived. In that case i denotes the time index of a certain radar image and not the region index of a rain area.

Parameters Related to the Area and Peak Number of Rain Areas

From the rain area specific values, sums of these values can be computed at a certain given time.

The total rain area A_{total} at a given time was determined by:

$$A_{total} = \sum_{i=1}^{N_A} A_i, \quad (2.8)$$

where N_A is the number of rain areas found for the selected time (see above).

The total number of peaks n_p , or total number of convection cells, is calculated as follows:

$$n_p = \sum_{i=1}^{N_A} p_i, \quad (2.9)$$

where p_i is the peak number of the i^{th} rain area.

From the three parameters A_{total} , n_p and N_A another three parameters can be derived:

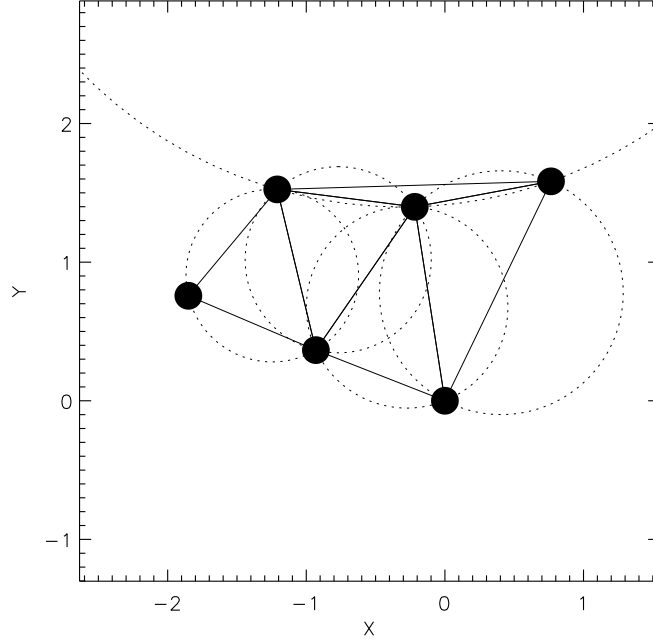


Figure 2.9: Delaunay triangulation of a set of six points (black dots). The set is decomposed into five triangles (solid lines). Their circumcircles (dashed lines) do not contain any of the set's points.

The average area per rain area A_r is given by

$$A_r = A_{total}/N_A. \quad (2.10)$$

The average area per peak A_{max} is

$$A_{max} = A_{total}/n_p. \quad (2.11)$$

The average number of peaks per rain area n_r is given by

$$n_r = n_p/N_A. \quad (2.12)$$

Frequency Distributions

In the main parts of this thesis power laws and log-normal functions are frequently used to describe functional dependencies of various parameters.

A power law is a function of the form:

$$F(x) = a \cdot x^b. \quad (2.13)$$

The parameters a and b of this function can simply be determined by linear regression if the equation is transformed to

$$F^*(x) = a^* + b \cdot x^*, \quad (2.14)$$

where $F^*(x) = \log F(x)$, $a^* = \log a$ and $x^* = \log x$.

One of the functions that was found to frequently represent the frequency distributions of various hydrological parameters (x) is the log-normal function. It is represented by:

$$P(x) = \frac{1}{x \cdot \sigma \sqrt{2\pi}} \exp \left[-\frac{(\ln x - \mu)^2}{2\sigma^2} \right], \quad (2.15)$$

where μ and σ are the mean and standard deviation of $\ln x$ (CROW and SHIMIZU, 1988), given by

$$\mu = \ln \bar{x} - \frac{1}{2} \ln \left(1 + \frac{s^2}{\bar{x}^2} \right) \quad (2.16)$$

and

$$\sigma = \sqrt{\ln \left(1 + \frac{s^2}{\bar{x}^2} \right)}, \quad (2.17)$$

where \bar{x} and s are the mean and standard deviation of x (MESNARD and SAUVAGEOT, 2003). Reciprocally,

$$\bar{x} = \exp \left(\mu + \frac{1}{2} \sigma^2 \right) \quad (2.18)$$

and

$$s = \sqrt{\exp(2\mu + \sigma^2) (\exp \sigma^2 - 1)}. \quad (2.19)$$

Fourier transformation was used to fit the diurnal cycles of some of the variables. Fourier transformation assumes that any periodic function $f(t)$ can be represented by a sum of cosines:

$$f(t) = \frac{a_0}{2} \left(1 + \sum_{n=1}^{\text{inf}} (2a_n/a_0 \cdot \cos(n\omega t + \phi_n)) \right), \quad (2.20)$$

where a_0 and a_n are scaling parameters and ϕ_n is an off-set parameter. In this thesis, parameters for $1 \leq n \leq 4$ were found to be sufficient to represent the analyzed data sets very well.

Chapter 3

Results

In the Methodology section, it was described that the different reflectivity values correspond to different features of the convective rain field. Low values of τ emphasize the outermost regions of the convection cells (or infant or decaying convection cells), while the higher reflectivity values correspond to the heavy precipitation regions at the core of the convection cells. In the following main sections of this thesis, each presented parameter was analyzed taking into account the four selected threshold values. First, the main features of each parameter are described followed by a description of the differences resulting from the threshold values. The main focus is laid on $\tau = 19$ dBZ as this threshold value includes features of both the cores and the outer regions of the convection cells but already distinguishes between the dynamical and advective part of the cloud. Another reason is that the statistical basis for this threshold is much better than for higher threshold values (cf. section 2.3). For some investigations which concentrate on short time scales (1 hour, 1 day) or small regions the lowest threshold, $\tau = 7$ dBZ, is used as only then enough rain areas are available for analysis.

The following sections are structured as follows: First (section 3.1), the diurnal variation of the numbers of rain areas and reflectivity peaks are described. This is followed by an analysis of the peak number distribution and its diurnal and spatial variation (section 3.1.2). Afterwards (section 3.2), the rain areas' sizes and related entities and their diurnal variation are presented, before the rain area size distribution is described. In the third large section (section 3.3), the distances between the peaks are investigated including the nearest and all neighbor distributions. The chapter concludes with section 3.4 where the fractal dimension of the rain areas is deduced.

3.1 Rain Area Number and Peak Number

3.1.1 Diurnal Variation of the Numbers of Rain Areas and Reflectivity Peaks

The average diurnal variation of the number of rain areas N_A is displayed in Figure 3.1. It shows a typical cycle of convective activity with a minimum at night and a maximum about one hour after local noon. The same is evident for the diurnal variation of the total number of convection cells n_p (Figure 3.2) which is obtained by counting all the reflectivity peaks at a certain time (see section 2.3.1). While low numbers of n_p prevail at night, the number of peaks quickly increases after sunrise. The maximum is reached at about 12:30 UTC, the time of local noon. The number of peaks then steadily decreases until the minimum values are reached at night. The relative change in numbers between night and day is quite dramatic. At noon, the number of peaks is six to ten times higher than at night, depending on the cut-off. These observations fit nicely if solar insolation is considered as the main cause, but not the only cause. If surface heating was considered, the maximum convective activity would be expected in the afternoon, the time of highest surface temperature (EMANUEL 1994). A coherent diurnal

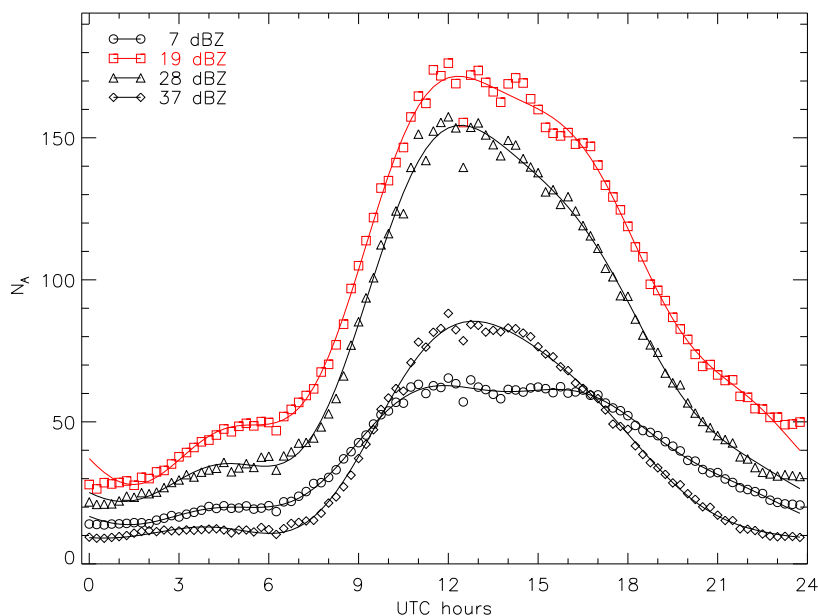


Figure 3.1: Average diurnal variation of the number of rain areas for four different cut-offs. The solid lines represent the corresponding data assembled from the first four frequencies of the Fourier transform.

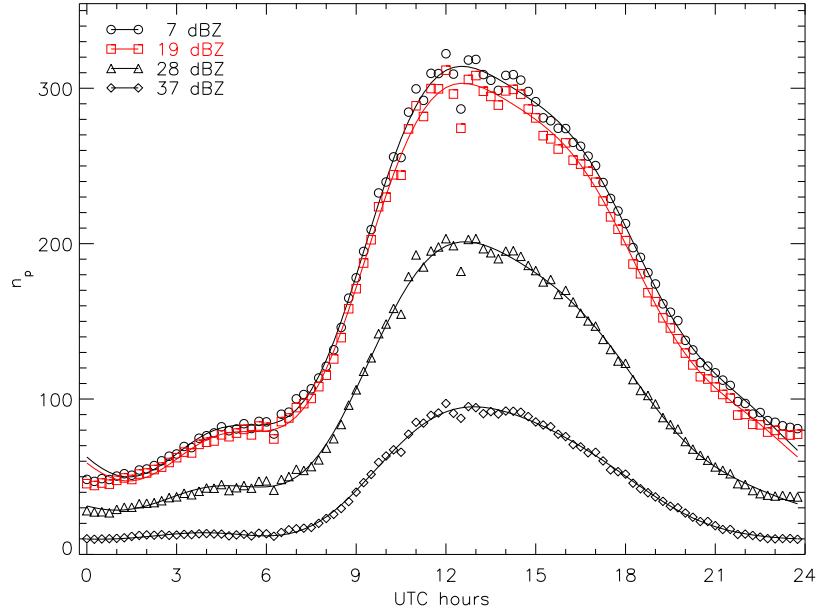


Figure 3.2: Average diurnal variation of the number of peaks for four different cut-offs. The solid lines represent the corresponding data assembled from the first four frequencies of the Fourier transform.

march of convective activity over land surfaces with a maximum around local noon (e.g. GRABOWSKI *et al.* 2006) or in the afternoon (e.g. GARREAUD and WALLACE 1997) is frequently reported. However, it is also known (STIRLING and PETCH 2004) that factors like temperature and moisture distribution at the surface or in the boundary layer can shift the time of maximum convective activity by several hours. Other factors like orography (e.g. OHSAWA *et al.* 2001) also play an important role in that respect (see Section 1.1 for a detailed description).

The two aforementioned parameters (N_A and n_p) can be combined to determine how many convection cells are contained in one rain area on average (n_p/N_A) and what the diurnal variation of this parameter n_r looks like (Figure 3.3). The surprising result is that there is almost no variation observed for most of the cut-offs. Obviously, the numbers of rain areas and reflectivity peaks change in such a way over the day that a constant ratio is preserved. This behavior is unexpected and has so far not been reported in the literature. It is further investigated in Section 3.1.2.

The curve of N_A for a cut-off of $\tau = 7$ dBZ is markedly different from the ones of the other cut-offs. Instead of a single peak, a plateau stretches from approximately 11 UTC to 17 UTC. The numbers of rain areas for the different cut-offs show great differences, too. The largest numbers are found for $\tau = 19$ dBZ, and not for $\tau = 7$ dBZ, with circa 170 rain areas present in

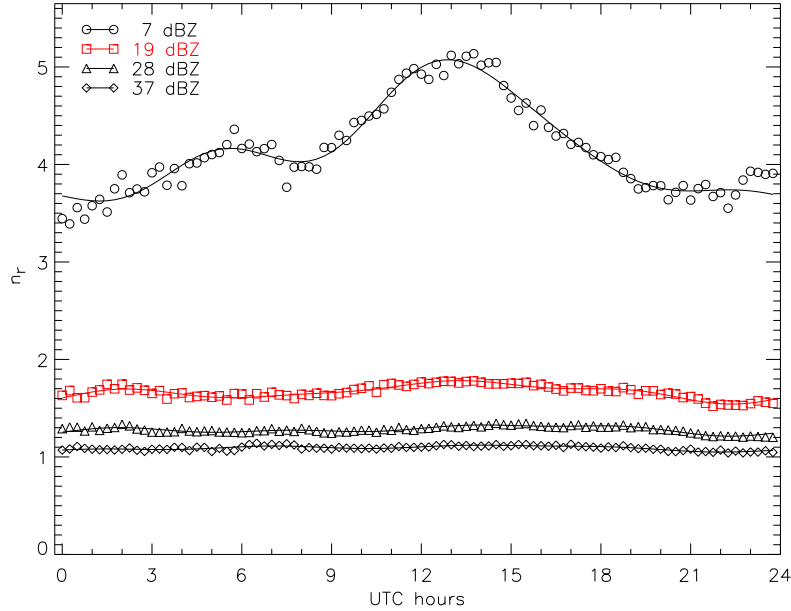


Figure 3.3: Average diurnal variation of the number of peaks per rain area for four different cut-offs. The solid lines represent the corresponding data assembled from the first four frequencies of the Fourier transform.

the investigated domain at noon. This is, obviously, due to the structure of the rain fields, where a "fog" of low reflectivity values (mainly resulting from the anvils of the fully developed Cbs, see Section 1.1), respectively low rain rates, envelopes the cores of the convection cells and their high reflectivity values. If the lowest level of reflectivity is removed, the cores of the convection cells are exposed and a formerly large rain area is broken up into many small ones. This shows that it is appropriate to use a cut-off of 19 dBZ or higher to obtain a clear convective signal (as already described in section 2.3). It can also be seen that most of the rain areas with $\tau \geq 19$ dBZ contain rain areas with $\tau \geq 28$ dBZ, too, as there are almost equal numbers of them. Rain areas with higher reflectivity values are already much rarer. However, the ratios between the rain area numbers at night and at noon indicate that rain areas with high reflectivity values are more frequent, on a relative basis, during the daytime, as is expected from the convective cycle. The data presented in Figure 3.1 can all be very well reproduced by using the first four frequencies of their fast Fourier transform (FFT). The relevant parameters are all given in Appendix B.

The diurnal cycles of the total number of peaks n_p are all very similar, with respect to their shape. It is a result of the overlying convective diurnal cycle, as explained above. The absolute amplitude, however, is very different for the four cut-offs. It decreases with increasing cut-off. This is a

consequence of the removal of a certain number of pixels with each increase in cut-off. It can also be noted that there are almost as many peaks for $\tau = 19$ dBZ as for $\tau = 7$ dBZ. It shows that about 95% of the convection cells found for the lowest cut-off include higher reflectivity values as well. This reinforces that a cut-off of $\tau = 19$ dBZ is sufficient to detect the convection cells.

The average number of convection cells per rain area (n_r) behaves like N_A . The diurnal cycle of n_r for $\tau = 7$ dBZ is an exception. It is clearly due to the characteristics of the diurnal cycle of N_A with a plateau around noon. Therefore, the found feature is clearly linked to the convective signal, but not to the low reflectivity envelope. From the average value of n_r , it is evident that the average rain area consists of one to two convection cells, implying that only few rain areas with a high peak number exist. For $\tau = 37$ dBZ, the ratio between unicellular rain areas and those with $p > 1$ is higher than 10:1, hence, about 90% of the rain areas are single cells. Only for $\tau = 7$ dBZ, n_r is markedly higher, a consequence of the structure of the rain areas (convection cell cores / low reflectivity envelope) as described above and in section 2.3.

3.1.2 Peak Number Distribution

In the above section, the diurnal variation of the number of rain areas and reflectivity peaks was analyzed. Evidence was found that most rain areas consist of a small number of convection cells, only. It was also detected that the number of convection cells per rain area remains constant over the day, despite a strong diurnal cycles in the absolute numbers of rain areas and convection cells.

For a more thorough investigation, the numbers of rain areas with the same number of peaks (p) have to be counted. The resulting PND, $P(p)$, shown in Figure 3.4, was computed considering the rain areas of all the selected days (see section 2.1.2) combined, independent of time. Additionally, the data were normalized with the total number of rain areas found for each cut-off. As expected, most of the rain areas are unicellular. The double-log representation of the data (Figure 3.4) indicates that a power law (cf. Equation 2.13)

$$P(p) = c_0 \cdot p^{d_0} \quad (3.1)$$

is appropriate for a fit. A least square fit of the double-log data confirms that a power law reproduces the data very well with a correlation coefficient of $r > 0.999$. The regression lines have been fitted to data points for relative frequencies of $P(p) > 5 \cdot 10^{-4}$. Below about that threshold, the numbers of rain areas are biased through the limited database of 39 days. This leads to a cut-off of the distribution for high peak numbers (the data points with the lowest relative frequency are represented only once for the respective peak number). The slope of the regression lines varies between $d_0 = -1.93$ and

Table 3.1: Coefficients of Equation 3.1 for the various thresholds. The curves have been fitted to data points with $P(p) > 5 \cdot 10^{-4}$. The value p_m represents the corresponding maximum peak number used for the fit.

τ [dBZ]	p_m	c_0	d_0	r
7	40	0.61	-1.93	1.00
19	18	0.64	-2.46	1.00
28	11	0.72	-2.94	1.00
37	6	0.89	-3.96	1.00

$d_0 = -3.96$. The parameter c_0 represents the fraction of unicellular cells. It varies between 61% for $\tau = 7$ dBZ and 89% for $\tau = 37$ dBZ. All relevant parameters are presented in Table 3.1. It is apparent how quickly the number of rain areas decreases with increasing p . Between $p = 1$ and $p = 10$ a decline by a factor of 100 ($\tau = 7$ dBZ) to 10,000 ($\tau = 37$ dBZ) is observed (Figure 3.4) as can also be seen from the computed exponents (Table 3.1).

So far only MESNARD and SAUVAGEOT (2003) investigated the peak number distribution for four selected radar stations. Two of which are located in France and another two in the African Tropics. The analyzed radar images covered a much smaller area than the radar composite used here and allowed to compute the PND down to a peak number of about 30-40. For Bordeaux, they report $c_0 = 0.60$ and $d_0 = -2.48$ for a cut-off of $\tau = 23$ dBZ. For $\tau = 39$ dBZ they obtain $c_0 = 0.83$ and $d_0 = -3.53$. Even though these authors used different cut-offs, their parameters are very close to the ones observed here for a much larger area. The other stations, however, exhibit different parameters for the power law. These are the African stations and Toulouse. All these have in common that they are from different climate regimes than Bordeaux and Germany. Therefore, results obtained for a certain region can probably not be transferred to other areas.

Physical causes for the development of the fractal frequency distribution could be found in the theory on self-organizing criticality. This theory predicts that extended dissipative dynamical systems (like Rayleigh-Bénard convection, GETLING 1998) have a power law as their spatial signature (BAK *et al.* 1987; BAK *et al.* 1988). However, the temporal signature of an SOC-system could not be found so far in this investigation.

PNDs of single days and single hours

The above presented PNDs were computed from the radar data of all days combined. Therefore, they represent the average conditions observed on the 39 selected days. The question arises whether these PNDs are produced by coincidence or if similar behavior can be established on single days as well. In

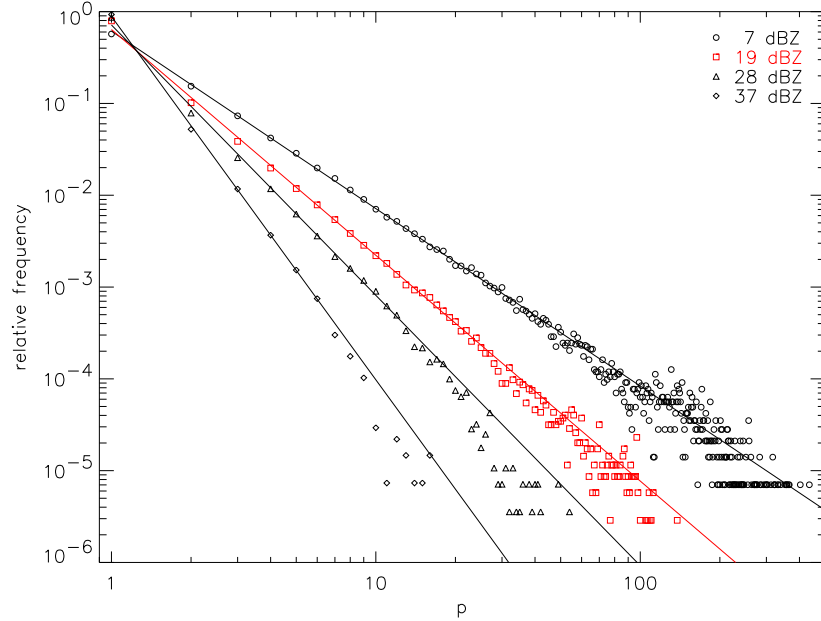


Figure 3.4: Peak number distribution for four different cut-offs. The data of each cut-off are normalized with the total number of rain areas found for that cut-off. The solid lines represent the corresponding regression lines.

the following, data of single days and also single hours are assessed. Again, the frequency distribution of each investigated period is normalized with the total number of rain areas present during that period.

The observed data sets show a large day-to-day variability in terms of the maximum peak number observed. On one of the days (1997/06/14), very large multicellular rain areas ($p > 130$) were detected, on two other days (1997/05/28; 1998/06/18) the maximum was $p = 11$ (cf. Appendix C). This makes clear that the day-to-day variability stretches over an order of magnitude. Figure 3.5 portrays PNDs of four single days. It is obvious that they can all be fitted very well by power laws. This also applies to all other daily data sets. Due to the low number of rain areas available for the analysis on single days (compared to that of the 39 days combined), rain areas with large p are often found only once or twice, giving rise to a long tail of data to the right side of the distribution (cf. 1997/05/21, 12:00-12:45 UTC in Figure 3.5). Therefore, only data points with a frequency of $P(p) > 5 \cdot 10^{-3}$ were considered for the fit to prevent biasing. This procedure was undertaken for all of the investigated days. The bandwidth of exponents found is $d_0 = -3.37$ to $d_0 = -2.27$. The distribution is displayed in Figure 3.6. Its maximum is located at $d_0 = -2.5$, which was also found for the whole dataset. The distribution shows that values of most exponents range between -2.65 and -2.25 (31 of 39 cases). A larger number of days would have to be analyzed

to better describe this distribution, however. A detailed list of the PND parameters for each day is given in Appendix C.

The same analysis was also conducted for time-periods shorter than a day. This brought with it difficulties calculating reliable PNDs, as the number of available rain areas is greatly reduced. Nevertheless, two examples are shown in Figure 3.5. Distributions for one hour periods on 1997/05/21 and 1997/06/24 were analyzed between 12:00 and 12:45 UTC (four radar images). Even for such short time frames the PND can be fitted very well by power laws. Their exponents are close to $d_0 = -2.1$.

In summary it can be stated that power law distributions of the PNDs are found on all investigated time scales. The exponents of the power laws are different between the analyzed periods. Such analyses are not reported in the literature to the author's knowledge. As presented in Section 1.1, it is known that triggering of convection is subject to many factors like orography, density stratification of the atmosphere, moisture and temperature variations of the surface and many more. To find the same combination of effects on one day and on another one is highly unlikely. Therefore, it can be hypothesized that these parameters contribute to which frequency distribution emerges on a certain day (also currently investigated within the scope of a diploma thesis at the IMuK). This is further investigated in the following Section.

3.1.3 Diurnal Variation of the PND

It was also studied if the average PND presented in section 3.1.2 shows a diurnal cycle. If hourly data are considered, the average number of available data points for each frequency distribution is greatly reduced to approximately $1/24^{th}$. Each of the 24 distributions was normalized with the total number of rain areas detected within that hour to obtain the relative frequencies. This procedure also eliminates the diurnal cycle introduced by the variation of the number of rain areas (cf. section 3.1.1). The exponents of the power laws determined from the hourly PNDs, again, range between $d_0 = -2.38$ and $d_0 = -2.70$. Figure 3.7 displays the diurnal variation of the relative frequencies of the six lowest peak numbers. It can be seen that the relative occurrence of $p = 1$ to 4 remains constant over the day. Additionally, the variability increases towards larger p , which is certainly due to the lower number of rain areas available for the analyses. On average, the PND seems to be constant over the day. Variations of the computed exponents of the PNDs are obviously due to random fluctuations in the number of rain areas resulting from a limited data base. The result of a constant relative frequency distribution also implies that the convective diurnal cycle (which is responsible for the changing numbers of rain areas, see section 3.1.1) merely has a multiplicative effect on the distribution. Even though there are much more rain areas present around noon, the ratios between rain areas with certain peak numbers remain constant in the 39-days-average.

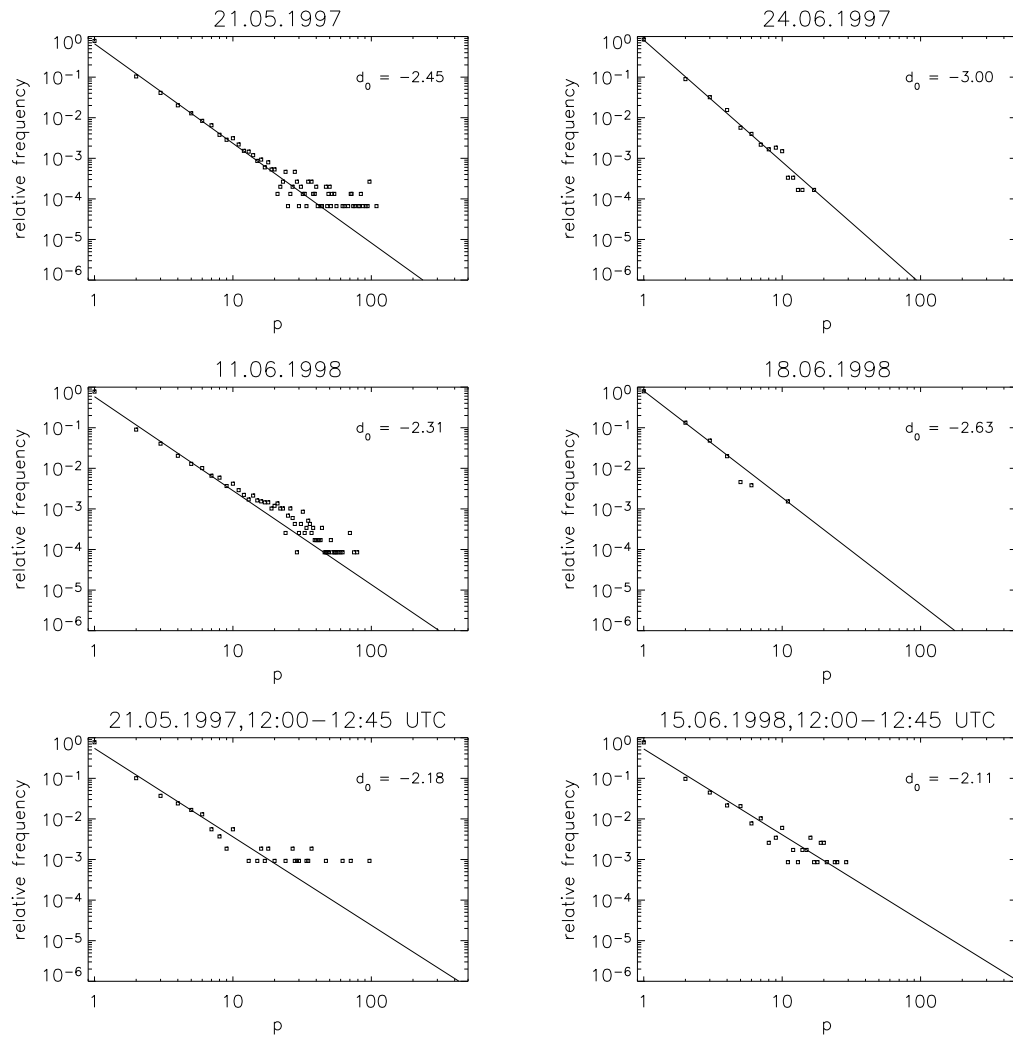


Figure 3.5: PND for single days (upper four diagrams) and hourly periods (lower two diagrams). A cut-off of $\tau = 19$ dBZ was used.

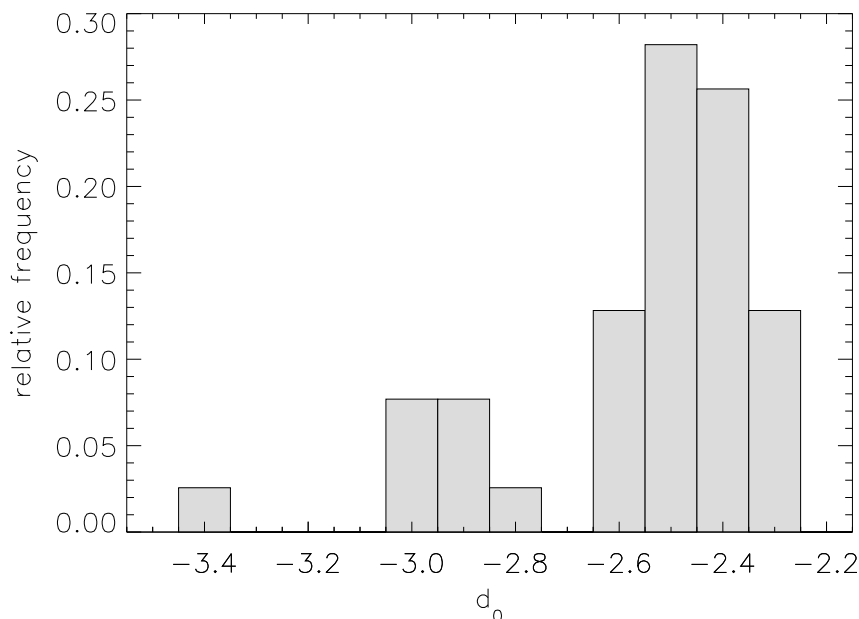


Figure 3.6: Frequency distribution of exponent d_0 (Equation 3.1). The distribution has been calculated for a bin size of 0.1.

To find out whether the results presented above are only coincidental and result from the combination of the 39 days, diurnal changes of the PND on single days were also checked. Though, this could only be done on days where enough rain areas were present during the whole 24-hour period. It is found that the findings presented above are also valid for these limited data bases. An example of which is given in Figure 3.8. Three-hour periods were used to reduce the amount of noise introduced by the limited amount of data. Despite some strong variability for large values of p , which was expected, it can still clearly be recognized that the relative numbers of unicellular rain areas and those with $p = 2$ and $p = 3$ remains fairly constant over the whole day. This indicates that, also on single days, the PND does not change markedly.

The finding from the previous Section that the PND *varies from day to day*, combined with the fact that it *does not vary on a certain day*, reinforces that a combination of parameters like the type of air mass and other boundary conditions (see above) have an influence on the population of rain areas that develops. A certain type of air mass that is advected behind a cold front usually has certain characteristics. However, these characteristics are different for different post-frontal situations.

The fact that the PND does not change over the day also explains why the average number of peaks per rain area was found to be almost constant as well. The total number of peaks at a certain time can be calculated by

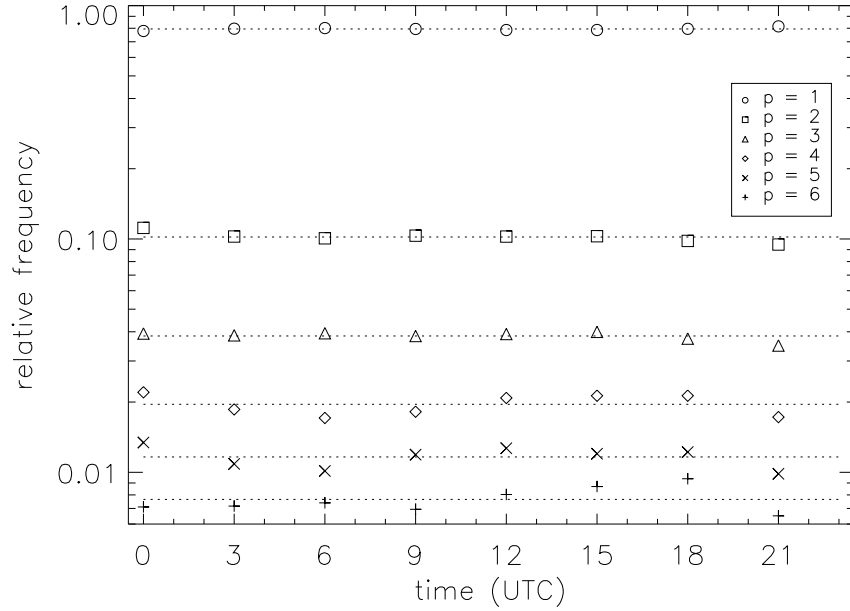


Figure 3.7: Diurnal variation of the average relative frequency of the six lowest peak numbers observed on the 39 selected days. The dotted lines show the corresponding mean relative frequencies.

Equation 2.9. It can also be obtained by

$$n_p = \sum_{p=1}^{p_{max}} N_A p \cdot P(p) = N_A \sum_{p=1}^{p_{max}} p c_0 \cdot p^{d_0}. \quad (3.2)$$

This can be plugged into the equation for n_r (Equation 2.12):

$$n_r = N_A \sum_{p=1}^{p_{max}} p c_0 \cdot p^{d_0} / N_A = \sum_{p=1}^{p_{max}} c_0 \cdot p^{d_0+1}. \quad (3.3)$$

Therefore, n_r only depends on c_0 and d_0 which themselves were found to remain almost constant on a certain day and for the average of the 39 days. Parameter n_r no longer depends on the number of rain areas. This is a direct consequence of the frequency distribution governing the population of rain areas, the power law.

3.1.4 Spatial Variation of the PND

Additionally to the diurnal variation, the spatial variation of the PND was analyzed. This was done using the following procedure: First, a certain peak

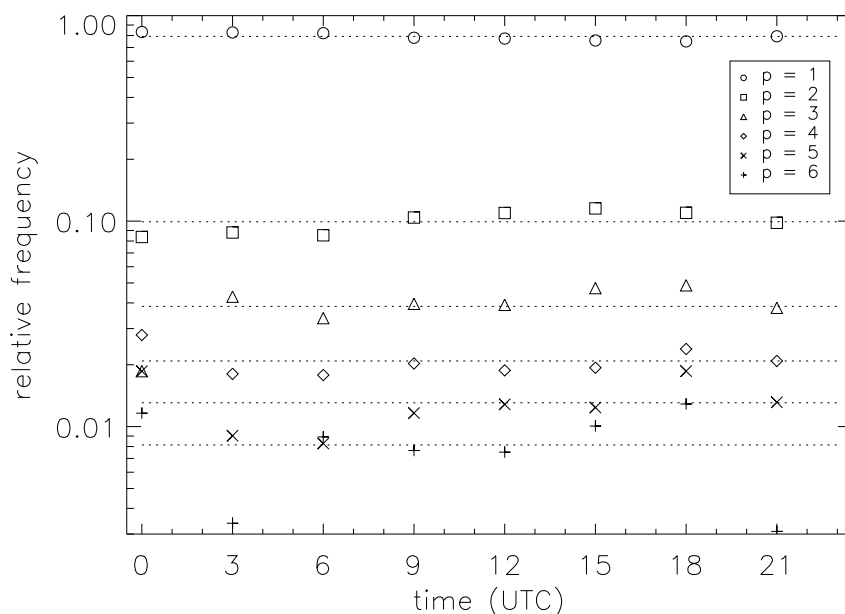


Figure 3.8: Diurnal variation of the relative frequency of the six lowest peak numbers on 21 May 1997 (3-hourly data). The dotted lines show the corresponding mean relative frequencies.

number or range of peak numbers was selected. Then all rain areas, which did not show such a peak number, were eliminated from the radar images. In a next step all radar images were overlaid and it was counted how often a pixel was covered by a rain area with the desired peak number. In doing so, it is possible to detect areas where certain types of rain areas preferably occur. Two figures show the spatial distribution of the occurrence of rain areas with $p = 1$ (Figure 3.9) and $32 \leq p < 64$ (Figure 3.10) for $\tau = 19$ dBZ, as an example. Obviously, unicellular rain areas more frequently occurred in Northern Germany than they do in the south on the 39 selected days. In the north they are found at a certain location in approximately 2% of all radar images. The same is true for rain areas with large peak numbers. They are present at a certain location in 2% of all radar images close to the North Sea coast, but rarely evolve further south. Similar results are evident for the other cut-offs.

It is also apparent (especially for $p = 1$, Figure 3.9) that the spatial distribution of the frequency of occurrence of rain areas is not smooth but marked by some pixels with a much higher frequency of occurrence than surrounding pixels. The observed effect is most likely due to clutter still present in the radar images as described in section 2.2.3.

The fact that the frequency of occurrence of deep convection over the investigated domain varies in space is most likely due to orographic ef-

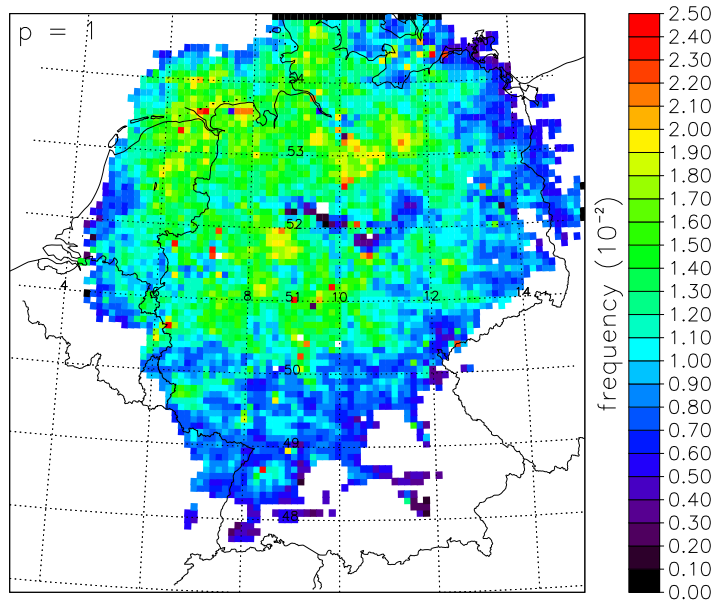


Figure 3.9: Spatial distribution of the frequency of occurrence of rain areas with $p = 1$ ($\tau = 19$ dBZ).

fects. Many authors report that roughness length changes between ocean and land (ALESTALO and SAVIJÄRVI 1985; ROELOFFZEN *et al.* 1986; ANDERSSON and GUSTAFFSON 1994), as well as effects from sea breeze circulations (VAN DE BERG and OERLEMANS 1985; WAKIMOTO and ATKINS 1994; ATKINS *et al.* 1995; KINGSMILL 1995; WILSON and MEGENHARDT 1997; BENNETT *et al.* 2006), can profoundly enhance convective activity. This is clearly reflected here by the more frequent occurrence of rain areas close to the coast.

To check now whether or not the PND differs in different regions of the investigated area, four domains were investigated. They have a north-south extension of 200 km and an east-west extension of 600 km. The location of the domains is shown in Figure 3.11. Domain 4 covers the coastal region where the largest numbers of rain areas with high peak numbers were detected. Domain 1 is located over Southern Germany where only few large rain areas were found. The other domains cover the transition of the Northern German low lands to the Central German highlands (Domain 3) and the highlands (Domain 2). For each of the domains, the PNDs and their parameters c_0 and d_0 (Equation 3.1) were calculated. The resulting PNDs are displayed in Figure 3.12. It can clearly be seen that, despite the great regional differences in numbers evident in Figures 3.9 and 3.10, there are only small differences between the relative frequencies. This is also confirmed by the parameters deduced for the PNDs, which are listed in Table 3.2.

The observed likeness between the PNDs and the differential in the fre-

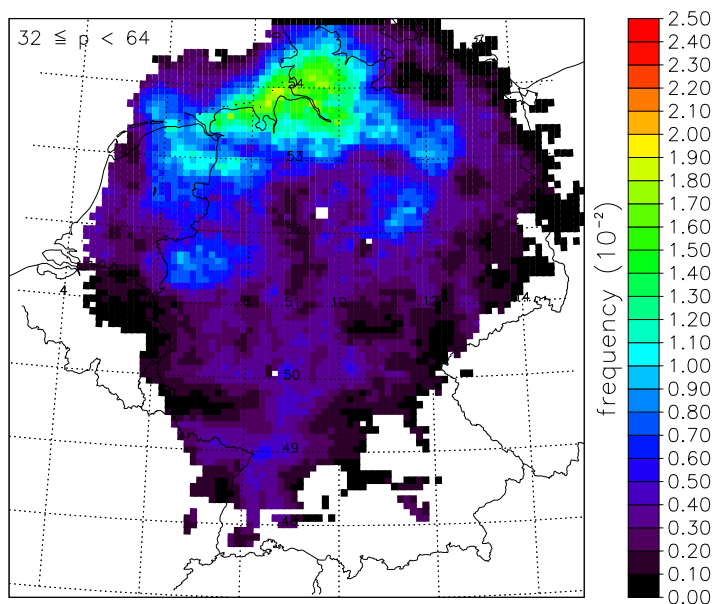


Figure 3.10: Spatial distribution of the frequency of occurrence of rain areas with $32 \leq p < 64$ ($\tau = 19$ dBZ).

Table 3.2: Coefficients of Equation 3.1 for the PNDs of Domain 1-4. The curves were fitted to data points of $1 \leq p \leq 18$.

Domain	c_0	d_0	r
1	0.57	-2.24	1.00
2	0.62	-2.32	1.00
3	0.60	-2.26	1.00
4	0.59	-2.23	1.00

quency of occurrence of rain areas with different peak numbers allows the conclusion that orography has the same effect in the whole investigated domain. This is in strong contrast to the change in terrain between the coast and the Alps in general, but also the soil heterogeneity in particular.

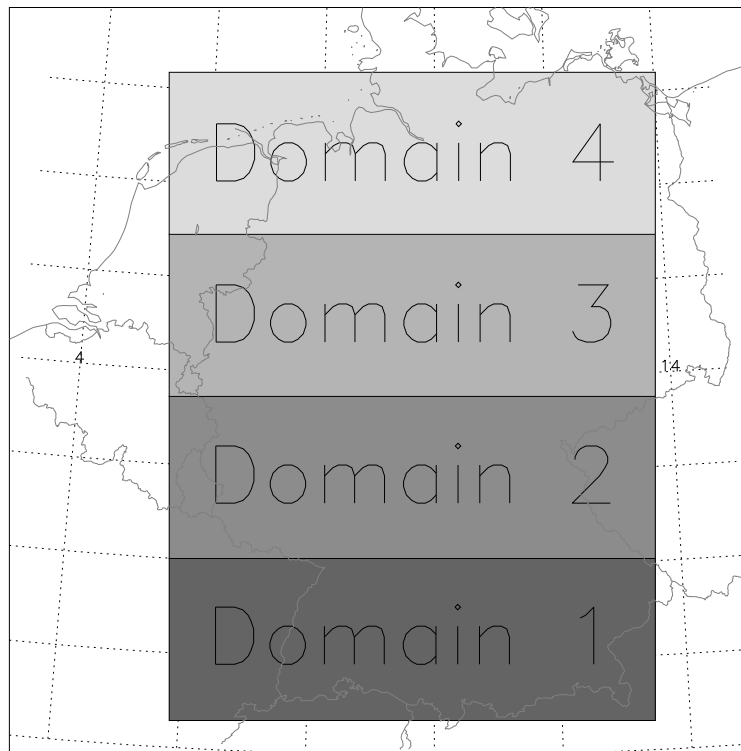


Figure 3.11: Geographical location of the domains used for the calculation of regional PNDs.

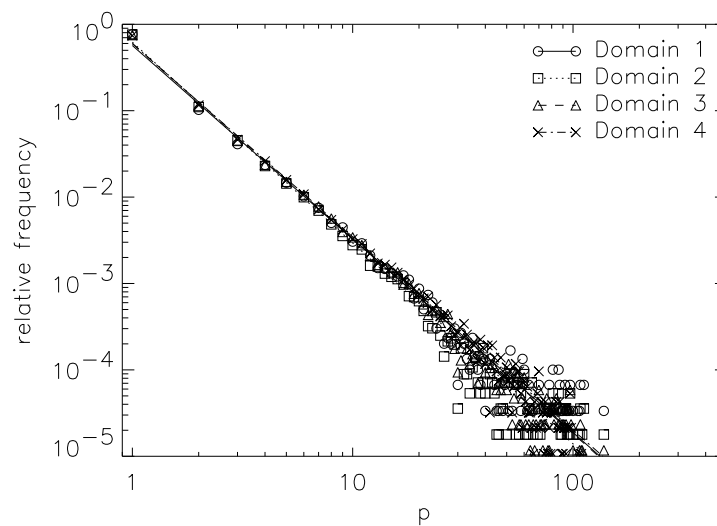


Figure 3.12: PNDs calculated for four regional domains (Figure 3.11). The lines represent the fitted power laws (Equation 3.1), the parameters of which are listed in Table 3.2. A cut-off of $\tau = 19$ dBZ was used.

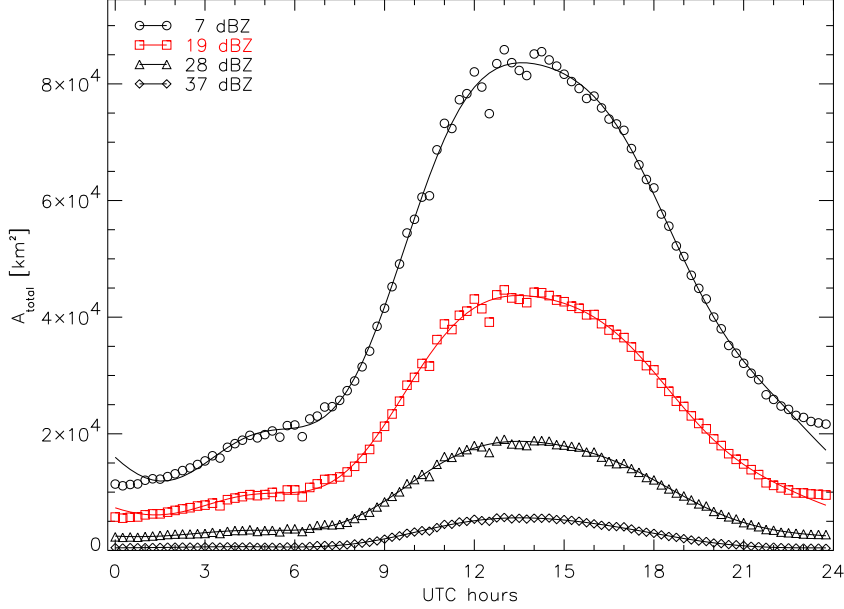


Figure 3.13: Diurnal variation of the average total rain area A_{total} for four different cut-offs. The solid lines represent the corresponding data assembled from the first four frequencies of their Fourier transform. A detailed list of the relevant parameters is given in Appendix B.

3.2 Size of the Rain Areas

Not only the numbers of rain areas and reflectivity peaks, respectively convection cells, are of interest, but also their spatial extension. In the following various parameters related to the size of the rain areas will be evaluated.

3.2.1 Diurnal Variations of the Total Rain Area and Related Entities

The diurnal variation of the average total rain area A_{total} (see section 2.3.1) is given in Figure 3.13. Similar to the total number of reflectivity peaks and rain areas (cf. section 3.1.1), the total rain area also follows a typical cycle of convective activity with a maximum shortly after local noon. All four data sets presented in Figure 3.13 show identical behavior. The discrepancy between A_{total} at night and at noon is quite large. Typically, there is a fivefold increase of A_{total} between those two points of time. In the evening, the convective area quickly decreases towards the minimum around midnight.

The observed diurnal behavior is a clear consequence of the diurnal cycle of convective activity (see Section 3.1 for a detailed explanation). As rela-

tively few rain areas are present in the morning, their combined size is small as well. This changes rapidly towards noon when more rain areas develop and the area covered by them increases, too. This is followed by a more gradual decrease in the evening, typical for convective activity (GARREAUD and WALLACE 1997).

The main difference between the four cut-offs is that the total area is the smaller the higher the cut-off. This is a consequence of the thresholding process. For $\tau = 7$ dBZ the average maximum extent is approximately $85\,000\text{ km}^2$ while it is only about $5\,000\text{ km}^2$ for $\tau = 37$ dBZ. Close inspection of the area values close to midnight reveals that there is a discrepancy (about $10\,000\text{ km}^2$ for $\tau = 7$ dBZ) between the end and the beginning of the time series. This results from the fact that single days and not consecutive ones were analyzed. Therefore, the time series are not necessarily periodic.

3.2.2 Diurnal Variation of the Average Rain Area Size

Data of the total area (A_{total} , see above) and the number (N_A , see section 3.1.1) of the rain areas can be combined to gain insight into the average size of each rain area A_r (cf. section 2.3.1) and its development during the day. Figure 3.14 shows that the average size of the rain areas remains almost constant during the day for $\tau \geq 19$ dBZ. However, there is a noticeable exception in the evening, when the average size of the rain areas is somewhat larger than during the rest of the day. These slightly larger sizes coincide with the most active decay phase (see e.g. Figures 3.13, 3.1 and 3.2). The life cycle of the Cbs provides an explanation for this observation. The horizontal extent of the area with precipitation particles within the deep convecting cloud is smaller for a mature Cb than for one in the dissipating stage (see Figure 1.1 and Section 1.1). This is due to transport of precipitation particles within the cloud and, especially, the weakening updrafts which cannot prevent precipitation from falling towards the surface within the whole cloud. Hence, the radar records a larger rain area during the dissipating stage than during the stages before. As the fraction of dissipating Cbs is the largest in the evening, the average size of the rain areas is slightly increased.

Only for $\tau = 7$ dBZ, a much strong variation is noticed. This is a consequence of the characteristics of the diurnal cycle of the number of rain areas for that threshold (Figure 3.1), for reasons already stated above. The average size of a rain area with $\tau = 19$ dBZ is 230 km^2 , 100 km^2 for $\tau = 28$ dBZ and 50 km^2 for $\tau = 37$ dBZ. This translates to average diameters of their quicircle areas of 17 km, 11 km and 8 km, respectively.

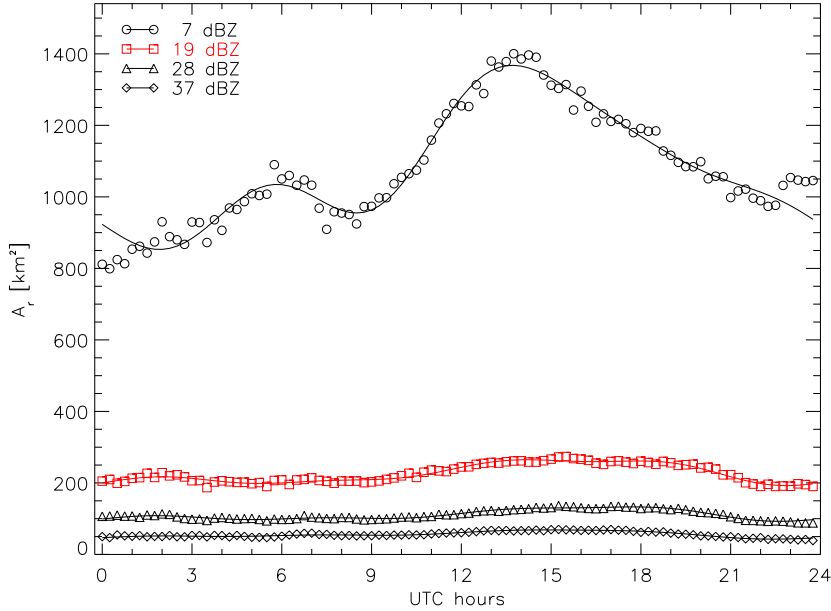


Figure 3.14: Diurnal variation of the average area per rain area A_r for four different cut-offs. The solid lines represent the corresponding data assembled from the first four frequencies of their Fourier transform. A detailed list of the relevant parameters is given in Appendix B.

3.2.3 Diurnal Variation of the Average Area Per Peak

The same analysis can be accomplished for the average area of reflectivity per peak (A_{max}). This is equivalent to the average size of the convection cells inside the rain areas. The result is almost identical to that obtained for the average rain area size (Figure 3.15). A slight variation is observed. The convection cells are slightly smaller at night and in the morning than later in the day for the reason given in the previous section. Their average size is approximately 260 km^2 ($\tau = 7 \text{ dBZ}$), 135 km^2 ($\tau = 19 \text{ dBZ}$), 85 km^2 ($\tau = 28 \text{ dBZ}$) and 48 km^2 ($\tau = 37 \text{ dBZ}$). Converted to equicircle diameters, their size is 18 km, 13 km, 10 km and 8 km, respectively. This is well in line with the values of the average size of a rain area (A_r) and the mean number of peaks per rain area (n_r). As $A_r \cdot n_r / n_p = A_{max}$, the average area per reflectivity peak can also be calculated from the other two parameters. E.g., if the average rain area has a size of 230 km^2 and there are 1.7 peaks per rain area, the mean area per peak must consequently be $230 \text{ km}^2 / 1.7 = 135 \text{ km}^2$, approximately.

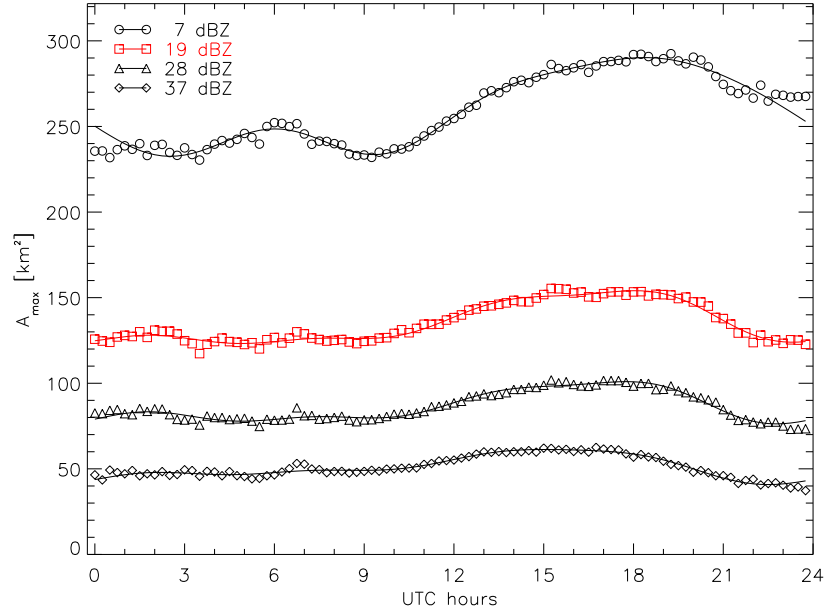


Figure 3.15: Diurnal variation of the average area per peak A_{max} for four different cut-offs. The solid lines represent the corresponding data assembled from the first four frequencies of their Fourier transform. A detailed list of the relevant parameters is given in Appendix B.

3.2.4 Rain Area Size Distribution

In the preceding section, the average size of the rain areas, the convection cells and their diurnal behavior was investigated. All that was done for the bulk data, not distinguishing between rain areas with the same peak number. In this section, the area of the rain areas will be analyzed for each peak number p separately to calculate the rain area size distribution (RASD). The equicircle diameter D_i of the rain areas is used instead of A_i , to be able to compare the results presented here with those from other studies (see section 1.4). Again, the data presented here are for a cut-off of $\tau = 19$ dBZ.

The size distribution $P_p(D)$ for the equicircle diameters and various values of p is displayed in Figure 3.16. Each of the distributions has a distinct maximum and overlaps neighboring distributions. As expected, rain areas with $p = 1$ have the lowest average size. The average size then increases with increasing p . This is also the case for the other cut-offs. Tests reveal that each of the distributions can very well be fitted by a log-normal function (Equation 2.15) as reported by MESNARD and SAUVAGEOT (2003). These functions are also shown in Figure 3.16. The quality of the fit is best for small p and deteriorates towards large peak numbers. Again, this is a consequence of the limited number of data available for rain areas with a large peak number.

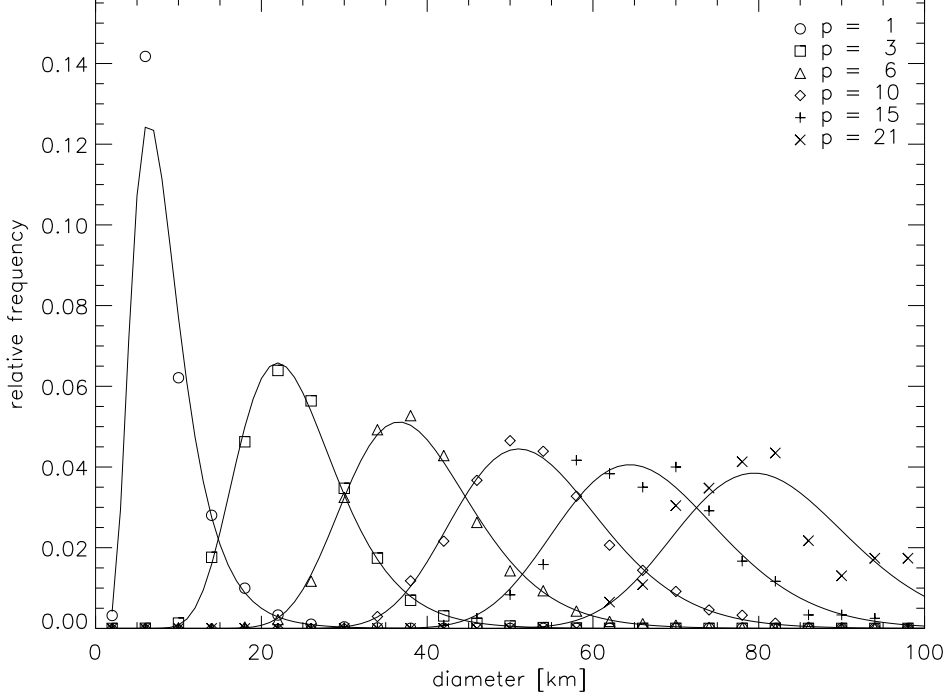


Figure 3.16: Size distribution $P_p(D)$ of the equicircle diameters for six values of p and $\tau = 19$ dBZ. The solid lines represent the corresponding fitted log-normal functions. The distributions were normalized for each peak number.

The parameters of the log-normal functions were computed (as described in Section 2.3.1, Equation 2.16 and 3.4) up to $p = 100$.

The parameters μ_p and σ_p for $\tau = 19$ dBZ are plotted as functions of p in Figures 3.17 and 3.18 (data of the other thresholds are available in Appendix D). It is found that σ_p can be fitted by a power law:

$$\sigma_p = c_1 \cdot p^{d_1}. \quad (3.4)$$

The quality of the fit is very good as the high correlation of $r > 0.96$ proves (Table 3.3). This is less clear for μ_p . The data points are not situated on a straight line as would be expected for a simple power law. Only for $p > 30$, a power law can be assumed. Thorough inspection of the power law for $p > 30$ and the deviations of the observed data for $p \rightarrow 1$ reveals that these deviations can very well be reproduced by another power law, yielding a product of two power laws for the whole data set. It is of the following form:

$$\mu_p = c_2 \cdot p^{d_2} (1 - c_3 \cdot p^{d_3}). \quad (3.5)$$

The fit to the data using Equation 3.5 gives very good results ($R > 0.99$) over the whole range of p . The calculated parameters are all given in Table 3.4. The whole procedure can also be undertaken for the area of the rain areas, instead of the equicircle diameter. Not surprisingly, the results obtained for $P_p(A)$ are basically the same, as the equicircle diameter is a simple transformation of the rain areas' area itself (Equation 2.3). The relevant figures, data and parameters are all given in Appendix D.

Equations 3.4 and 3.5 can now be plugged into Equation 2.15 to finally obtain $P_p(D)$:

$$P_p(D) = \frac{1}{D \cdot c_1 \cdot p^{d_1} \sqrt{2\pi}} \exp \left[-\frac{(\ln D - c_2 \cdot p^{d_2} (1 - c_3 \cdot p^{d_3}))^2}{2c_1^2 \cdot p^{2d_1}} \right]. \quad (3.6)$$

The results presented here are very well in line with those of MESNARD and SAUVAGEOT (2003). The parameters for σ_p reported by these authors deviate only slightly from the ones listed in Table 3.3 as different cut-offs are used here. However, there are also marked differences. MESNARD and SAUVAGEOT (2003) found a simple power law to represent μ_p . Here, a combination of two power laws fits the data as shown above. This discrepancy is most likely due to the fact that the aforementioned authors could only use peak numbers up to about $p = 20$, resulting from the much smaller area accessible by a single radar compared to a network of radars, as used here. A close inspection of the figures presented in the paper by MESNARD and SAUVAGEOT (2003) reveals, however, that a combination of power laws would have been more appropriate to use in there case, too.

Like for the PND, physical causes for the occurrence of the log-normal frequency distributions observed here are difficult to find. Generally, log-normal functions are frequently found to describe the frequency distributions of parameters related to precipitation. The log-normal function describes the size distribution of tropospheric clouds and their nearest neighbor spacing (MAPES and HOUZE 1993; LOPEZ 1977; HOUZE and CHENG 1977; ALI 1998; JOSEPH and CAHALAN 1990; SENGUPTA *et al.* 1990) as well as the amount of rainfall (BIONDINI 1976). This also applies to the area, volume and height of thunderstorms (POTTS *et al.* 2000). RAYMOND (2000) and RAYMOND (1997) show analytically that differential equations for relative humidity can yield solutions with log-normal distributions as well, providing a possible explanation why this type of distribution is so often observed in cloud and rain statistics.

LOPEZ (1977) also gives some examples when log-normal distributions occur. They are observed in systems that grow by the *law of proportional effects*. It applies to variates whose change at any step of a process is a random proportion of the previous value of the variate. Under the assumption that the change at each step is small, one can obtain an equation the central-limit

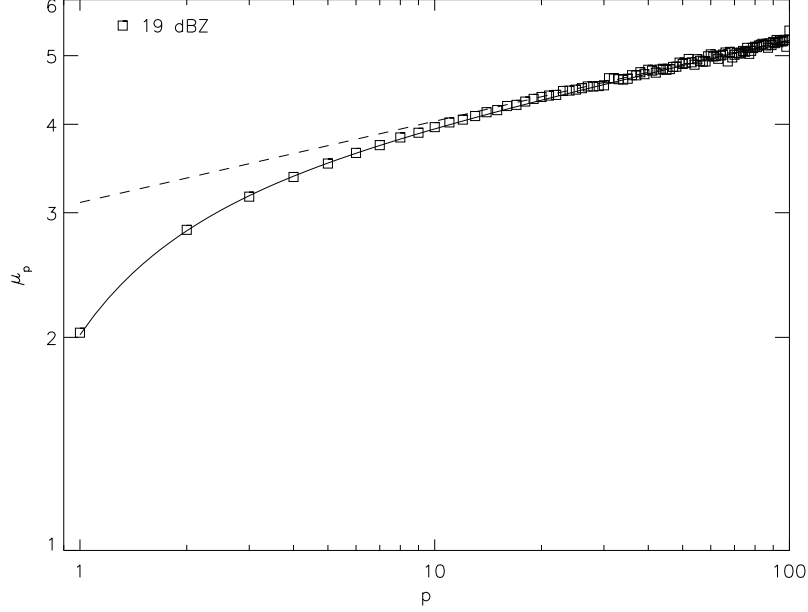


Figure 3.17: Parameter μ_p as a function of peak number p for $\tau = 19$ dBZ. The dashed line shows the power law fit for $p > 30$, the solid line represents the fitted data of Equation 3.5.

theorem can be applied to. It says that a variate $\ln x$ that is influenced by many small and unrelated random effects is in the limit normally distributed and, therefore, x is log-normally distributed (LOPEZ 1977). Therefore, if one assumes that the rain areas grow by the law of proportional effects, a log-normal size distribution can be expected. But, only if the change in size is small from step to step. That is just what is observed. Log-normal behaviour was detected for each single peak number, but not for the whole population. Because as soon as two rain areas merge, their peak numbers change. The change in size at this step is not small as is demanded by the law of proportional effects, at least not for the smaller of the two rain areas. Therefore, the rain areas investigated here are consistent with such a growth model.

Equation 2.18 provides a direct link between the parameters μ_p and σ_p of the log-normal function and the mean values of the considered variables area and equicircle diameter of the rain areas, respectively. As μ_p and σ_p can both be expressed by power laws, it is possible to calculate the mean diameter \bar{D}_p and the mean area \bar{A}_p of a rain area for a given value of p . Substituting μ_p and σ_p in Equation 2.18 yields:

$$\bar{x}_p = \exp \left(c_2 \cdot p^{d_2} (1 - c_3 \cdot p^{d_3}) + \frac{c_1^2}{2} p^{2d_1} \right), \quad (3.7)$$

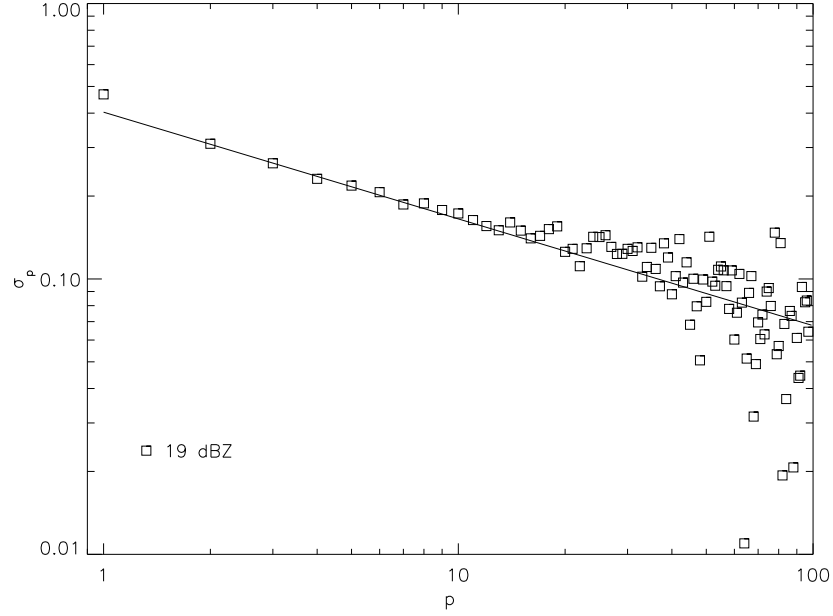


Figure 3.18: Parameter σ_p as a function of peak number p for $\tau = 19$ dBZ. The solid line shows the power law fit.

Table 3.3: Coefficients of Equation 3.4 for the various thresholds. Data of $2 \leq p \leq 7$ were used for the fit.

τ [dBZ]	c_1	d_1	r
7	0.42	-0.40	0.99
19	0.40	-0.39	1.00
28	0.39	-0.40	1.00
37	0.33	-0.36	0.96

Table 3.4: Coefficients of Equation 3.5 for the various thresholds. Due to the limited number of data no fit for $\tau = 37$ dBZ was possible.

τ [dBZ]	c_2	c_3	d_2	d_3	r
7	3.31	0.30	0.10	-0.93	1.00
19	3.10	0.35	0.11	-1.15	1.00
28	2.98	0.34	0.13	-1.20	1.00
37	-	-	-	-	-

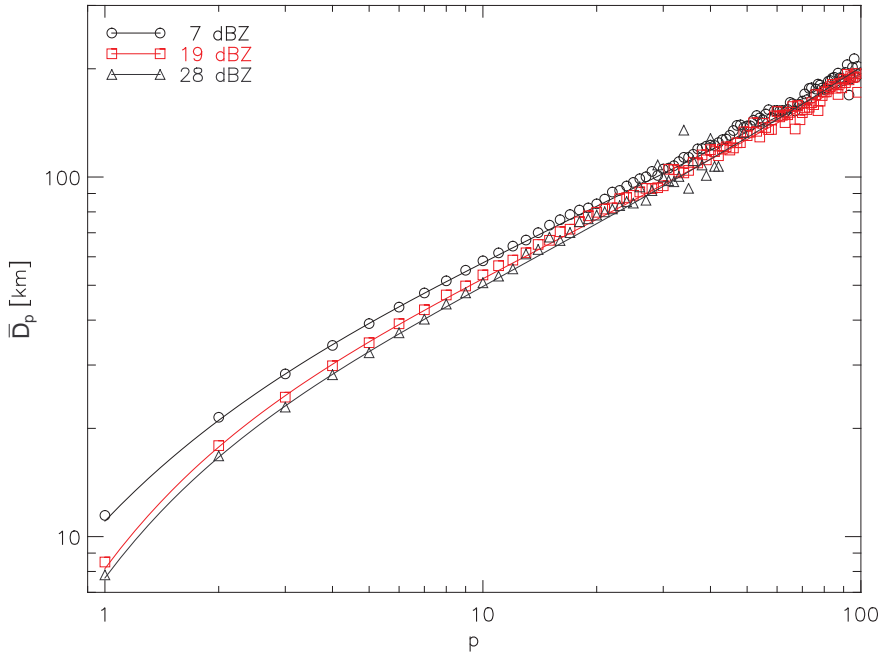


Figure 3.19: Mean diameter \bar{D}_p of the rain areas as a function of p and for three different thresholds. The lines show the corresponding computed data, using Equation 3.7.

where \bar{x}_p can be either \bar{D}_p or \bar{A}_p with their corresponding parameters c_n and d_n ($n = 1, 2, 3$; cf. Tables 3.3 and 3.4 and Appendix D). The computed mean diameter of the rain areas can, therefore, be compared to the one obtained from the data directly. The values deduced from Equation 3.7 match the observed ones very well (Figure 3.19), proving that the derived power laws for the parameters μ_p and σ_p are suitably chosen. The equivalent diameter of the rain areas quickly increases from about 10 km ($p = 1$) to more than 200 km for $p > 100$. The latter corresponds to an average area of each rain area of approximately 30 000 km² (the size of the German land North Rhine-Westphalia).

Also of interest is the average area associated with each peak. This parameter can be obtained simply by dividing Equation 3.7 by the peak number p . The result using the computed data and the corresponding observations are presented in Figure 3.20. Two features of the observed data are immediately apparent: Firstly, the average area associated with a peak strongly increases between $p = 1$ and approximately $p = 10$. Secondly, above $p = 10$, the increase in size is almost absent. \bar{A}_p/p changes from approximately 230 to 280 km² between $p = 10$ and $p = 100$. The computed data match the observations to a large extent, even though there are some discrepancies for peak numbers of about 20. A very similar behaviour is also observed for the other cut-offs (see Figure 3.20).

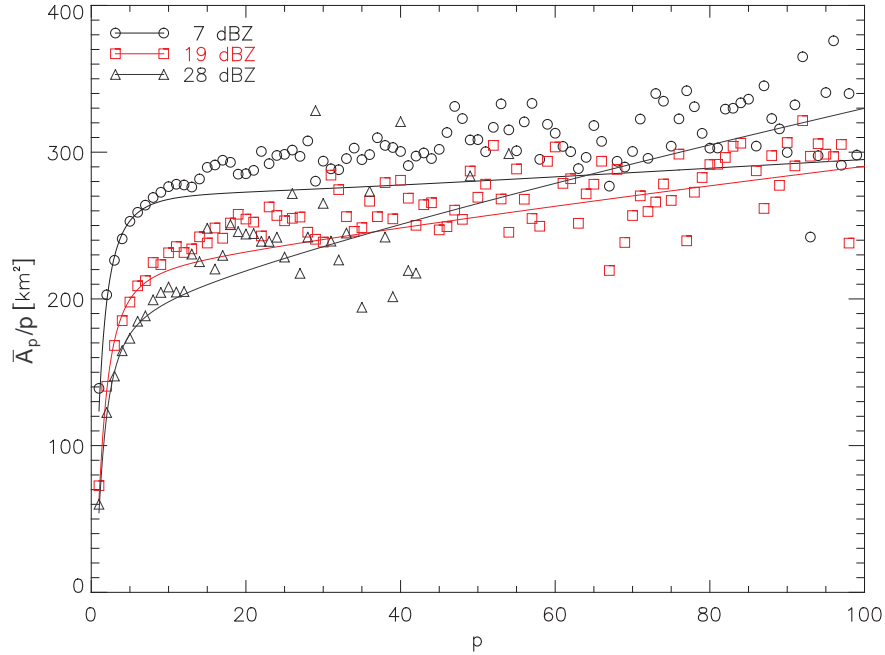


Figure 3.20: Mean area associated with each peak as a function of p . The lines show the corresponding computed data, using Equation 3.7.

3.2.5 Rain Area Size Distribution Without Peak Number Distinction

The parameters acquired for the PND and RASD can be used to calculate the RASD independent of the peak number. The frequency $P(p, x)$ of a rain area with p peaks and area A or diameter D within the whole population is given by the RASD $P_p(x)$ weighted with the frequency distribution $P(p)$:

$$P(p, x) = P_p(x) \cdot P(p), \quad (3.8)$$

where x can be substituted by either A or D . The intended rain area size distribution $P(x)$ is then obtained by summing over all values of p :

$$P(x) = \sum_{p=1}^{p_{max}} P_p(x) \cdot P(p). \quad (3.9)$$

Inserting Equations 3.4, 2.15, 3.5 and 3.1 finally yields size distributions $P(A)$ and $P(D)$:

$$P(A) = \frac{c_0}{Ac_1\sqrt{2\pi}} \sum_{p=1}^{p_{max}} p^{d_0-d_1} \exp \left[-\frac{(\ln A - c_2 p^{d_2} (1 - c_3 p^{d_3}))^2}{2c_1^2 p^{2d_1}} \right] \quad (3.10)$$

and

$$P(D) = \frac{c_0}{Dc_1\sqrt{2\pi}} \sum_{p=1}^{p_{max}} p^{d_0-d_1} \exp \left[-\frac{(\ln D - c_2 p^{d_2} (1 - c_3 p^{d_3}))^2}{2c_1^2 p^{2d_1}} \right]. \quad (3.11)$$

Now, the so determined distributions can be compared with the direct determined ones using the original data sets. Figure 3.21 visualizes the results for the area of the rain areas (Equation 3.10; $\tau = 19$ dBZ). Both data sets agree very well. There are only slight deviations in the range between 100 km^2 and 500 km^2 . These deviations can be traced back to the mismatch of parameter σ_p for $p = 1$ (cf. Figure 3.18). The fit delivers a σ_p that is smaller than observed leading to a frequency distribution of the single cells that is narrower than the observed one. This results in a too small number of large rain areas with one peak. As a consequence, there are too few rain areas in the size range stated above. The increasing mismatch above approximately 4000 km^2 is, once again, due to the low numbers of rain areas available in that range of sizes. The properties of the distributions for other cut-offs closely resemble those presented here (Figure D.5 in Appendix D). That also applies to the distribution of diameters (cf. Figure D.6 in Appendix D).

Equation 3.10 can also be used to analyze which population of the rain areas dominates a certain size range by summing over selected values of p only, instead of all p . The result is displayed in Figure 3.22. It is found that most of the rain areas below about 200 km^2 are single peaked. This limit is slightly shifted for other cut-offs. Large rain areas with areas $A > 10^4 \text{ km}^2$ usually have a peak number larger than 32. The match between observed and calculated data is very good. Though, there is some discrepancy for the transition between $p = 1$ and $2 \leq p < 4$. An explanation for this is easily found in the mismatch between the observed σ_p for $p = 1$ and the one modeled using Equation 3.4 (cf. Figure 3.18) as already explained above.

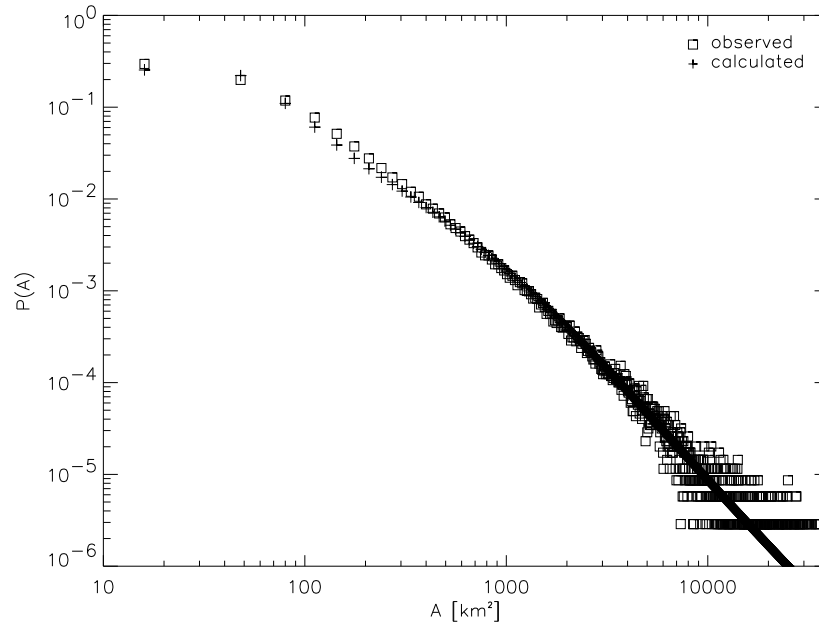


Figure 3.21: Rain area size distribution for $\tau = 19$ dBZ. Crosses denote calculated data, while the observed data are shown by squares (bin size: 32 km^2).

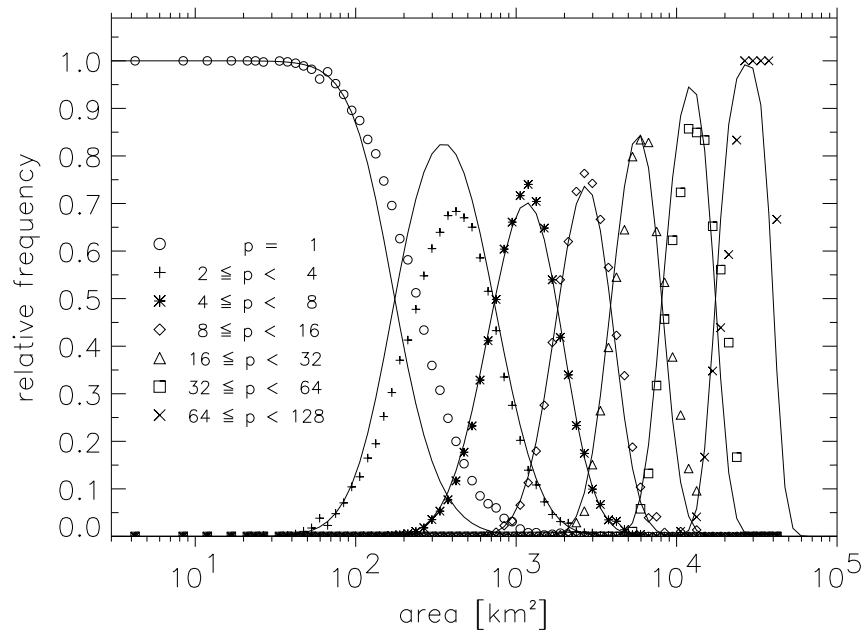


Figure 3.22: Distribution of the frequency of various rain area populations $\tau = 19$ dBZ. The lines show the corresponding modeled data.

3.3 Distances Between Peaks

In the previous sections parameters related to the size of the rain areas and the number of convection cells were analyzed. Now, the distances e_{ij} between the cell centers within a rain area are investigated. They provide valuable information on where convection cells emerge in relation to already present ones and if, e.g., there are differences between large clusters and smaller ones. It could be hypothesized that larger clusters can enhance the development of secondary convection more efficiently through stronger or more numerous cold air outflows.

ALI (1998), SENGUPTA *et al.* (1990), JOSEPH and CAHALAN (1990) report that the nearest neighbor spacing of cumulus clouds follows a log-normal distribution. It is therefore tested whether or not this type of distribution governs the distances between centers of the radar observed convection cells as well.

To prove or disprove the hypothesis formulated above and to analyze the frequency distribution of the spacings between the cells, the nearest neighbor distribution (NND) was computed (see Section 2.3.1). It includes the distances between the peaks and their nearest neighbor. The distribution was computed for each peak number separately. Naturally, this can only be performed for rain areas with $p \geq 2$.

3.3.1 Nearest Neighbor Distribution - Peak Number Dependence

Each peak in a cluster with $p \geq 2$ has a nearest neighbor and can be assigned a distance to that neighbor (see Figure 3.23). All these distances were used to compute the NND. The whole process was undertaken for each peak number separately. The resulting distributions $P_{NN}(\mathbb{E})$ of distances e_{ij} for four selected peak numbers are presented in Figure 3.24. Surprisingly, there are no large differences between the NNDs for $p = 2, 5, 10$ and 50 . Each distribution is marked by a steep increase towards a distinct maximum close to a distance of 10 km. The distributions then drop off more gradually towards larger distances. It is also apparent that nearest neighbor spacings above 30 km are very rare.

These distributions can again be fitted very well by log-normal functions, as Figure 3.24 implies. It is confirmed that the NND does not vary greatly despite the very different peak numbers by calculating the parameters μ_p and σ_p for each of the log-normal fitting functions. The parameter μ_p is indeed more or less constant over the whole range of peaks (Figure 3.25), implying that the mean value of the distribution does not change with respect to p :

$$\mu_p = \text{const} = c_5. \quad (3.12)$$

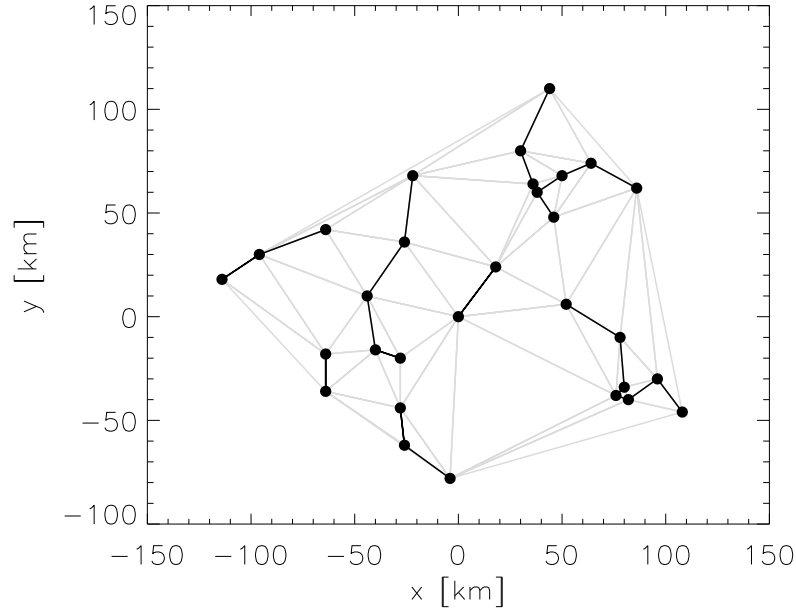


Figure 3.23: A rain area with $p = 30$. The connecting lines between the cell centers (black dots) represent the sides of the triangles resulting from the Delaunay triangulation. The thick black lines denote the connections between a peak and its nearest neighbor. They constitute the NND.

σ_p on the other hand shows a different behaviour as it slightly decreases with increasing peak number. It is found that it can quite well be fitted by a function of the following form (cf. Figure 3.26):

$$\sigma_p = c_4 - d_4 \log p, \quad (3.13)$$

A decreasing σ_p with increasing peak number has the effect that the NND of a cluster with a high peak number is narrower than that of cluster with low p . That means that small nearest neighbor spacings are more frequent in the first case than in the latter. This is consistent with the hypothesis formulated above. It is also confirmed that a log-normal distribution governs the frequency distribution of \mathbb{E} as observed by authors listed above for cumulus clouds, even though the scales of the investigations are very different. That a log-normal distribution is found here as well is likely due to the fact that small cumulus clouds and deep convective clouds originate from the same basic processes. However, all these authors do not give physical reasons for the occurrence of the log-normal distribution. Probably, the processes described in Section 3.2.4 give at least some possible explanations.

The parameters μ_p and σ_p for the various cut-offs are all listed in Table 3.5. The results are about the same for the other cut-offs. Again, it was not

Table 3.5: Coefficients of Equation 3.12 and 3.13 for the various thresholds. The maximum peak number (p_{max}) used for the fit is given as well. Due to the limited number of data, no fit for $\tau = 37$ dBZ was possible.

τ [dBZ]	p_{max}	c_4	d_4	R	c_5
7	50	0.44	-0.036	0.83	2.44
19	50	0.42	-0.033	0.65	2.44
28	20	0.41	-0.025	0.46	2.41
37	-	-	-	-	-

possible to compute parameters for $\tau = 37$ dBZ as only data up to about $p = 15$ were forthcoming.

Above, NNDs were analyzed for each peak number separately. The whole process can also be undertaken without distinguishing between rain areas with different peak numbers. This results in a NND for the whole rain field instead of a NND of a certain rain area type. This distribution is also displayed in Figure 3.24. Not surprisingly this distribution is very similar to the NNDs of certain peak numbers. This is because it basically is the sum of all the peak numbers' NNDs. The parameters μ_p in this case is 2.409 and $\sigma_p = 0.385$. These values are very close to the ones found for the NNDs described above.

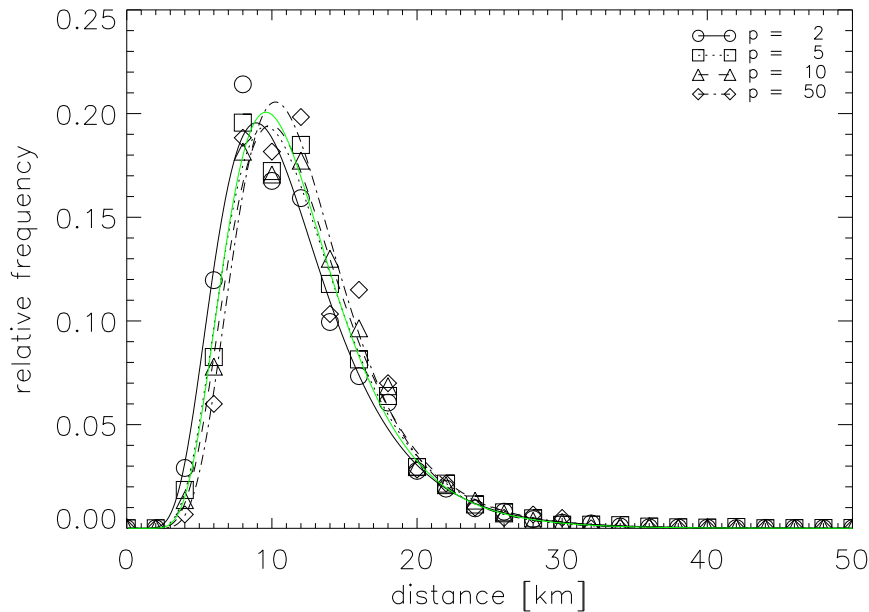


Figure 3.24: NND for four different peak numbers (gray, $\tau = 19$ dBZ) and independent of p (green). The lines show the corresponding fitted log-normal functions.

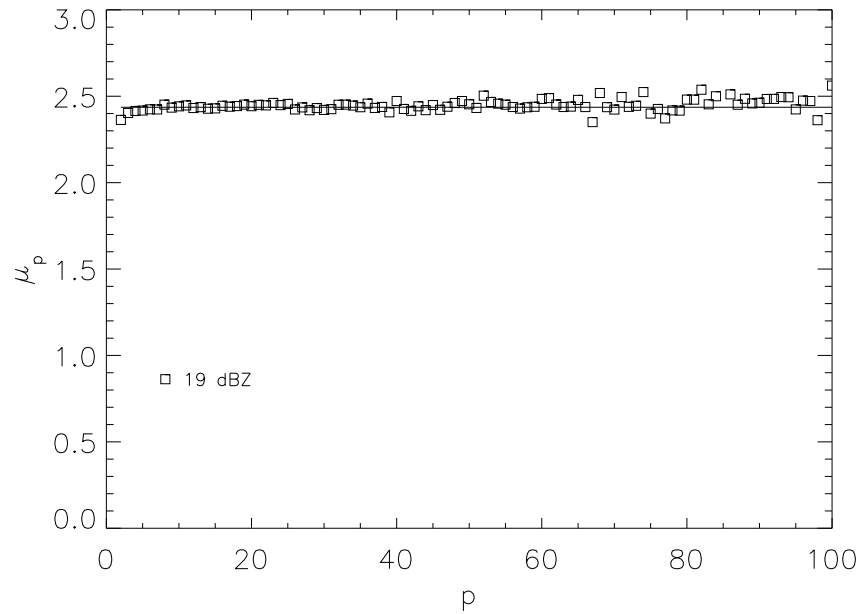


Figure 3.25: Parameter μ_p for the NND as a function of peak number ($\tau = 19$ dBZ). The line shows the average value of μ_p .

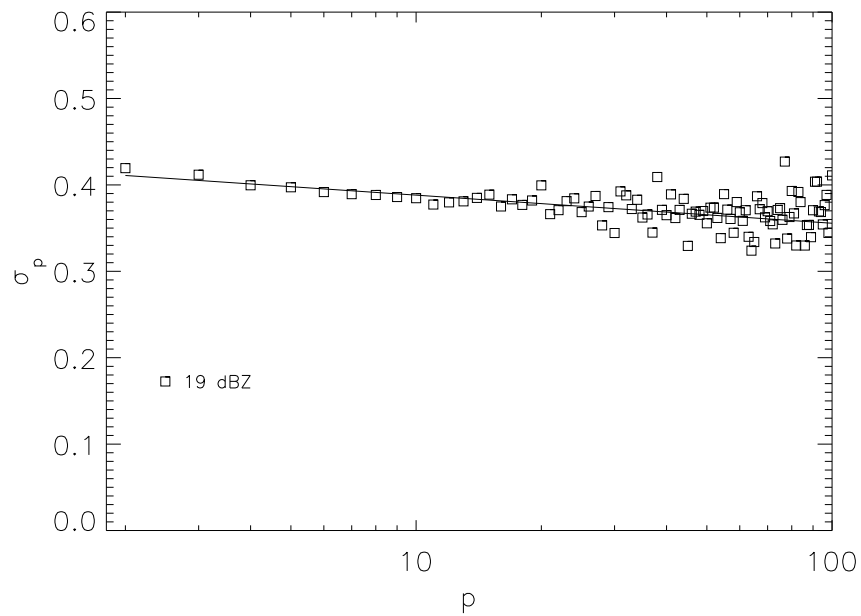


Figure 3.26: Parameter σ_p for the NND as a function of peak number ($\tau = 19$ dBZ). The line shows the corresponding fitted function (Equation 3.13).

3.3.2 Nearest Neighbor Distribution - Diurnal Variation

The NNDs were also analyzed with respect to their diurnal variation. The NND independent of peak number (see previous paragraph) was chosen representatively to display the results which are almost identical for the other peak numbers (as in the previous section). The NND was calculated for hourly periods, i.e. it includes data from the radar images of 0, 15, 30 and 45 minutes past each hour. The resulting 24 distributions are displayed in Figure 3.27. It is apparent that the distribution does not change much. The location of the maximum is close to 10 km and the difference in height of the maximum is only 0.025. For each of the distributions μ_p and σ_p were derived and plotted in Figures 3.28 and 3.29. The variation of μ_p which determines the location of the maximum of the distribution is minimal and translates to a variation of ± 400 m compared to a spatial resolution of the radar images of 2 km. Parameter σ_p diverges a bit more from the mean value, but this deviation is still small. The average values of the parameters are $\mu_p = 2.40$ and $\sigma_p = 0.387$.

That the NND does not vary over a day implies that the overall structure of the rain field and the rain areas does not change. Interestingly, it was observed (Section 3.2.3) that the average area per peak is larger in the after-

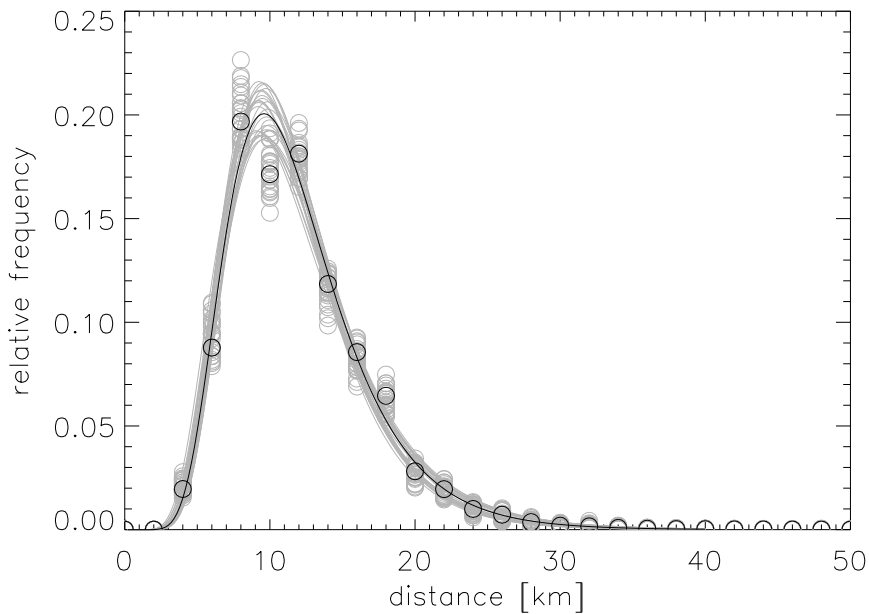


Figure 3.27: NNDs independent of p ($\tau = 19$ dBZ) for 24 hourly periods (gray) and the NND for the combined data (black). The lines show the corresponding fitted log-normal functions.

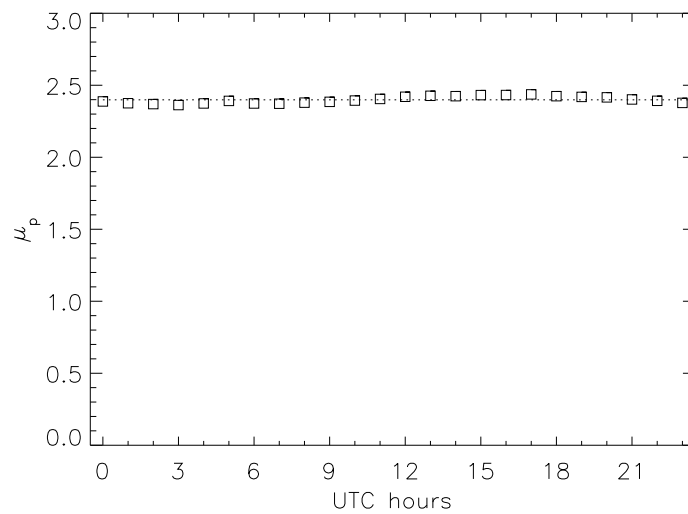


Figure 3.28: Parameter μ_p for the hourly NNDs (independent of p , $\tau = 19$ dBZ). The dotted line shows the average value of μ_p .

noon. This does obviously not coincide with an increase in distance between the convection cells and reinforces the assumption that a larger fraction in the afternoon of decaying convection cells is responsible.

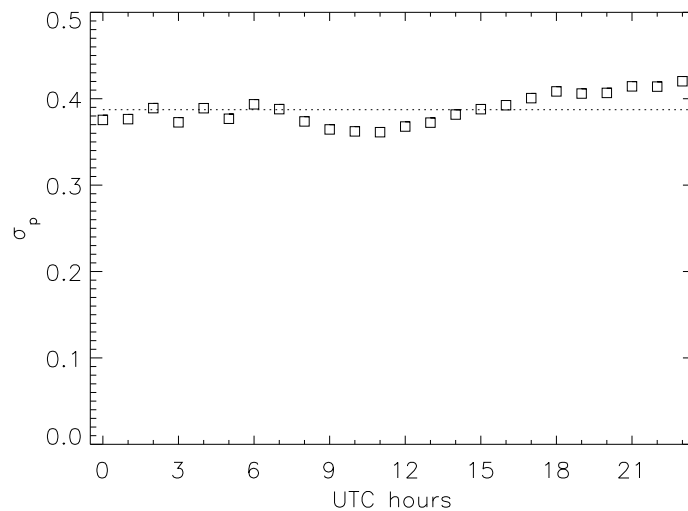


Figure 3.29: Parameter μ_p for the hourly NNDs (independent of p , $\tau = 19$ dBZ). The dotted line shows the average value of σ_p .

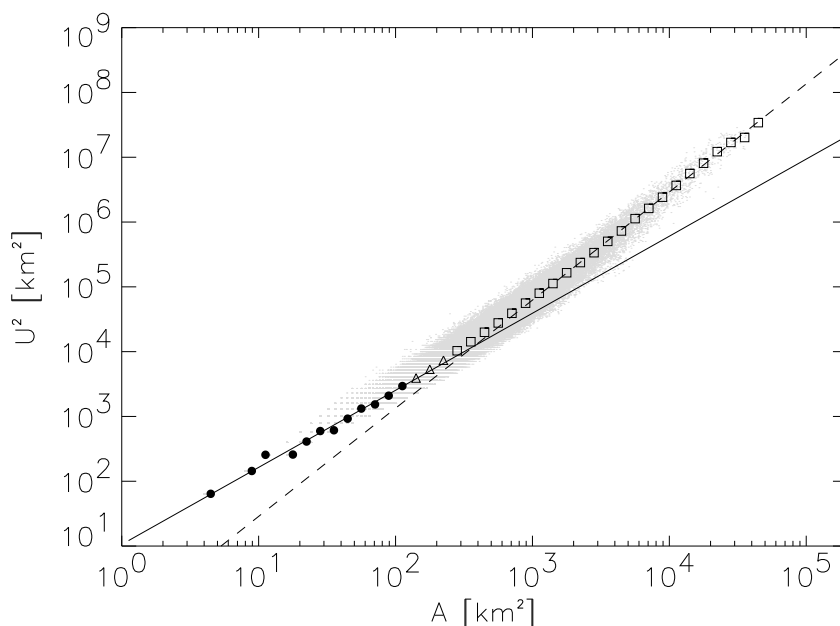


Figure 3.30: U^2 plotted over area A . The symbols represent the average values for certain size classes. The type of symbol indicates the fraction of unicellular rain areas within that size class (black circles: $>80\%$; triangles: 50% to 80% ; squares $<50\%$). The solid line shows the regression line for a fractal dimension of $d = 1.19$ and the dashed line $d = 1.67$.

3.4 Fractal Dimension

As already described in section 1.4, the fractal dimension provides information on how contorted the perimeter of a structure is compared to its area (the so-called area-perimeter relation or A-P relation). According to LOVEJOY (1982), the fractal dimension is also useful to distinguish between a "small scale" (size $< \lambda$) and a "large scale" (size $> \lambda$), if different values for the A-P relation are observed for area $< \lambda^2$ and area $> \lambda^2$. In the literature, many different values of the fractal dimension of radar and satellite observed rain and cloud fields are reported (see section 1.4). It is the purpose of this section to determine the fractal dimension of the rain areas analyzed in this thesis, to be able to compare it to the values reported by other scientists. Also, the existence of different scales is checked for.

From the perimeter U and the area A of the rain areas, their fractal dimension d can be deduced (cf. Chapter 1.4). U and A were computed for each rain area, as described in Chapter 2.3, and plotted as U^2 over A in Figure 3.30 for a cut-off of 19 dBZ. Obviously, the data points are not randomly distributed, but are fairly well aligned along a line with a slope of 1.35 in the double-log plot. This slope corresponds to the fractal dimension

of the rain areas (see section 1.4). Another feature is immediately evident as well: The fractal dimension is not constant over the whole range of sizes. Below approximately $A = 300 \text{ km}^2$ the slope is lower than for areas larger than this threshold. Such behaviour is also observed for the other cut-offs. To aid comparability, the average values for certain size classes of rain areas are shown as well. It is found that the fractal dimension is $d = 1.19$ for small rain areas up to a size of about 100 km^2 and increases to $d = 1.67$ for $A > 1000 \text{ km}^2$ ($d = 1.75$ for $\tau = 7 \text{ dBZ}$ and $d = 1.55$ for $\tau = 28 \text{ dBZ}$ and $\tau = 37 \text{ dBZ}$). The break diameter is found to be approximately $D_b = 20 \text{ km}$ ($A = 300 \text{ km}^2$, see above).

The type of the symbols used for the representation of the average values of the size classes indicates the fraction of unicellular rain areas in that range of sizes. It can clearly be seen that the change in fractal dimension between $A = 100 \text{ km}^2$ and $A = 1000 \text{ km}^2$ goes along with a decreasing fraction of rain areas with $p = 1$. This can even more clearly be identified in Figure 3.22.

It was stated above that such a change in fractal dimension is directly related to the existence of "small scale" and "large scale" structures. In this case the analysis clearly shows that the two different fractal dimensions found are closely linked with unicellular and multicellular rain areas (see above). Therefore, the single cells can be considered to be the building blocks of the "large scale" clusters. The lower fractal dimension of the single cells also means a less contorted perimeter, which indicates that the single cells are rounder than the multicellular clusters.

All these results are consistent with those obtained by BENNER and CURRY (1998) who found fractal dimensions of $1.08 < d < 1.29$ for small clouds fractal dimensions of $1.27 < d < 1.73$ for larger clouds. These authors as well as CAHALAN and JOSEPH (1989), SENGUPTA *et al.* (1990), KUO *et al.* (1993) and BENNER and CURRY (1998) attribute the difference in fractal dimension to unicellular (small d) and multicellular (large d) systems. This is confirmed here for radar observed clouds (see above). MESNARD and SAUVAGEOT (2003) also find larger fractal dimensions for multi-peaked rain areas compared to their single-peaked counterparts. Why clouds and rain areas have an average fractal dimension of $d = 1.35$ is not known so far.

Chapter 4

Conclusions, Limitations and Outlook

4.1 Conclusions

This phenomenological study of radar observed post-frontal deep convective cloud fields was performed using radar composite images provided by the DWD. They enabled to investigate rain fields over scales so far not covered by other studies. It provides new insight into some of the phenomena studied in the past, confirms results obtained by other researchers and also improves these results.

Many of the aspects observed during the investigation of the structure of the post frontal convective rain fields are well known phenomena and can mainly be explained by the change of insolation during the day. These are e.g. the diurnal cycles of the numbers of rain areas and their total size, as well as the number of rain areas, respectively deep convection cells, as was initially hypothesized. The maxima of all these diurnal cycles were found to occur in the early afternoon, about two hours before the occurrence of the maximum surface heating. It is reported by other studies that the timing of the maximum of convective activity over land is mainly influenced by surface heating, but can be strongly modified by many other factors important for the initiation of deep convection (see Sections 1.1, 3.1.1 and 3.2.1). These factors might probably explain the observed time difference. The dominating effect of surface heating is further reinforced by the fact that the timing of the cold front passage has no preferred time of day. It could be expected that the maximum occurrence of deep convective cells and their maximum extent is found some time after the passage of such a front (related to a following trough, for example) which is clearly not the case here.

The diurnal cycle of the average area per peak/rain area showed that a not well pronounced maximum occurred in the late afternoon, during the

time of day when peak numbers and rain area numbers decline the strongest. The observed maximum is likely a consequence of the life cycles of the deep convection cells. They begin as small objects, but end as large extended objects (see Sections 1.1 and 3.2.2).

It was discovered, for the first time, that the average number of deep convection cells is near constant over the day. This characteristic is a direct consequence of the self similar frequency distribution of the population of rain areas, the power law (see Section 3.1.3).

As shown in Section 3.1.2 the maximum numbers of peaks varied between only 29 and more than 400 on the 39 investigated days. It was not purpose of this study to investigate the causes for these large differences. However, in the introduction it was outlined that a whole range of factors influence the triggering of convection, like density stratification, large scale lifting, orography, temperature and moisture variations at the surface, roughness length changes between ocean and land, as well as local circulation systems. The combination of all these factors and their complex interaction determine where, when and how many deep convective systems emerge. To investigate which of these factors or combination of factors has the largest effect remains to be analyzed by future phenomenological studies (as is currently done in the frame of a Diploma thesis at the Institute of Meteorology and Climatology of the Leibniz University of Hannover) or through modeling.

Despite the large day-to-day differences in total numbers of rain areas, the population of rain areas, with respect of their peak number p , always shows scale-free behaviour, ie. it is self-similar. The values of the exponent of these power laws are well within the range observed by other researchers (eg. MESNARD and SAUVAGEOT 2003, see Section 1.4). It does not matter whether hourly, daily or seasonal data are considered, power laws are found to represent the frequency distribution of peak numbers (the PND) very well (Sections 3.1.2, 3.1.3 and 3.1.4). The physical causes for this behaviour are not known. Such an investigation is beyond the scope of this thesis.

However, it was possible to extend the investigated range by about one order of magnitude compared to other studies. Also, it was shown for the first time that the PND is a power law down to temporal scales of hours. Interestingly, it was discovered that the average PND does not vary over a large area and is the same at the coast as well as at the Alps despite the very different orographical features and surface inhomogeneities (like land use, vegetation etc.). The effect that these features have on the type population seems to be homogeneous for the whole investigated domain. If absolute numbers of rain areas are considered, there is a clear effect of the coast (see Section 3.1.4). There, convective activity obviously gets enhanced as could be expected from processes like roughness length changes and sea-breeze effects (cf. Section 1.1).

To find the physical causes for the occurrence of the scale free distribution of the peak numbers was beyond the scope of this study. However, it is

reported that extended dissipative dynamical systems (like Rayleigh-Bénard convection, see Section 1.4 and 3.1.2) exhibit such behaviour if they are an SOC system. The temporal fingerprint of such a system, $1/f$ -noise, was looked for, but not detected, however. It is recommended to further investigate the possible presence of $1/f$ -noise in future studies to find out whether or not post-frontal convection is an SOC system.

Besides power laws, log-normal functions also turned out to describe very well some aspects of the population of rain areas. That applies to the area distributions of rain areas with a certain peak number (RASD, Section 3.2.4) and also to the distances between the peaks (NND, Sections 3.3.1).

In the past, only one publication by MESNARD and SAUVAGEOT (2003) describes an investigation on rain areas with peak number dependence. Their results (see Section 1.4) are partially confirmed here. They, too, found log-normal functions to be suitable to describe the RASD. Also, they discovered that the parameter σ_p , which is the standard deviation of the log-normal distribution can be described by a simple power law (cf. Section 3.2.4). However, due to the much smaller size of their investigated domains they were not able to compute the RASD for peak numbers higher than about $p = 20$. This range is extended here by about one order of magnitude. As a consequence, a slightly different function was found to be the best match for μ_p . Here, it is a combination of two power laws and not a simple power law. Again, it was beyond the scope of this thesis to attain physical causes for the occurrence of the log-normal distribution. Possible reasons for its origin are given in Section 3.2.4 (e.g. law of proportional effects).

The RASDs and the PND were used to assemble the RASD without peak number distinction, following the procedure described by MESNARD and SAUVAGEOT (2003). As the correlations for the fits to the parameters describing the RASDs and the PND were all in the range of above 0.9, it is not surprising that the final computed result matched the observations to a high degree, too (see Section 3.2.5).

It was also found that the area associated with a peak is smaller for low peak numbers than for the large ones (Section 3.2.4). A reason for that could be the growth of the single convection cells. A newly formed cell is naturally smaller than a cell at a more mature stage. For a growing cell it becomes more and more likely that it gets incorporated into a cluster of cells as its area grows. Though, for rain areas with $p > 10$ the average area per peak does not change much any longer. The likely explanation is that within such a cluster of convection cells cells of various age are present. Some of them are still growing, but, some are already decaying. It seems that some equilibrium state emerges where the average area per peak remains roughly constant within a cluster of cells. Proving this assumption is difficult as it would require to track each single deep convection cell within a cluster and to determine its size. This question is left to future research.

The fact that the area of a peak is roughly constant also means, as would be expected, that the more peaks a rain area has the larger it is. Therefore, the different types of rain areas dominate different scales of size (Section 3.2.5). Eg. 80% to 100% of the rain areas below approximately 200 km² ($\tau = 7$ dbZ) have $p = 1$, ie. they are single cells. These results helped to explain the detection of clearly different fractal dimensions for unicellular and multicellular rain areas.

The fractal dimension provides a measure on the "wigglyness" of the perimeter of the rain areas with respect of their area. It was shown (Section 3.4) that the fractal dimension of small rain areas is lower than that of large rain areas. Such a change in fractal dimension is a clear indication of the presence of two distinct populations (LOVEJOY 1982). It has been shown in the past (see Section 3.4 that these two populations are unicellular and multicellular clouds. In this case, the lower fractal dimensions can clearly be tracked down to the rain areas with $p = 1$ as they dominate just that range of sizes where the low value of D was detected. The high values of D are found in the size range where more than 80% of the rain areas consist of at least two convection cells, i.e. they are multicellular. This proves that the results found from satellite image analyses of clouds are valid for the radar observed rain areas as well. The values of the fractal dimensions for the different rain area sizes are well within the range reported by other scientists (cf. Section 1.4 and 3.4).

Distances between cumulus clouds were frequently analyzed in the past (see Sections 1.4 and 3.3). Here, for the first time, the distances between the centers of deep convection cells observed by radar are presented. Like the distances between the satellite observed clouds, the distances show a log-normal frequency distribution (see Section 3.3). The frequency distribution was also calculated for each peak number separately, with an almost identical log-normal function for all the peak numbers. This is in contrast to the RASD, where each peak number had a log-normal distribution that was markedly different from those of other peak numbers due to the increasing size of the rain areas with increasing peak number. The sum of log-normal functions with different standard deviations and means does not result in another log-normal function. Therefore, the frequency distribution of the RASD independent of p was not log-normal (cf. Section 3.2.5). In the case of (near) identical standard deviations and means, the sum of log-normal distributions yields another (near) log-normal distribution. This fact could explain why log-normal functions were found to represent the nearest neighbor distributions of clouds in earlier studies, even though the multicellular character of cloud clusters was not considered.

The diurnal variation of the distances between the convection cells was also analyzed (Section 3.3.2). Interestingly, it was discovered that the NND remains nearly constant during the day. This implies that the overall structure of the convective rain field does not change even though the average

area per convection cell was found to be larger in the afternoon. These observations reinforce the assumption that a larger fraction of decaying rain areas is the cause of the afternoon increase in rain area size. The day-to-day variations of the distance distribution still remains to be analyzed, however.

Finally, it can be stated that a small number of parameters is sufficient (for a given threshold value τ) to describe the basic characteristics of the post-frontal showers. For the size distributions eight parameters are necessary (see Equations 3.10 and 3.11) while only three suffice for the distances between the peaks (see Equations 3.12 and 3.12). The diurnal variations of the total rain area, the absolute numbers of convection cells and the other related parameters can very well be reproduced by the first four frequencies of the FFT.

4.2 Limitations

The study performed here had some limitations. Firstly, the radar composite images that were available consisted of a six-step reflectivity scale. It made the detection of reflectivity peaks more difficult compared to a "continuous" reflectivity distribution. The errors in the numbers of detected peaks were of the order of 10% as laid out in Section 2.3.1. It is therefore recommended to repeat the study using the PZ-Product of the DWD with a reflectivity resolution of 0.5 dBZ and a spatial resolution of 1 km. Then, the shape of the observed structures (like ellipticity) and the amount of precipitation could be taken into account as well. Partially, this is already done within a DFG project conducted at IMuK.

The manual segmentation of the radar images limited the number of convective situations that could be investigated. It would be desirable to develop an automated approach like the use of neural networks (see e.g. WALTHER and BENNARTZ 2006). Then, a much larger number of radar images could be analyzed and the statistical basis for high rain rates would get much improved.

As is the case for most phenomenological studies, it is difficult to determine the exact physical causes of the observed characteristics of the rain fields and rain areas. Nevertheless, many of the observed characteristics are in line with the effects that various physical processes have (presented in the Introduction). The complex interaction of processes involved in the initiation of deep convection makes it necessary, however, to use models to investigate these interactions further.

4.3 Summary and Outlook

This study investigated features so far not analyzed in previous studies, like PNDs down to a temporal scale of one hour and nearest neighbor distances of convection cells observed by radar. The use of radar composite images obtained by a network of radars allowed to extend the results of other studies by about one order of magnitude. Furthermore, it confirmed and clarified earlier results which were limited due to the use of single radars. Additionally, for the first time, the distances between the centers of deep convective cells observed by radar were analyzed for each rain area separately and the whole field of rain areas. These nearest neighbor distances were found to be log-normally distributed, as was already detected for clouds by studies of satellite images. All these statistics lay the basis for the development of a rain cell generator.

The results and methods of this project were used in the validation process of the regional climate model BALTIMOS. There, small scale precipitation patterns produced by the model were compared to the ones observed by radar (THEUSNER and HAUF 2004; THEUSNER and HAUF 2006). All these methods can be used in the validation process of future climate and weather models where the hydrological cycle is of crucial importance.

Even though this phenomenological study did not allow to find the physical causes of the observed structures, it very well lays and extends the basis to use models to analyze the processes that lead to the development of these observed structures. The results and methods presented here also supported the initiation and extension of a research project within the large scale research program Quantitative Precipitation Forecast (SPP 1167 PQP) of the DFG. It laid the basis for future research that tries to find connections between the observed PNDs (which were found to be power laws) and amount of precipitation to ultimately enhance the quality of quantitative precipitation forecasts.

Appendix A

Used radar images

Table A.1: List of the radar images from 1997 used for the analyses.

date	period(s)	number of images
1997/05/07	0:00 - 23:45	96
1997/05/09	5:30 - 23:45	74
1997/05/10	0:00 - 23:00	93
1997/05/21	0:00 - 23:45	96
1997/05/28	7:15 - 23:30	66
1997/05/30	0:00 - 17:15	70
1997/05/31	10:00 - 22:00	49
1997/06/09	8:45 - 20:30	48
1997/06/14	6:00 - 23:45	72
1997/06/22	7:15 - 23:45	67
1997/06/23	0:00 - 23:45	96
1997/06/24	7:00 - 23:45	68
1997/07/01	4:45 - 13:00; 13:45 - 23:45	75
1997/07/04	5:15 - 23:45	75
1997/07/05	8:00 - 23:45	64
1997/07/19	5:15 - 23:45	75
1997/07/27	1:45 - 23:45	89
1997/07/29	0:00 - 23:45	96
1997/08/01	7:30 - 23:45	66
1997/08/29	0:00 - 23:45	96

1531

Table A.2: List of the radar images from 1998 used for the analyses.

date	period(s)	number of images
1998/06/10	4:45 - 5:15; 5:45 - 10:15; 10:45 - 23:45	75
1998/06/11	0:00 - 3:15; 3:45 - 5:15; 5:45 - 23:45	94
1998/06/15	0:00 - 5:30; 6:00 - 6:30; 7:00 - 23:45	94
1998/06/16	0:00 - 10:15; 10:45 - 12:15; 12:45 - 13:30; 14:00 - 23:45	93
1998/06/17	0:00 - 9:45; 10:30 - 22:15	88
1998/06/18	2:45 - 22:15	79
1998/06/28	0:00 - 23:45	96
1998/07/01	0:00 - 23:30	95
1998/07/05	4:30 - 23:45	78
1998/07/06	0:00 - 23:45	96
1998/07/07	0:00 - 23:45	96
1998/07/14	0:00 - 4:30; 6:30 - 23:45	89
1998/07/15	0:00 - 5:45; 6:45 - 11:00; 11:30 - 23:45	92
1998/07/31	0:00 - 23:45	96
1998/08/05	0:00 - 21:00	85
1998/08/22	0:00 - 6:00; 6:30 - 23:45	95
1998/08/23	0:00 - 23:45	96
1998/08/27	0:00 - 12:15; 12:45 - 23:45	95
1998/08/29	0:00 - 9:15; 9:45 - 23:45	95

1727

Appendix B

Fast Fourier Transform Parameters

Table B.1: Coefficients of Equation 2.20 for various thresholds for the diurnal cycle of the number of rain areas.

τ [dBZ]	$a_0/2$	a_1	a_2	a_3	a_4	ϕ_1	ϕ_2	ϕ_3	ϕ_4	r
7	38.06	0.67	0.05	0.074	0.069	0.57	0.48	-0.93	1.52	1.0
19	92.90	0.75	0.13	0.060	0.075	0.49	0.56	-0.32	-1.43	1.0
28	75.12	0.85	0.21	0.089	0.065	0.43	0.61	-0.39	-1.32	1.0
37	36.42	1.02	0.34	0.104	0.049	0.45	0.75	-0.34	-1.13	1.0

Table B.2: Coefficients of Equation 2.20 for various thresholds for the diurnal cycle of the number of peaks.

τ [dBZ]	$a_0/2$	a_1	a_2	a_3	a_4	ϕ_1	ϕ_2	ϕ_3	ϕ_4	r
7	169.96	0.78	0.15	0.070	0.064	0.49	0.64	-0.27	-1.36	1.0
19	157.36	0.79	0.16	0.068	0.064	0.48	0.66	-0.27	-1.34	1.0
28	97.04	0.87	0.22	0.084	0.055	0.44	0.71	-0.37	-1.28	1.0
37	40.12	1.03	0.34	0.097	0.045	0.45	0.78	-0.29	-1.06	1.0

Table B.3: Coefficients of Equation 2.20 for various thresholds for the diurnal cycle of the number of peaks per rain area.

τ [dBZ]	$a_0/2$	a_1	a_2	a_3	a_4	ϕ_1	ϕ_2	ϕ_3	ϕ_4	r
7	4.16	0.138	0.051	0.038	0.016	0.12	0.96	0.96	-0.51	0.97
19	1.67	0.039	0.028	0.017	0.015	0.32	1.28	-1.05	-1.56	0.94
28	1.28	0.021	0.021	0.010	0.015	0.68	-1.28	1.51	1.52	0.90
37	1.09	0.020	0.013	0.005	0.009	0.06	-0.86	-0.04	1.05	0.84

Table B.4: Coefficients of Equation 2.20 for various thresholds for the diurnal cycle of the total area of rain areas ($a_0/2$ and a_n in km^2).

τ [dBZ]	$a_0/2$	a_1	a_2	a_3	a_4	ϕ_1	ϕ_2	ϕ_3	ϕ_4	r
7	43540.37	0.82	0.15	0.055	0.052	0.62	1.03	0.06	-1.20	1.0
19	21980.54	0.86	0.18	0.057	0.048	0.57	1.03	-0.19	-1.20	1.0
28	8718.80	0.94	0.26	0.060	0.038	0.53	1.05	-0.33	-1.01	1.0
37	2210.57	1.13	0.41	0.062	0.035	0.50	0.99	0.11	-0.69	1.0

Table B.5: Coefficients of Equation 2.20 for various thresholds for the diurnal cycle of the average area of a rain area ($a_0/2$ and a_n in km^2).

τ [dBZ]	$a_0/2$	a_1	a_2	a_3	a_4	ϕ_1	ϕ_2	ϕ_3	ϕ_4	r
7	1078.29	0.19	0.049	0.059	0.021	0.69	-1.56	1.20	-0.14	0.97
19	226.03	0.14	0.058	0.027	0.034	0.95	-1.23	-0.98	1.53	0.98
28	110.77	0.14	0.078	0.030	0.042	1.05	-1.02	1.57	1.40	0.97
37	55.82	0.17	0.094	0.023	0.034	0.56	-1.10	1.01	1.22	0.97

Table B.6: Coefficients of Equation 2.20 for various thresholds for the diurnal cycle of the average area per peak ($a_0/2$ and a_n in km^2).

τ [dBZ]	$a_0/2$	a_1	a_2	a_3	a_4	ϕ_1	ϕ_2	ϕ_3	ϕ_4	r
7	258.95	0.10	0.032	0.024	0.009	1.51	0.00	1.38	0.26	0.98
19	135.23	0.11	0.038	0.012	0.020	1.16	-0.77	-0.90	1.48	0.98
28	86.32	0.12	0.058	0.021	0.028	1.10	-0.92	-1.49	1.35	0.98
37	51.03	0.15	0.082	0.022	0.027	0.61	-1.12	1.30	1.28	0.97

Appendix C

PND Parameters

Table C.1: Parameters of the peak number distributions of single days (year 1997; $\tau = 19$ dBZ). The parameters listed are those of Equation 3.1. Additionally, the correlation coefficient (r), the maximum peak number used for the calculation of the parameters (p_m) and the maximum peak number that occurred on the respective day (p_{max}) are given as well.

date	c_0	d_0	r	p_m	p_{max}
1997/05/07	0.746	-2.900	-0.997	6	30
1997/05/09	0.645	-2.430	-0.995	7	49
1997/05/10	0.699	-2.539	-0.998	7	18
1997/05/21	0.663	-2.453	-0.997	7	109
1997/05/28	0.973	-3.366	-0.990	4	11
1997/05/30	0.781	-2.854	-0.998	5	14
1997/05/31	0.754	-3.036	-0.996	5	23
1997/06/09	0.724	-2.393	-0.986	8	26
1997/06/14	0.641	-2.550	-0.990	6	138
1997/06/22	0.650	-2.389	-0.996	7	34
1997/06/23	0.619	-2.445	-0.992	7	98
1997/06/24	0.818	-3.001	-0.997	5	17
1997/07/01	0.663	-2.430	-0.997	7	36
1997/07/04	0.611	-2.319	-0.991	7	35
1997/07/05	0.645	-2.370	-0.994	8	87
1997/07/19	0.583	-2.340	-0.992	8	95
1997/07/27	0.704	-2.475	-0.999	7	26
1997/07/29	0.705	-2.491	-0.997	6	36
1997/08/01	0.661	-2.471	-0.997	7	93
1997/08/29	0.690	-2.519	-0.998	6	56

Table C.2: Parameters of the peak number distributions of single days (year 1998; $\tau = 19$ dBZ). The parameters listed are those of Equation 3.1. Additionally, the correlation coefficient (r), the maximum peak number used for the calculation of the parameters (p_m) and the maximum peak number that occurred on the respective day (p_{max}) are given as well.

date	c_0	d_0	r	p_m	p_{max}
1998/06/10	0.640	-2.310	-0.991	8	47
1998/06/11	0.582	-2.314	-0.993	8	79
1998/06/15	0.615	-2.356	-0.992	7	98
1998/06/16	0.653	-2.420	-0.998	8	70
1998/06/17	0.688	-2.542	-0.998	7	24
1998/06/18	0.807	-2.628	-0.999	4	11
1998/06/28	0.609	-2.267	-0.992	8	77
1998/07/01	0.704	-2.442	-0.998	7	106
1998/07/05	0.753	-2.915	-0.997	5	28
1998/07/06	0.788	-2.976	-0.999	5	35
1998/07/07	0.730	-2.571	-0.999	6	70
1998/07/14	0.786	-2.797	-1.000	6	67
1998/07/15	0.647	-2.373	-0.998	8	62
1998/07/31	0.696	-2.567	-0.998	6	87
1998/08/05	0.669	-2.560	-0.996	7	19
1998/08/22	0.701	-2.506	-0.999	6	110
1998/08/23	0.671	-2.494	-0.995	6	72
1998/08/27	0.725	-2.492	-0.999	7	39
1998/08/29	0.715	-2.611	-0.997	7	55

Appendix D

Rain Area Distribution

Table D.1: Coefficients of Equation 3.4 (σ_p) for the area distributions for the various thresholds. Data of $2 \leq p \leq 7$ were used for the fit.

τ [dBZ]	c_1	d_1	r
7	0.76	-0.35	1.00
19	0.77	-0.36	0.99
28	0.77	-0.39	0.99
37	0.65	-0.34	0.96

Table D.2: Coefficients of Equation 3.5 (μ_p) for the area distributions for the various thresholds. Due to the limited number of data no fit for $\tau = 37$ dBZ was possible.

τ [dBZ]	c_2	c_3	d_2	d_3	r
7	6.41	0.30	0.10	-0.90	0.99
19	5.98	0.36	0.12	-1.14	0.99
28	5.69	0.35	0.13	-1.24	0.98
37	-	-	-	-	-

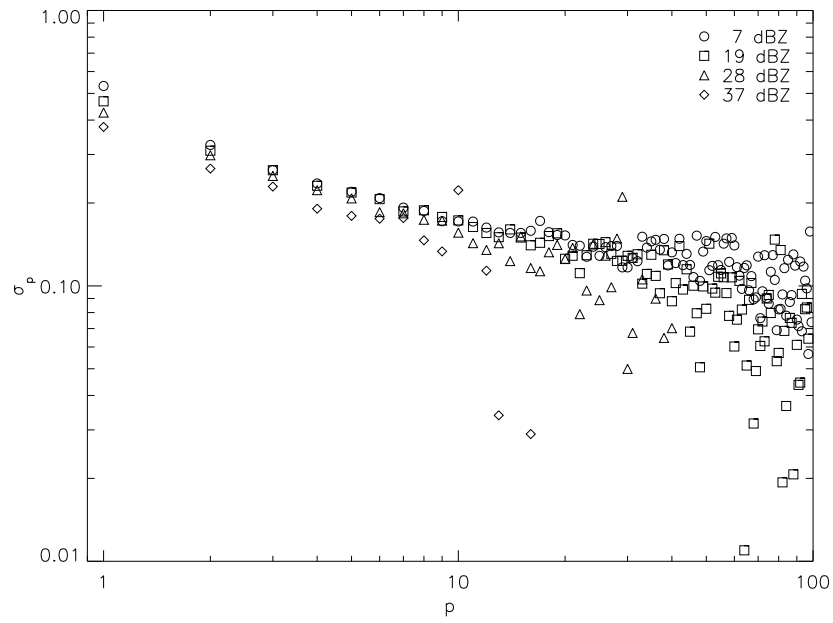


Figure D.1: Parameter σ_p as a function of peak number p for the diameter distribution

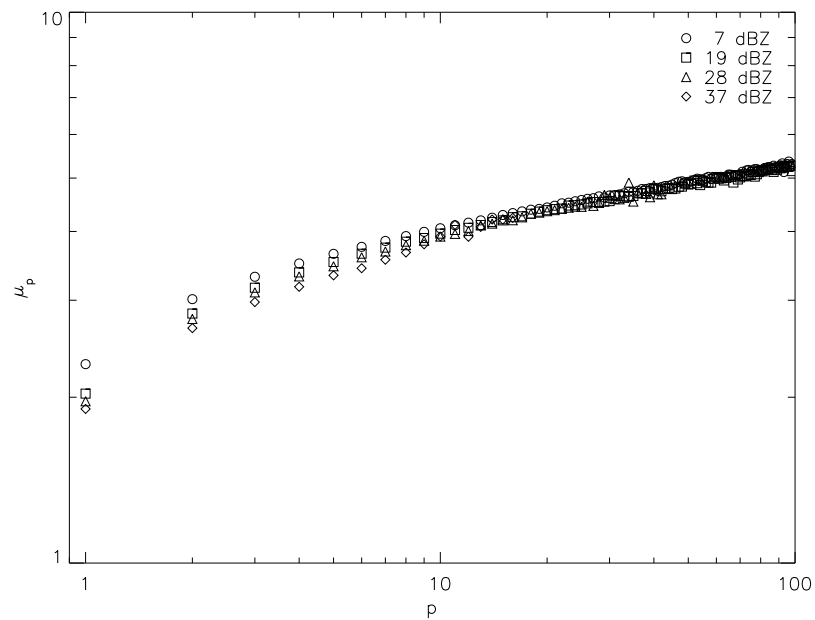


Figure D.2: Parameter μ_p as a function of peak number p for the diameter distribution.

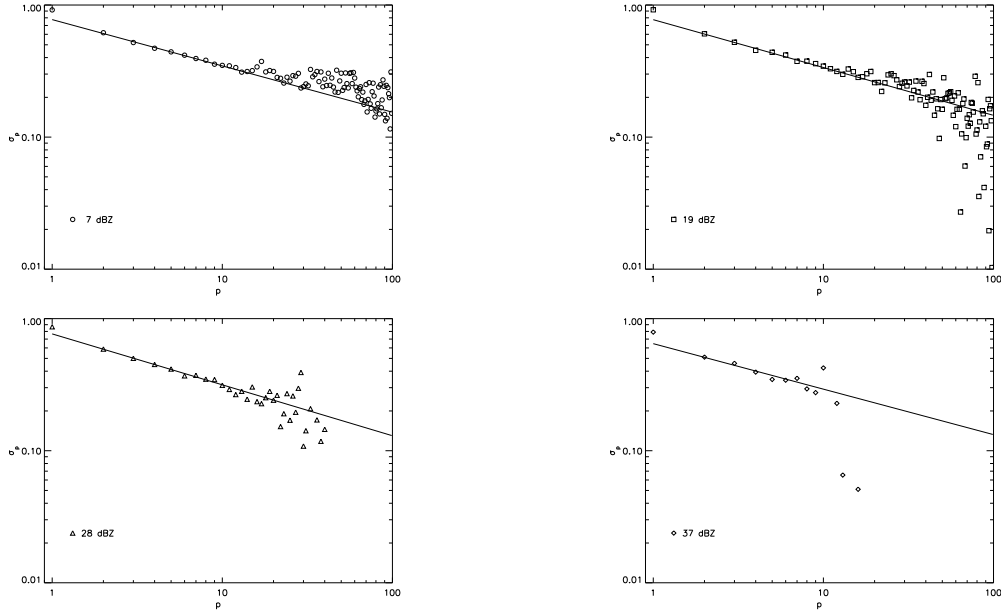


Figure D.3: Parameter σ_p as a function of p for the area distribution. The solid line represents the corresponding power law fits 3.4. The parameters of which are given in Table D.1.

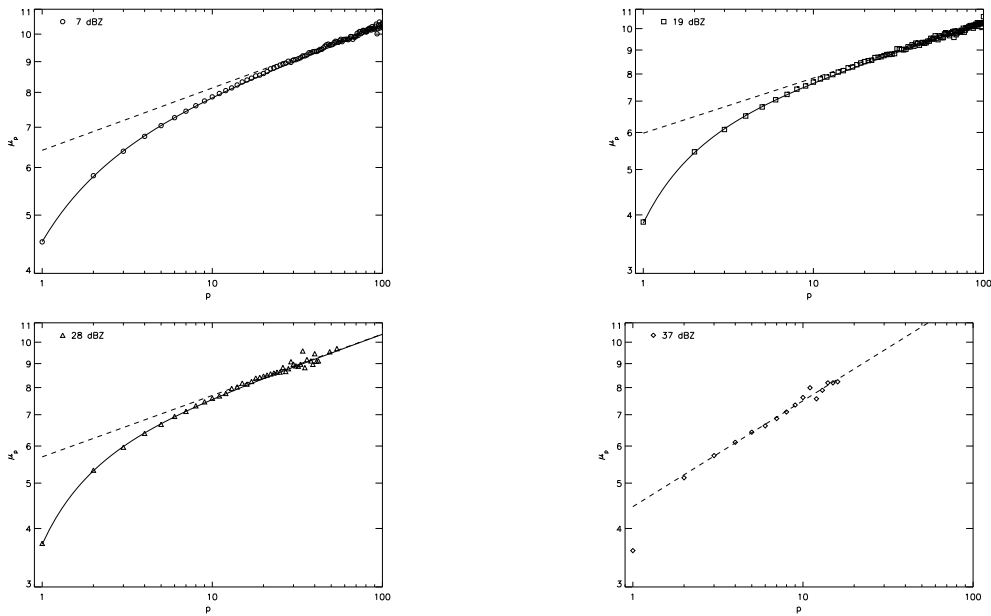


Figure D.4: Parameter μ_p as a function of p for the area distribution. The dashed line represents the power law fits for $p > 30$. The solid line shows the fitted data using Equation 3.5. The parameters of which are given in Table D.2.

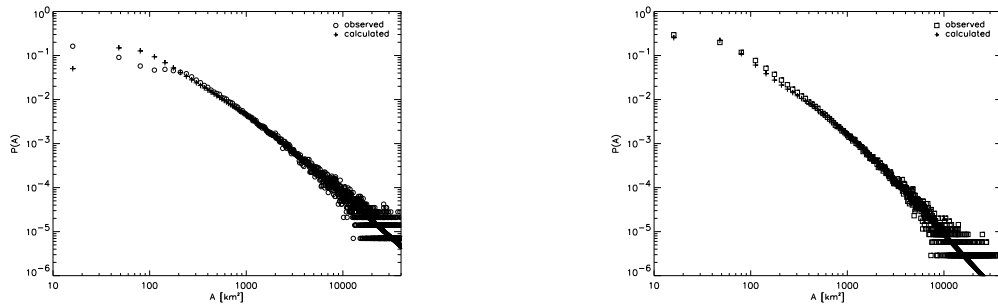


Figure D.5: Rain area size distribution for $\tau = 7$ dBZ and $\tau = 28$ dBZ. Crosses denote calculated data, while the observed data are shown by squares (bin size: 32 km^2).

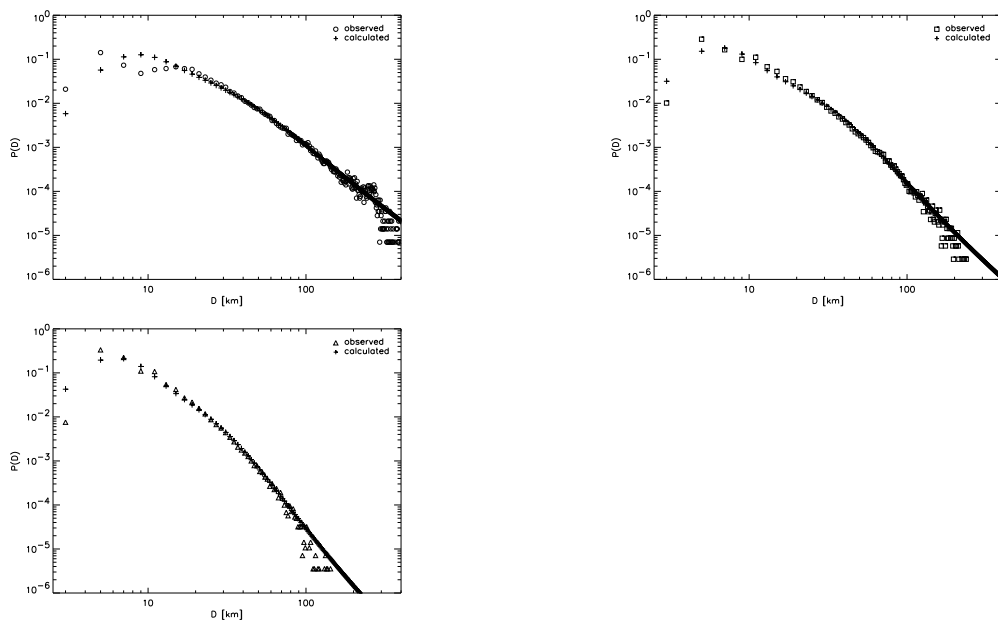


Figure D.6: Rain area diameter distribution for $\tau = 7$ dBZ (upper left), $\tau = 19$ dBZ (upper right) and $\tau = 28$ dBZ (lower left). Crosses denote calculated data, while the observed data are shown by squares (bin size: 2 km).

Bibliography

- Agee, E. M., 1982:** *An Introduction to Deep Convective Systems*, D. Reidel Publishing Company, Dordrecht, Holland. — 423 pp.
- Alestalo, M., H. Savijärvi, 1985:** Mesoscale circulations in a hydrostatic model: coastal convergence and orographic lifting. — *Tellus A*, **37** (2), 156–162.
- Ali, K., 1998:** Spatial distribution of convective clouds in north India. — *Atmos Res*, **49** (1), 1–10.
- Andersson, T., N. Gustaffson, 1994:** Coast of Departure and Coast of Arrival: Two Important Concepts for the Formation and Structure of Convective Snowbands over Seas and Lakes. — *Mon Weather Rev*, **122** (6), 1036–1050.
- Atkins, N. T., R. M. Wakimoto, T. M. Weckwerth, 1995:** Observation of the sea-breeze front during CaPE. Part II: Dual-Doppler and aircraft analysis. — *Mon Weather Rev*, **123** (4), 944–969.
- Atkinson, B. W., J. W. Zhang, 1996:** Mesoscale shallow convection in the atmosphere. — *Rev Geophys*, **34** (4), 403–431.
- Bak, P., C. Tang, K. Wiesenfeld, 1987:** Self-Organized Criticality: An Explanation of $1/f$ Noise. — *Phys Rev Lett*, **59** (4), 381–384.
- Bak, P., C. Tang, K. Wiesenfeld, 1988:** Self-organized criticality. — *Phys Rev A*, **38** (1), 364–374.
- Barthlott, C., U. Corsmeier, C. Meißner, F. Braun, C. Kottmeier, 2006:** The influence of mesoscale circulation systems on triggering convective cells over complex terrain. — *Atmos Res*, **81** (2), 150–175.
- Benner, T. C., J. A. Curry, 1998:** Characteristics of small tropical cumulus clouds and their impact on the environment. — *J Geophys Res*, **103** (D22), 28753–28767.

- Bennett, L. J., K. A. Browning, A. M. Blyth, D. J. Parker, P. A. Clark, 2006:** A review of the initiation of precipitating convection in the United Kingdom. — *Q J Roy Meteor Soc*, **132 (617)**, 1001–1020.
- van de Berg, L. C. J., J. Oerlemans, 1985:** Simulation of the sea-breeze front with a model of moist convection. — *Tellus A*, **37 (1)**, 30–40.
- Biondini, R., 1976:** Cloud motion and rainfall statistics. — *J Appl Meteorol*, **15**, 205–224.
- Burt, D. T., B. J. Schachter, 1980:** Two Algorithms for Constructing a Delaunay Triangulation. — *Int J Computer Information Sci*, **9**, 219–242.
- Burt, S., 2005:** Cloudburst upon Hendraburnick Down: the Boscastle storm of 16 August 2004. — *Weather*, **60**, 219–227.
- Cahalan, R. F., J. H. Joseph, 1989:** Fractal characteristics of cloud fields. — *Mon Weather Rev*, **117**, 261–272.
- Carvalho, L. M. V., M. A. F. Silva Dias, 1998:** An application of fractal box dimension to the recognition of mesoscale cloud patterns in infrared satellite images. — *J Appl Meteorol*, **37 (10)**, 1265–1282.
- Cheng, M. D., A. Arakawa, 1997:** Inclusion of rain water budget and convective downdrafts in the Arakawa-Schubert parametrization. — *J Atmos Sci*, **54 (10)**, 1359–1378.
- Crane, R. K., 1996:** *Electromagnetic Wave Propagation Through Rain*. — Wiley-Interscience, New York, 273 pp.
- Crook, N. A., 1996:** Sensitivity of moist convection forced by boundary-layer processes to low-level thermodynamic fields. — *Mon Weather Rev*, **124 (8)**, 1767–1785.
- Crook, N. A., T. C. Clark, M. W. Moncrieff, 1990:** The Denver cyclone. Part I: Generation in low-Froude-number flow. — *J Atmos Sci*, **47 (23)**, 2725–2742.
- Crook, N. A., T. C. Clark, M. W. Moncrieff, 1991:** The Denver cyclone. Part II: Interaction with the convective boundary layer. — *J Atmos Sci*, **48 (19)**, 2109–2126.
- Crow, E. L., K. Shimizu, 1988:** *Log-normal Distributions: Theory and Application*. — M. Dekker, New York, 387 pp.
- Davolio, S., A. Buzzi, P. Malguzzi, 2006:** Orographic influence on deep convection: case study and sensitivity experiments. — *Meteorol Z*, **15 (2)**, 215–223.

- Dennis, A. S., F. G. Fernald, 1963:** Frequency distribution of shower sizes. — *J Appl Meteorol*, **2**, 767–769.
- Drufuca, G., 1977:** Radar-derived statistics on the structure of precipitation patterns. — *J Appl Meteorol*, **16 (10)**, 1029–1035.
- DWD, 1998:** *Der Radarverbund - Informationen zum Wetterradar-Verbundsystem*. — Deutscher Wetterdienst, Offenbach.
- Emanuel, K. A., 1994:** *Atmospheric Convection*. — Oxford University Press, Inc., New York, 580 pp.
- Feral, L., H. Sauvageot, 2002:** Fractal identification of supercell storms. — *Geophys Res Lett*, **29 (14)**, Art. No. 1686.
- Fovell, R. G., P. S. Dailey, 2001:** Numerical simulation of the interaction between the sea-breeze front and horizontal convective rolls. Part II: Alongshore ambient flow. — *Mon Weather Rev*, **129 (8)**, 2057–2072.
- Garreaud, R. D., J. M. Wallace, 1997:** The diurnal march of convective cloudiness over the Americas. — *Mon Weather Rev*, **125 (12)**, 3157–3171.
- Georgakakos, K. P., W. F. Krajewski, 1996:** Statistical microphysical causes of rainfall variability in the tropics. — *J Geophys Res*, **191 (D21)**, 26165–26180.
- Getling, A. V., 1998:** *Rayleigh-Bénard Convection*. — World Scientific, Singapore, 245 pp.
- Goldhirsh, J., B. Musiani, 1986:** Rain cell size statistics derived from radar observations at Wallops Island, Virginia. — *IEEE T Geosci Remote*, **24 (6)**, 947–954.
- Gotoh, K., Y. Fujii, 1998:** A fractal dimension analysis on the cloud shape parameters of cumulus over land. — *J Appl Meteorol*, **37**, 1283–1292.
- Grabowski, W. W., P. Bechtold, et al., 2006:** Daytime convective development over land: A model intercomparison based on LBA observations. — *Q J Roy Meteor Soc*, **132 (615)**, 317–344.
- Gray, W. R., A. W. Seed, 2000:** The characterisation of orographic rainfall. — *Meteorol Appl*, **7 (2)**, 105–119.
- Hauf, T., C. Dettmer, W. Deierling, 2001:** Parametrisierung der Statistik von konvektiven Niederschlagsfeldern durch inverse Modellierung. — *BMBF-Projekt 01LA9853/0, Abschlußbericht*.
- Houze, R. A., 1993:** *Cloud Dynamics*. — Academic Press, San Diego, 573 pp.

- Houze, R. A., C. P. Cheng, 1977:** Radar characteristics of tropical convection observed during GATE - Mean properties and trends over summer season. — *Mon Weather Rev*, **105** (8), 964–980.
- Hsu, H. H., M. Y. Lee, 2005:** Topographic effects on the eastward propagation and initiation of the Madden-Julian oscillation. — *J Climate*, **18** (6), 795–809.
- Jakob, D., et. al., 2006:** BALTIMOS. — *Theor Appl Climatol*, **in review**.
- Joseph, J. H., R. F. Cahalan, 1990:** Nearest neighbor spacing of fair weather cumulus clouds. — *J Appl Meteorol*, **29**, 793–805.
- Kedem, B., L. S. Chiu, Z. Karni, 1990:** An analysis of the threshold method for measuring area-averaged rainfall. — *J Appl Meteorol*, **29** (1), 3–20.
- Kingsmill, D. E., 1995:** Convection initiation associated with a sea-breeze front, a gust front, and their collision. — *Mon Weather Rev*, **123** (10), 2913–2933.
- Koistinen, J., D. B. Michelson, 2002:** BALTEX weather radar-based precipitation products and their accuracies. — *Boreal Environmental Research*, **7** (3), 253–263.
- Konrad, T. G., 1978:** Statistical models of summer rainshowers derived from fine-scale radar observations. — *J Appl Meteorol*, **17** (2), 171–188.
- Kundzewicz, Z. W., U. Ulbrich, et al., 2005:** Summer Floods in Central Europe - Climate Change Track? — *Nat Hazards*, **36** (1-2), 165–189.
- Kuo, K. S., R. M. Welch, R. C. Weger, M. A. Engelstad, S. K. Sengupta, 1993:** The three-dimensional structure of cumulus clouds over the ocean: 1. Structural analysis. — *J Geophys Res*, **98** (D11), 20685–20711.
- Lawford, R. G., 1996:** Temporal variations in the scaling properties of rain echoes during the development of a cold loe in Saskatchewan. — *J Appl Meteorol*, **35** (6), 796–809.
- Lopez, R. E., 1977:** The Lognormal Distribution and Cumulus Cloud Populations. — *Mon Weather Rev*, **105**, 865–872.
- Lopez, R. E., D. O. Blanchard, D. Rosenfeld, W. L. Hiscox, M. J. Casey, 1984:** Population characteristics, development processes and structure of radar echoes in south Florida. — *Mon Weather Rev*, **112** (1), 56–71.
- Lovejoy, S., 1982:** Area-perimeter relation for rain and cloud areas. — *Science*, **216** (4542), 185–187.

- Machado, L. A. T., M. Desbois, J. P. Duvel, 1992:** Structural characteristics of deep convective systems over tropical Africa and the Atlantic Ocean. — *Mon Weather Rev*, **120** (3), 392–406.
- Machado, L. A. T., W. B. Rossow, 1993:** Structural characteristics and radiative properties of tropical cloud clusters. — *Mon Weather Rev*, **121** (12), 3234–3260.
- Mandelbrodt, B., 1982:** *The Fractal Geometry of Nature*. — W.H. Freeman, New York, 461 pp.
- Mapes, B. E., R. A. Houze, 1993:** Cloud clusters and super clusters over the oceanic warm pool. — *Mon Weather Rev*, **121** (5), 1398–1415.
- Mather, J. R., 1949:** An investigation of the dimensions of precipitation echoes by radar. — *B Am Meteorol Soc*, **30**, 271–277.
- Mesnard, F., H. Sauvageot, 2003:** Structural characteristics of rain fields. — *J Geophys Res*, **108** (D13), 4385–4401.
- Miller, J. R., A. S. Dennis, J. H. Hirsch, D. E. Cain, 1975:** Statistics of shower echoes in western North Dakota. — In: *Preprints 16th Radar Meteorology Conference, Houston*, Am. Meteorol. Soc, Boston, pp. 391–396.
- Ohsawa, T., H. Ueda, T. Hayashi, A. Watanabe, J. Matsumoto, 2001:** Diurnal variations of convective activity and rainfall in tropical Asia. — *J Meteorol Soc Jpn*, **79** (1B), 333–352.
- Pike, W. S., 2003:** Hailfalls at Woodlands St. Mary, West Berkshire, 13 May 2003. — *Weather*, **58** (12), 451–452.
- Potts, R. J., T. D. Keenan, P. T. May, 2000:** Radar characteristics of storms in the Sydney area. — *Mon Weather Rev*, **128** (9), 3308–3319.
- Raymond, W. H., 1997:** A theoretical evaluation of the relevance of lognormal distributions for the moisture flux and wind components. — *Mon Weather Rev*, **125** (11), 3018–3023.
- Raymond, W. H., 2000:** Moisture advection using relative humidity. — *J Appl Meteorol*, **39** (12), 2397–2408.
- Roeloffzen, J. C., W. D. V. den Berg, J. Oerlemans, 1986:** Frictional convergence at coastlines. — *Tellus A*, **38** (5), 397–411.
- Rys, F. S., A. Waldvogel, 1986:** Fractal shape of hail clouds. — *Phys Rev Lett*, **56** (7), 784–787.
- Sauvageot, H., 1994:** The probability density function of rain rate and the estimation of rainfall by area integrals. — *J Appl Meteorol*, **33** (11), 1255–1262.

- Sauvageot, H., F. Mesnard, R. S. Tenorio, 1999:** The relation between area-averaged rain rate and the rain cell distribution parameters. — *J Atmos Sci*, **56** (1), 57–70.
- Schröter, M., 2003:** *Untersuchung der Evolution von Konvektionsstrukturen bei Kaltluftausbrüchen mit Hilfe eines parallelisierten Grobstrukturmodells.* — PhD Thesis, Institut für Meteorologie und Klimatologie, Universität Hannover, 125 pp.
- Sengupta, S. K., R. M. Welch, M. S. Navar, T. A. Berendes, D. W. Chen, 1990:** Cumulus cloud field morphology and spatial patterns derived from high spatial resolution Landsat imagery. — *J Appl Meteorol*, **29**, 1245–1267.
- Smith, P. L., 1990:** *Precipitation Measurement and Hydrology: Panel Report*, American Meteorological Society, Boston. — 806 pp.
- Smolarkiewicz, P. K., R. M. Rasmussen, T. C. Clark, 1988:** On the dynamics of Hawaiian cloud bands: island forcing. — *J Atmos Sci*, **45** (13), 1872–1905.
- Stirling, A. J., J. C. Petch, 2004:** The impacts of spatial variability on the development of convection. — *Q J Roy Meteor Soc*, **130** (604), 3189–3206.
- Theusner, M., T. Hauf, 2004:** A study on the small scale precipitation structure over Germany using the radar network of the German Weather Service. — *Meteorol Z*, **13**, 311–322.
- Theusner, M., T. Hauf, 2006:** Validation of BALTIMOS precipitation structures using BALTRAD radar data. — *Theor Appl Climatol*, **in review**.
- Tian, W. S., D. J. Parker, 2002:** Two-dimensional simulation of orographic effects on mesoscale boundary-layer convection. — *Q J Roy Meteor Soc*, **128** (584), 1929–1952.
- Tian, W. S., D. J. Parker, C. A. D. Kilburn, 2003:** Observations and numerical simulation of atmospheric cellular convection over mesoscale topography. — *Mon Weather Rev*, **131** (1), 225–235.
- Wakimoto, R. M., N. T. Atkins, 1994:** Observation of the sea-breeze front during CaPE. Part I: Single-Doppler, satellite, and cloud photogrammetry analysis. — *Mon Weather Rev*, **122** (6), 1092–1114.
- Walther, A., R. Bennartz, 2006:** Radar-based precipitation type analysis in the Baltic area. — *Tellus A*, **58** (3), 331–343.
- Weckwerth, T. M., 2000:** The effect of small-scale moisture variability on thunderstorm initiation. — *Mon Weather Rev*, **128** (12), 4017–4030.

- Weckwerth, T. M., J. W. Wilson, R. M. Wakimoto, 1996:** Thermodynamic variability within the convective boundary layer due to horizontal convective rolls. — *Mon Weather Rev*, **124** (5), 769–784.
- Weger, R. C., J. Lee, T. Zhu, R. M. Welch, 1992:** Clustering, randomness and regularity in cloud fields: 1. Theoretical considerations. — *J Geophys Res*, **97** (D18), 20519–20536.
- Welch, R. M., K. S. Kuo, B. A. Wielicki, S. K. Sengupta, L. Parker, 1988:** Marine stratocumulus cloud fields off the coast of southern California observed using Landsat imagery: 1. Structural characteristics. — *J Appl Meteorol*, **27**, 341–362.
- Welch, R. M., B. A. Wielicki, 1986:** The stratocumulus nature of fog. — *J Clim Appl Meteorol*, **25**, 101–111.
- Wielicki, B. A., R. M. Welch, 1986:** Cumulus cloud properties derived using Landsat satellite imagery. — *J Clim Appl Meteorol*, **25**, 261–276.
- Wilson, J. W., G. B. Foote, N. A. Crook, J. C. Frankhauser, C. G. Wade, J. D. Tuttle, C. K. Mueller, 1992:** The role of boundary-layer convergence zones and horizontal rolls in the initiation of thunderstorms: a case study. — *Mon Weather Rev*, **120** (9), 1785–1815.
- Wilson, J. W., D. L. Megenhardt, 1997:** Thunderstorm initiation, organization, and lifetime associated with Florida boundary layer convergence lines. — *Mon Weather Rev*, **125** (7), 1507–1525.
- Zhu, T., J. Lee, R. C. Weger, R. M. Welch, 1992:** Clustering, randomness and regularity in cloud fields: 2. Cumulus cloud fields. — *J Geophys Res*, **97** (D18), 20537–20558.

Acronyms and Symbols

Symbol	Explanation
a_0, a_n	Function coefficients
A_i, A	Area of a single rain area
A_{max}	Area of reflectivity per peak
\bar{A}_p	Mean area of rain areas with a certain peak number
A_{px}	Area of a pixel of the radar image
A_r	Average area of the rain areas at a certain time or for a certain period of time
A_{total}	Total area of the rain areas at a certain time or for a certain period of time
AVHRR	Advanced Very High Resolution Radiometer
BALTIMOS	Baltex Integral Model System
$c_{0,1,2,3}$	Power law coefficients
$c_{4,5}$	Function coefficients
Cb	Cumulonimbus cloud
Cbs	Plural form of Cb
d	Fractal dimension
D, D_i	Equivalent circular diameter of a (single) rain area
$d_{0,1,2,3}$	Power law exponents
d_4	Function coefficient
D_b	Break diameter of the rain areas
dB	Decibels, difference between values of dBZ
dBZ	Decibels of Z , Unit of radar reflectivity Z
DFG	Deutsche Forschungsgemeinschaft (German Research Foundation)
\bar{D}_p	Mean equivalent circular diameter of rain areas with a certain peak number
DWD	Deutscher Wetterdienst (German Weather Service)
\mathbb{E}	Set of nearest neighbor distances of all rain areas with $p = p_0$
\mathbb{E}_i	Set of nearest neighbor distances of one rain area with region index i (undefined for $p = 1$)
e_{ij}	Distance between a peak and its nearest neighboring peak
FFT	Fast Fourier Transform

Symbol	Explanation
GIF	Graphics Interchange Format
GUI	Graphical user interface
i	Region index of a rain area
IMuK	Institute of Meteorology and Climatology, Leibniz University of Hannover, Germany
λ	Scale break value
μ_p	Mean of the log-normal RASD for a certain peak number
N_A	Number of rain areas at a certain time or during a period of time
$N_{A,p}$	Number of rain areas at a certain time or during a period of time
n_i	Number of pixels of a rain area
NND	Nearest neighbor distribution
NOAA	National Oceanic and Atmospheric Administration
n_p	Total number of peaks at a certain time or during a certain period of time
n_r	Average number of reflectivity peaks per rain area at a certain time or during a certain period of time
p, p_i	Peak number of a (single) rain area
$P(A)$	Rain Area Size Distribution of A
PC-product	National radar composite image of the DWD
$P(D)$	Rain Area Size Distribution of D
ϕ_n	Off-set parameter
p_m	Maximum peak number used for fitting
p_{max}	Maximum peak number
PND	Peak number distribution
$P(p)$	Peak number distribution
$P_p(D)$	Rain area size distribution for D and A
$P(p, x)$	Frequency of a rain area with p peaks and area A or diameter D within the whole population
r	correlation coefficient
R	Rain rate
RA	Rain area
RASD	Rain area size distribution
S1	Set of radar images with 2 km spatial resolution and 0.5 dB reflectivity steps
S2	Set of radar images with 2 km spatial resolution and 6-step reflectivity scale
s_i	Length of the perimeter of a rain area in pixels
SOC	Self organizing criticality
σ_p	Standard deviation of the log-normal RASD for a certain peak number
σ_x, σ_y	Standard deviation of the filter function used to smooth the radar images

Symbol	Explanation
τ	Threshold value of rain rate/radar reflectivity
U, U_i	Perimeter of a (single) rain area
UTC	Coordinated Universal Time
x	Substitute for A and D
x_{ij}	Peak x-coordinates
\mathbb{X}_{ij}	Set of x-coordinates of a peak
y_{ij}	Peak y-coordinates
\mathbb{Y}_{ij}	Set of y-coordinates of a peak
Z	Radar reflectivity value

Acknowledgements

Ich danke besonders Herrn Prof. Dr. T. Hauf, der als Doktorvater diese Arbeit initiiert und die Betreuung und Begutachtung dieser Arbeit übernommen hat. Immer hat er mir mit seinem Rat und wichtigen Denkanstößen zur Seite gestanden und war jederzeit für eine wissenschaftliche Diskussion der Ergebnisse da. Außerdem möchte ich mich bei Herrn Prof. Dr. D. Etling für die Übernahme des Korreferats bedanken.

Danken möchte ich auch dem Deutschen Wetterdienst, der die Radardaten schon für ein früheres Projekt zur Verfügung gestellt hatte (HAUF *et al.* 2001; BMBF01LA9853/0) sowie Herrn M. Hagen vom Institut für Physik der Atmosphäre der DLR in Oberpfaffenhofen für die Aufbereitung der Daten. Zudem hat mir der DWD einen Testdatensatz RZ-Daten überlassen, wofür ich mich ebenfalls bedanken möchte.

Weiterhin gilt mein Dank Herrn Prof. Dr. U. Finke, der mir jederzeit bei Fragen zur IDL-Programmierung weitergeholfen hat. Ebenfalls danke ich meinen (ehemaligen) Kollegen und Freunden Peer Röhner, Clemens Drüe, Tanja Weusthoff, Matthias Brakebusch, Theres Franke, Susanne Keyn, Katharina Koppe, Sonja Rosczyk, Sonja Fabig, Rudi Deckert und Tahera Ali, die mir immer bereitwillig bei Fragen zu \LaTeX und IDL geholfen, für die Korrektur meiner Dissertation gesorgt und auch sonst für ein sehr angenehmes Arbeitsklima gesorgt haben.

Außerdem danke ich noch noch besonders meinen Eltern und meiner Schwester Kristina, die mich während meines ganzen Studiums unterstützt und somit dies alles mit ermöglicht haben.

Curriculum Vitae

Persönliche Daten

Name Michael Theusner
Geburtsdatum, -ort 08. Dezember 1974, Hannover

Bildungsweg

1981 - 1985 Grundschole Gehrden
1985 - 1987 Orientierungsstufe Gehrden
1987 - 1994 Matthias-Claudius-Gymnasium Gehrden
Juni 1994 Abitur
1994 - 1995 Zivildienst
1995 - 2001 Studium der Meteorologie an der Universität Hannover
Sept. 1997 Vordiplom
Febr. 1999 - Jan. 2000 Auslandsstudium, University of Tasmania, Hobart, Australien
Nov. 1999 Graduate Diploma of Science with First Class Honours, Titel: "Physical Causes of Differences in Antarctic Climate Trends"
Mai 2000 - Mai 2001 Diplomarbeit, Titel: "An Investigation of Changes of Climate Zones on Global and Regional Scales"
14. Mai 2001 Letzte Diplomprüfung, Abschluss: Diplom-Meteorologe
Mai 2001 - Jan. 2005 Wissenschaftlicher Mitarbeiter am Institut für Meteorologie und Klimatologie der Universität Hannover, Bearbeitung des DFG-Projekts BALTIMOS "Kleinskalige Niederschlagsstruktur - Beobachtung und Validierung" mit dem Ziel der Promotion zum Dr. rer. nat.
Seit Febr. 2005 Wissenschaftlicher Mitarbeiter am Institut für Meteorologie und Klimatologie der Universität Hannover, Bearbeitung des EU-Projektes FLYSAFE